INVESTIGATION OF AERODYNAMIC CHARACTERISTICS OF DELTA WINGS

A THESIS SUBMITTED BY

ANIMESH ROY

DOCTOR OF PHILOSOPHY (ENGINEERING)

DEPARTMENT OF POWER ENGINERING

FACULTY COUNCIL OF ENGINEERING AND TECHNOLOGY

JADAVPUR UNIVERSITY

KOLKATA 700032, INDIA

2024

INVESTIGATION OF AERODYNAMIC CHARACTERISTICS OF DELTA WINGS

A THESIS SUBMITTED

IN FULFILLMENT OF THE REQUIREMENT FOR THE DEGREE OF

DOCTOR OF PHILOSOPHY (ENGINEERING)

UNDER THE GUIDANCE AND SUPERVISION OF

PROF. BIRESWAR MAJUMDAR
EX-PROFESSOR, DEPARTMENT OF POWER ENGINEERING,
JADAVPUR UNIVERSITY
&
PROF. PRABIR KUMAR DE
PROFESSOR, DEPARTMENT OF MECHANICAL ENGINEERING,
JADAVPUR UNIVERSITY

SUBMITTED BY

ANIMESH ROY

FACULTY COUNCIL OF ENGINEERING AND TECHNOLOGY

JADAVPUR UNIVERSITY

KOLKATA 700032, INDIA

2024

JADAVPUR UNIVERSITY

FACULTY COUNCIL OF ENGINEERING AND TECHNOLOGY

INDEX NO. 201/17/E

1. Title of the thesis:	**Investigation of Aerodynamic Characteristics of Delta Wings**
2. Name, Designation and Institution of the Supervisor/s:	**1. Dr. Bireswar Majumdar** Professor (Retd.) Department of Power Engineering Jadavpur University Salt Lake Campus Kolkata –700106, India **2. Dr. Prabir Kumar De** Professor Department of Mechanical Engineering Jadavpur University Kolkata –700032, India
3. List of Publications:	**Journal Publications:** 1. Animesh Roy, Samrat Biswas, Prabir Kumar De and Bireswar Majumdar, "*Analysis of Vortex Dominated Flow over Double Delta Wing*", Journal of Mines, Minerals and Fuels, Vol. 71, No. 10, December 2023. 2. Samrat Biswas, Animesh Roy, Prabir Kumar De and Bireswar Majumdar, "*Surface Flow Visualization Tests on Swept Back Wing Configuration Subjected to Subsonic Flow*", SAMRIDDHI: A Journal of Physical

	Sciences, Engineering and Technology, vol. 12, issue. 2, December 2020. 3. Samrat Biswas, Aritras Roy, Animesh Roy, Prabir Kumar De and Bireswar Majumdar, "*Flow Field Investigation on a Double Delta Wing*", Journal of Aerospace Sciences and Technologies, vol. 71, no. 2, May 2019. 4. Samrat Biswas, Animesh Roy, Prabir Kumar De and Bireswar Majumdar, "*Investigation of Flow Field over Swept Back Wing*", International Journal of Research and Analytical Reviews, vol. 6, no. 1, March 2019. 5. Samrat Biswas, Animesh Roy, Prabir Kumar De and Bireswar Majumdar, "*Experimental and Numerical Investigation of Flow Field Structure over Swept Back Wing*", Journal of Emerging Technologies and Innovative Research, vol. 6, no. 3, March 2019.

STATEMENT OF ORIGINALITY

I Animesh Roy, registered on 23.08.2017 do hereby declare that this thesis entitled "**Investigation of Aerodynamic Characteristics of Delta Wings**" contains literature survey and original research work done by the undersigned candidate as part of Doctoral studies.

All information in this thesis have been obtained and presented in accordance with existing academic rules and ethical conduct. I declare that, as required by these rules and conduct, I have fully cited and referred all materials and results that are not original to this work.

I also declare that I have checked this thesis as per the “Policy on Anti Plagiarism, Jadavpur University, 2019”, and the level of similarity as checked by iThenticate software is _____%.

Signature of Candidate:

Date:

Certified by Supervisor(s):

(Signature with date, seal)

1.

2.

CERTIFICATE FROM THE SUPERVISOR/S

This is to certify that the thesis entitled " **Investigation of Aerodynamic Characteristics of Delta Wings**"submitted by Shri Animesh Roy, who got his/her name registered on 23.08.2017 for the award of Ph.D. (Engg) degree of Jadavpur University is absolutely based upon his own work under the supervision of Prof. Bireswar Majumdar, Ex-Professor, Department of Power Engineering and Prof. Prabir Kumar De, Professor, Department of Mechanical Engineering, Jadavpur university, Kolkata, India and that neither his thesis nor any part of the thesis has been submitted for any degree/diploma or any other academic award anywhere before.

1._____

Signature of the Supervisor and date with Office Seal

2._____

Signature of the Supervisor and date with Office Seal

ACKNOWLEDGEMENTS

The list is endless if I have to thank all the people who made this work possible. My first and sincere thanks go to Prof. Bireswar Majumdar for giving me the opportunity to work on such an exciting project, and then providing his invaluable guidance. He gave me the thought that there are no limits on what we can achieve. Thank you, sir, from the bottom of my heart. My gratitude to Prof. Prabir Kumar De for his support sincere support from the very beginning. He never said no to anybody when someone pursue a new idea. I am grateful to have such fantastic duo of supervisors.

The other person who I owe an immense gratitude is my laboratory fellow, researcher and friend Dr. Samrat Biswas. We agreed in many things, disagreed in others, but there was no time where I could not learn something from him. He was with me helping with all equipment and others that he best knows during my work. I wish I could have had him for longer time during research. Thanks for your time and friendship.

I want to take this opportunity to convey my sincere gratitude to my colleagues, the members of Power Engineering department especially Sri Nepal Ranjan Dey, and representatives of library for serving all demands positively. I express my gratefulness to the faculty members of Power Engineering for providing their continuous endorsement to make this learning procedure a great experience.

Friends outside the institute helped me to forget my research difficulties and enjoy my life. All of them participated in this thesis, by relaxing me in the anger times.

I convey my gratefulness to Jadavpur University for giving the opportunity to use their labs and equipment.

I don’t want to forget my father, my wife Kakali and son Pablo. All of you helped me to be here. Although they may not have understood most of the research I was performing, why always I was annoyed, or why the rooms turned to a mess of papers, they were accepting and supportive. Their encouragement and unconditional love made this possible. Thanks for your support.

I am grateful to every person who continuously pushed me, encouraged me to complete the work. Many people – whether they know it or not – enabled me to complete my work.

Thank you all.

ANIMESH ROY

ABSTRACT

This thesis presents a comprehensive experimental investigation of the aerodynamic characteristics of various delta wings, with a primary focus on the flow field around a double delta wing under subsonic flow conditions. The study aims to enhance the understanding of the complex aerodynamic phenomena associated with double delta wings, particularly in the subsonic regime, by utilizing both experimental and numerical approaches.

The double delta wing configuration, known for its two distinct leading-edge sweeps, offers unique aerodynamic advantages, including enhanced lift, delayed stall, and improved maneuverability. These characteristics make it an ideal design for high-speed and high-performance aircraft. The research explores these benefits by employing various experimental techniques, including wind tunnel testing, oil flow visualization, balance measurement, surface pressure distribution measurements, and velocity profile assessments using a three-hole pressure probe.

The experimental investigations were conducted in a subsonic open circuit wind tunnel at the Fluid Mechanics and Machinery Laboratory, Department of Power Engineering, Jadavpur University, Kolkata, India. The double delta wing model, designed and fabricated in-house, was tested under various angles of attack to capture a comprehensive dataset. The wind tunnel tests were complemented by high-fidelity numerical simulations using Computational Fluid Dynamics (CFD) to validate and extend the experimental findings. The flow visualization techniques revealed detailed insights into the vortex formation and interaction patterns over the double delta wing. The oil flow visualization technique provided qualitative data on the surface flow streamlines and vortex structure, while the surface pressure measurements quantified the pressure distribution across the wing surface, which is critical for understanding lift and drag characteristics. The velocity profile measurements using the three-hole pressure probe further detailed the flow field over the wing, highlighting the complex interaction of vortices and the resulting aerodynamic forces. The study identified several key aerodynamic phenomena, including the formation of strong leading-edge vortices that enhance lift and delay stall, particularly at high angles of attack. The pressure distribution data showed significant variations corresponding to different flow

regimes, contributing to a deeper understanding of the aerodynamic efficiency of the double delta wing. The velocity measurements corroborated the experimental observations, providing a detailed map of the flow field and supporting the numerical simulation results.

In addition to the experimental work, extensive numerical simulations were performed to model the airflow around the double delta wing. These simulations used advanced turbulence models and grid configurations to ensure an accurate representation of the flow physics. The numerical results closely matched the experimental data, validating the computational approach and providing further insights into the unsteady flow characteristics and vortex dynamics. The findings of this thesis contribute significantly to the field of aerodynamics, particularly in understanding the flow behavior around complex wing configurations like the double delta wing. The combined experimental and numerical approach provides a robust framework for analyzing and optimizing such wing designs, with implications for improving the performance of high-speed and high-maneuverability aircraft. Future work recommended includes extending the experimental investigations to different flow regimes, such as transonic and supersonic, and exploring the impact of different wing geometries and configurations. Additionally, further refinement of the numerical models to capture more detailed unsteady flow phenomena would enhance the predictive capabilities for advanced aerodynamic designs.

In conclusion, this thesis provides a thorough investigation of the aerodynamics of double delta wings, offering valuable insights into their performance characteristics and contributing to the broader knowledge base in aerospace engineering. The integration of experimental and numerical methods presents a comprehensive approach to studying and optimizing advanced wing configurations for modern aircraft applications.

Keywords: **Aerodynamics, Double Delta Wing, Delta Wing, Oil Flow Visualization, Vortex Lift**

GRAPHICAL ABSTRACT

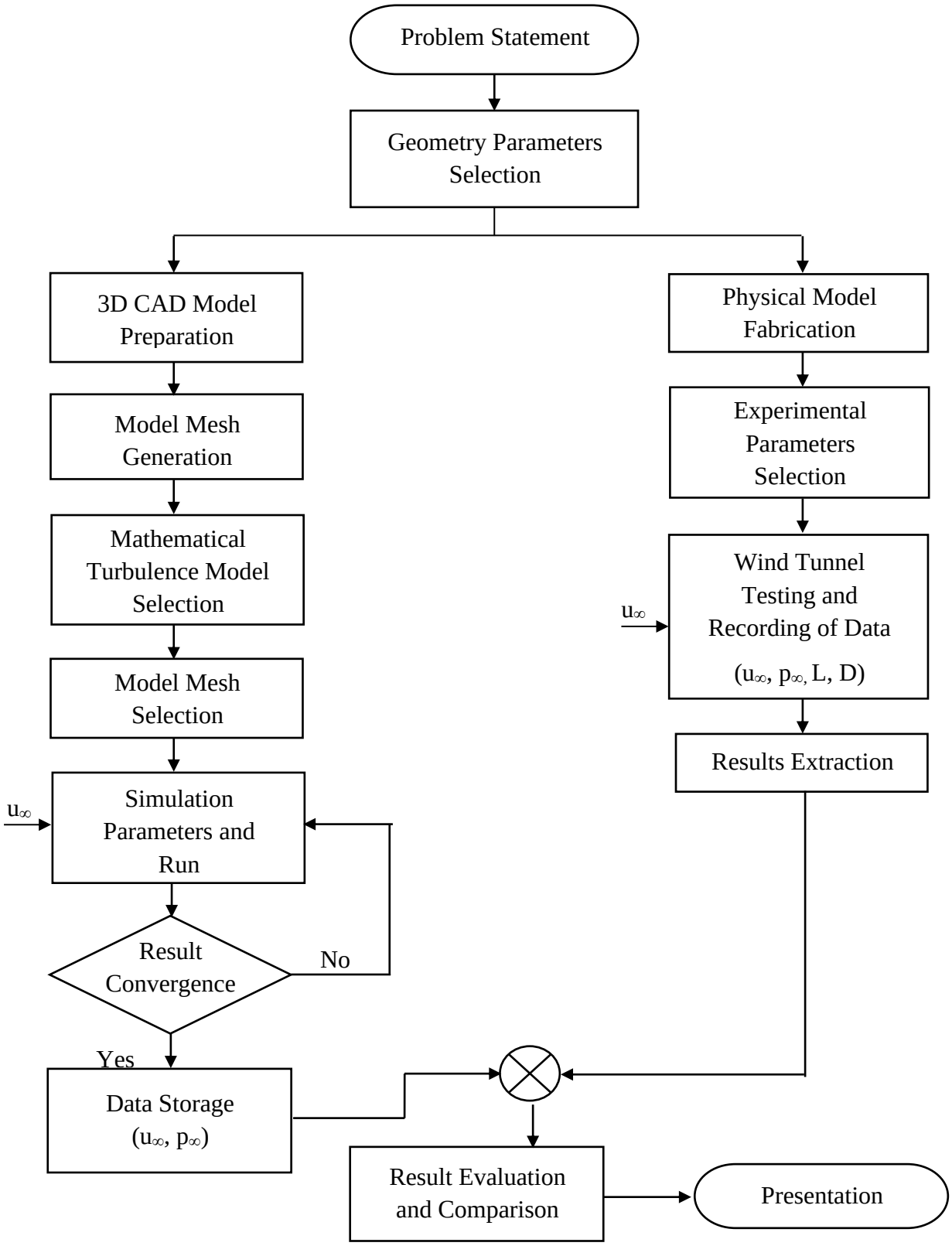

CONTENTS

NOMENCLATURE

C_L	Coefficient of lift
C_M	Coefficient of pitching moment
C_N	Coefficient of normal force
C_p	Coefficient of pressure
C_R	Wing root chord (m)
CFD	Computational Fluid Dynamics
Exp	Experimental value
$F_{\upsilon 1}$	Viscous damping factor
G_υ	Turbulent viscosity production term
Ma	Mach Number
MAC	Mean Aerodynamic Chord
NASA	National Aeronautics and Space Administration
Num	Numerical value
P_T	Total pressure
P_S	Static pressure
P_∞	Ambient pressure
Re_{MAC}	Reynolds number corresponds to MAC
S	Wing planform area (m^2)
SA	Spalart-Allmaras
T	Ambient temperature (K)
U_r	Uncertainties in the measured parameter r
U_x	Chord-wise velocity component (m/s)
U_y	Span-wise velocity component (m/s)
u_∞	Free stream velocity (m/s)
$\bar{u}$	Mean velocity
x	Chord-wise distance (m)
y	Span-wise distance (m)
y^+	Distance from wall to first grid cell in CFD
Y_u	Turbulent viscosity destruction term

z	Distance over the wing (m)
α	Pitch angle (^{o})
β	Yaw angle
ρ	Density of air
μ	Dynamic Viscosity
μ_t	Turbulent Viscosity
υ	Molecular kinematic viscosity

LIST OF TABLES

LIST OF PLATES

LIST OF FIGURES

CHAPTER 1

Introduction

In the late 1800s, research on airfoil sections began. Prior to this, scientists knew that a flat plate at a specific angle generates lift. Some early researchers investigated the relationship between lift and the shape of bird wings. In 1884, H. F. Philips developed and patented airfoil shapes in one of the earliest wind tunnels [1]. Similarly, Otto Lilienthal [2] interested in bird flight, measured bird wing shape and tested various airfoil configurations using a whirling machine. During this time, scientists recognized that wing curvature or camber was crucial for flight.

In the early 20th century, as interest in powered flight grew, more extensive research into airfoil design was conducted. This was a groundbreaking period for the field of aeronautics. To provide historical context, the Wright brothers pioneered the invention of the airplane with their first successful powered flight in December 1903 [3]. Prandtl then introduced his boundary layer theory in 1904 [4], followed by the publication of his lifting-line theory in 1918 [5]. Additionally, Munk's dissertation [6], which presented the concept of minimum-induced drag, was published in the same year. These advancements, coupled with the rapid technological progress during World War I and World War II, shaped the evolution of aviation. Experiments by engineers like Gustave Eiffel along with Ludwig Prandtl expanded knowledge of airfoil behaviour, leading to the development of the NACA airfoil series that became widely used in aircraft and other power-producing designs. [7] [8] [9]

The double-delta wing configuration evolved from these foundational developments in aerodynamics and wing design. By carefully tailoring the sweep angles and planform of the wing, aircraft designers were able to create a highly efficient wing shape suitable for a range of flight regimes, from subsonic to supersonic speeds [7] [10].

While the precise origin of the double-delta wing concept is difficult to pinpoint, its development is closely tied to advancements in supersonic flight during the Cold War era. Early research on delta wings revealed their inherent advantages at supersonic speeds, such as low drag and improved stability. However, these early delta wings suffered from certain limitations, including high landing speeds and challenging low-

speed handling characteristics. The double-delta configuration emerged to address these shortcomings while retaining the benefits of the delta wing at higher speeds.

The advantages of the double-delta wing design are documented in the available literature, though less in numbers. High-fidelity computational studies have provided detailed insights into the complex flow fields and performance characteristics of these wings, particularly in regimes relevant to micro air vehicles (MAVs) and flexible wing applications. Wind tunnel testing has also been crucial for validating the aerodynamic benefits, with researchers exploring concepts like other high-lift mechanisms.

1.1 Overview of Aircraft Wings

Aircraft wings are the primary lift-generating components of an airplane, playing a crucial role in flight dynamics and performance. The design and configuration of wings significantly influence an aircraft's aerodynamic efficiency, maneuverability, and stability. Over the years, various wing designs have been developed to optimize performance across different flight regimes, from subsonic to supersonic speeds.

1.2 Types of Wing Configurations

- **Straight Wings**: Commonly used in low-speed aircraft, straight wings provide good lift at low speeds but generate significant drag at higher speeds.
- **Swept Wings:** Swept wings are angled backward (or forward) from their root to their tip, reducing drag at transonic and supersonic speeds. The swept back design is typical in many modern aircrafts weather jet or commercial.
- **Delta Wings:** Characterized by their triangular shape, delta wings offer excellent performance at high speeds and high angles of attack. They generate strong leading-edge vortices, enhancing lift and delaying stall.

Figure 1.1 gives an idea of the above three configurations.

1.3 The Double Delta Wing

The double delta wing, also known as the cranked arrow wing, is an advanced wing design featuring two distinct leading-edge sweeps. This configuration combines a highly swept inner section with a less swept outer section, forming a distinctive "crank"

in the wing planform. This unique design offers several aerodynamic advantages, particularly in terms of lift, stability, and maneuverability.

1.4 Aerodynamic Characteristics of Double Delta Wings

1. **Enhanced Lift and Delayed Stall:** The double delta wing design generates strong leading-edge vortices, which enhance lift and delay stall, especially at high angles of attack. This characteristic is critical for improving the performance of high-speed aircraft during maneuvers.
2. **Improved Maneuverability:** The configuration provides better maneuverability and stability, making it ideal for fighter jets and high-performance aircraft that require agile flight capabilities.
3. **Aerodynamic Efficiency:** By optimizing the distribution of lift and reducing drag, the double delta wing maintains aerodynamic efficiency across a wide range of flight conditions, including subsonic, transonic, and supersonic speeds.

1.5 Applications of Double Delta Wings

Double delta wings have been employed in various high-speed aircraft designs, most notably in combat and supersonic transport aircraft. Examples include:

- **Saab Viggen:** A Swedish multirole fighter aircraft that utilizes a double delta wing for improved maneuverability and high-speed performance.
- **Concorde:** A supersonic passenger jet that leveraged the aerodynamic benefits of the double delta wing to achieve efficient supersonic flight.
- **Space Shuttle Orbiter:** The double delta wing design contributed to the orbiter's aerodynamic efficiency during re-entry and landing phases.

1. **Double Delta Wing Shape:** Figure 1.2 shows the typical planform of a double delta wing, highlighting the distinct angles of the inner and outer wing sections.

2. **Vortical Flow:** Figure 1.3 illustrates of the vortical flow structures over a double delta wing, demonstrating how the strake and wing vortex generated and lift produced.

3. **Aircraft Example - Concorde:** The Concorde, a famous supersonic passenger jet, utilized a double delta wing to achieve efficient supersonic flight (Figure 1.4).

The double delta wing represents a significant advancement in aircraft wing design, offering a blend of high lift, delayed stall, and enhanced maneuverability. Its application

in various high-performance aircraft underscores its importance in the field of aerospace engineering. This thesis aims to delve deeper into the aerodynamic principles, design considerations, and practical applications of the double delta wing, contributing to the ongoing research and development in this area.

Motivation and Importance of Present Work

Delta wing aircraft primarily operate at very high speeds for the majority of their flight time. However, these wings also encounter low Reynolds number conditions during takeoff and landing. Similarly, in military applications, these wings frequently experience low Reynolds number environments during in-flight maneuvering or acrobatic maneuvers, in addition to landing and takeoff. The substantial influence of wings on military applications has resulted in these studies becoming increasingly restricted, confidential, and difficult to access in past years.

In recent years, some experimental data have become available in the open literature, specifically for comparatively high Reynolds number operational scenarios of these types of wings. Interestingly, very limited data under low Reynolds number conditions are publicly available regarding delta or double delta wing configurations. In recent times, Remotely Piloted Vehicles or Unmanned Aerial Vehicles have been under development for use in surveillance, sampling, and monitoring applications in military and scientific contexts. These vehicles operate across a broad spectrum of Reynolds numbers, with many UAVs required to function at Reynolds numbers significantly below half a million [11]. These particular low subsonic speed operating conditions introduce specific design requirements.

The primary motivation of the current study is the experimental investigation of the aerodynamic properties of a double delta wing configuration under varied orientations. Concurrently, extensive numerical experiments have been conducted to facilitate comparison and refinement.

Outline of the Thesis

This report investigates the flow field characteristics of a double delta wing model. The study employed a variety of experimental techniques to analyse the flow field. Additionally, three-dimensional numerical simulations were conducted under conditions similar to the experiments. The observations from both experimental and numerical methods were used for comparative investigation and analysis. The thesis is structured in seven chapters.

- **Chapter 1** is about the introduction on different wing shapes and configurations and the aerodynamics. Special emphasis was given to double delta wing and its origination. It also discussed about motivation, importance and usefulness of double delta wing configuration is also provided.
- **Chapter 2** deals with the survey of available (or declassified) and relevant literature available in public domain regarding different wing design under subsonic operating condition. Literatures on double delta wing were also reviewed in this chapter to assess the problem statement. Along with this, the scope of the present study has also been outlined.
- **Chapter 3** contains discussion about experimental facility and instrumentation needed to examine the flow field structure. Facility part of this chapter discusses about facilities available to successfully conduct the experimental findings. Instrumentation includes the discussion about data processing and the uncertainty in measurement and of instruments.
- **Chapter 4** discusses about numerical technique and procedure. Numerical technique and procedure encompass discussion about 3-dimensional turbulence model used along with its mathematical formulation and related steps to perform numerical simulation staring from generation of CAD model of the wing. In this chapter, grid independence study and model independence study have also been discussed.
- **Chapter 5** discusses and analyse the data collected through various different experimental methods. Several different representations of results extracted from experimental methods are used for the discussion.
- **Chapter 6** elaborates on the comparison between results obtained from experimental methods and computational simulation. Furthermore, expand

upon the conjectures formed from discussion made using experimental results. Comparative investigation of results from different experimental methods alongside results deduced from numerical simulation is discussed here. Finally, to get a comprehensible visualization of the whole flow field numerically generated visualization results are discussed.

- **Chapter 7** has the conclusion drawn from the present thesis. The scope of future work on this topic is also discussed along with the drawbacks of the methods implemented in the present investigation.

After Chapter 7, a **Reference** section is added. This section lists out all the necessary documents referred to or consulted during this study or presenting this thesis.

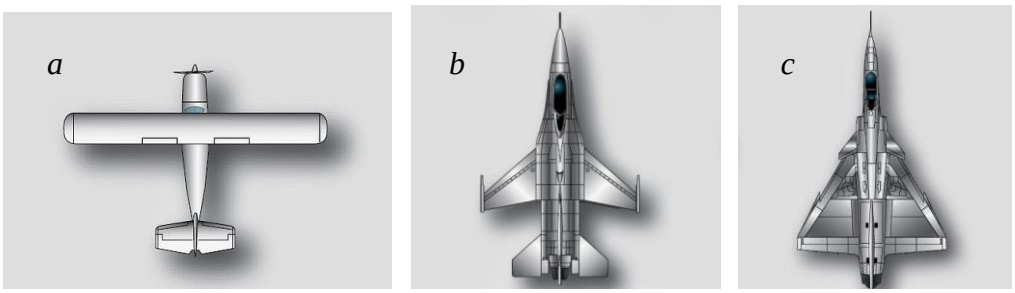

Figure 1.1 Different wing configurations, (a) straight wing, (b) swept wing, (c) delta wing

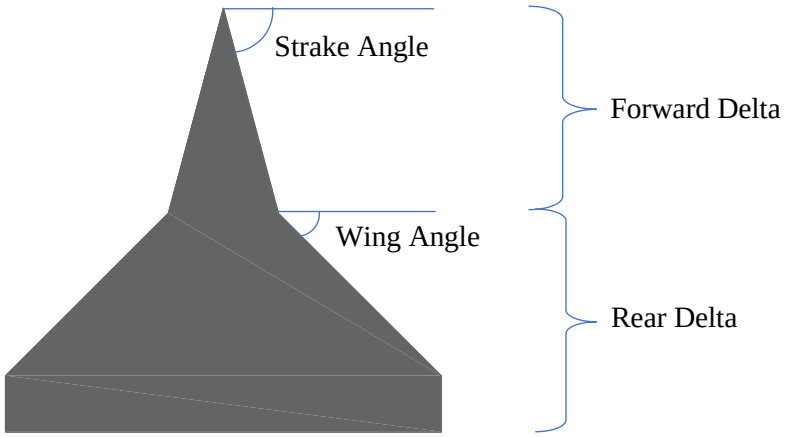

Figure 1.2 Typical planform of a double delta wing

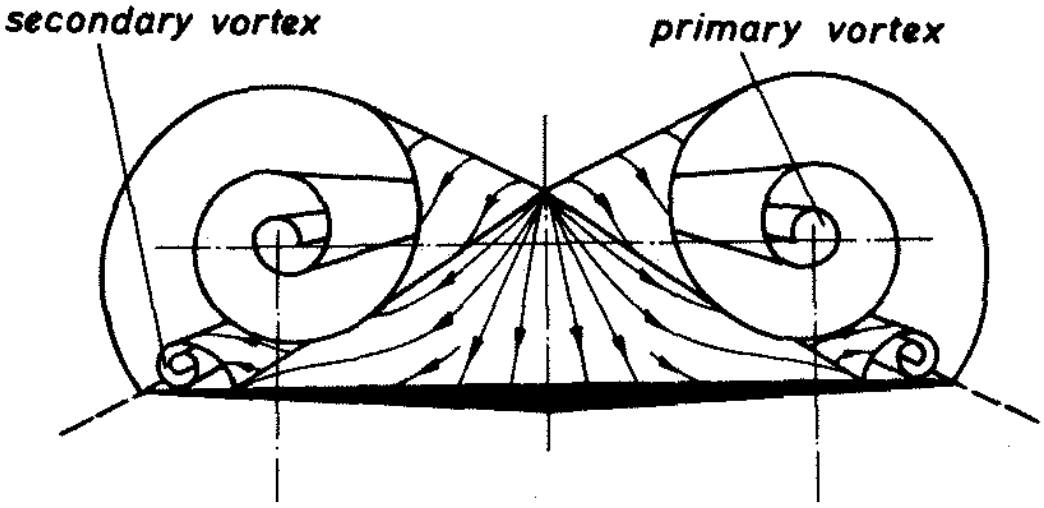

Figure 1.3 Illustration of vortex formation in double delta wing [68]

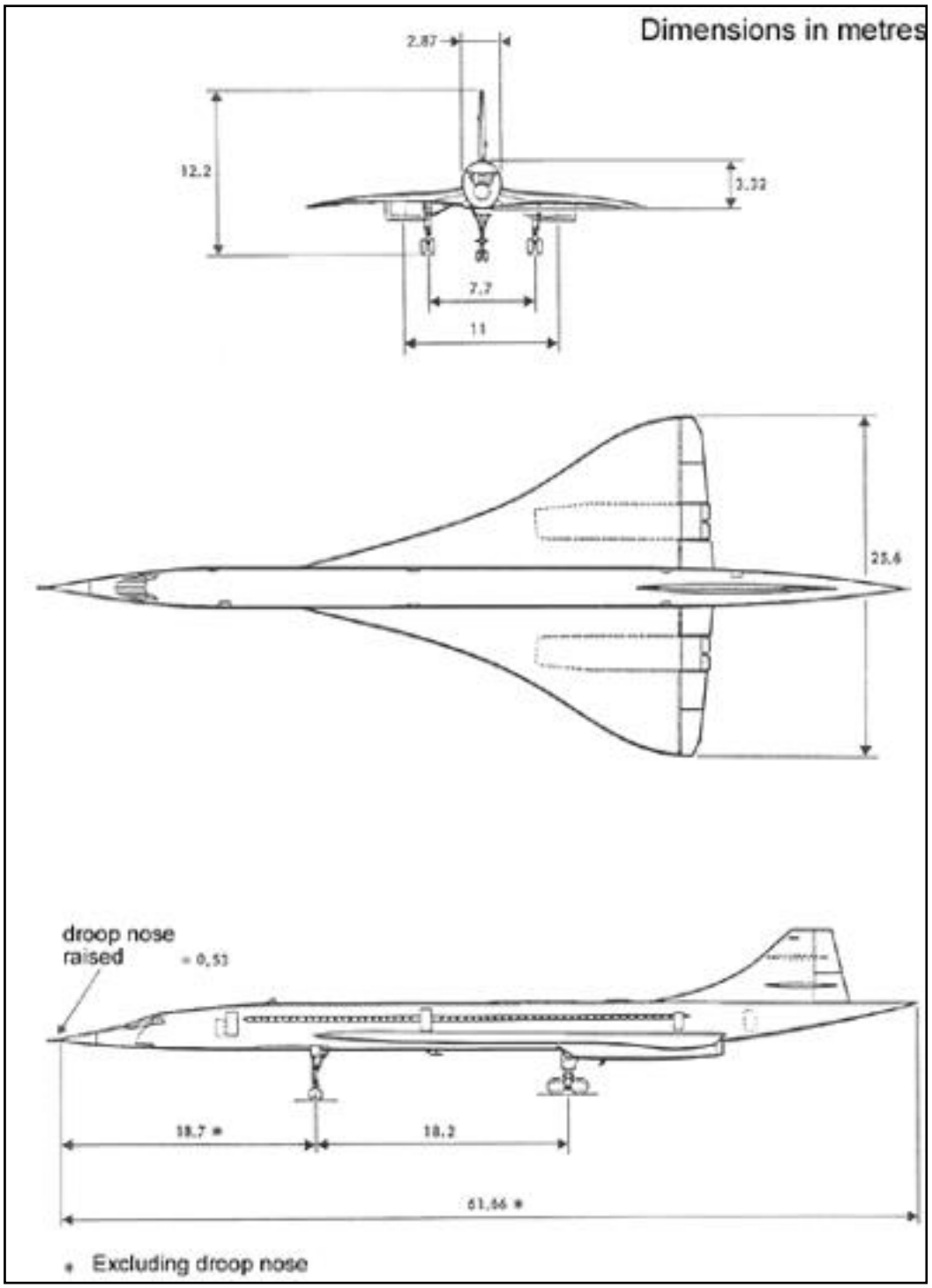

Figure 1.4 CONCORD uses double delta wing planform [12]

CHAPTER 2

Literature Review

The double delta wing configuration has been a subject of extensive research in the field of aerodynamics, particularly in the subsonic regime. The unique design of the double delta wing, with its two distinct leading edges, offers intriguing fluid dynamic characteristics that have been explored through both experimental and computational studies.

One of the key aspects of the double delta wing's performance in the subsonic regime is its aerodynamic character. Studies have shown that the vortical flow structures that develop over the wings can lead to enhanced lift and delayed stall, particularly at high angles of attack. As demonstrated through numerical simulations, the reorganization of these vortical structures and the resulting suction regions near the wing's apex can contribute to this lift enhancement.

The oil flow visualization technique has been a valuable tool in understanding the complex flow phenomena over the double delta wing. By observing the oil patterns on the wing's surface, researchers have been able to infer the nature of the boundary layer and the formation of primary and secondary vortices. These visualizations have provided insights into the evolution of the flow field, including the interaction between the vortices and the wing's surface, as well as the effects of wing geometry and angle of attack on the overall flow structure.

The velocity and pressure distribution over the double delta wing are also of critical importance in understanding its aerodynamic performance. Experimental investigations, often employing techniques such as particle image velocimetry (PIV) and pressure tapping, have revealed the intricate flow features and pressure gradients that develop over the wing. These data have been used to validate computational fluid dynamics (CFD) simulations, which in turn have been used to provide a more comprehensive understanding of flow physics.

The published literature on double delta wing performance in the subsonic regime offers some information, from experimental studies to numerical simulations. These

sources have collectively contributed to our understanding of the complex flow phenomena and their influence on the overall aerodynamic characteristics of this unique wing configuration.

The three main types of research are theoretical, computational, and experimental. Theoretical research is grounded in established theoretical principles that can be simple or based on strict assumptions. It generally has lower costs compared to other forms of research but the results must be validated experimentally for complex flow patterns and geometry. Theoretical models involve a large number of calculations, while with advancements in computational power and numerical schemes, the use of a computational approach has become more feasible. However, despite these developments, numerical approaches may not always provide exact solutions. Experimental analysis continues to be essential for any research despite its associated costs and errors. Both theoretical and computational approaches should be complemented by experimental studies. For aerodynamic experiments on wing or airfoil sections, a wind tunnel is the primary instrument required. Wind tunnel model studies are essential prior to manufacturing aircraft prototypes. Some companies made own wind tunnels for experimenting on airfoils and wings. However, the limited publication of experimental or numerical data is often due to confidential reasons. NASA declassified some results, making a wealth of experimental data available in Abbott and Doenhoff's [13] "Theory of Wing". This has assisted researchers in validating experimental data through analytical and numerical analysis.

2.1 Analytical Study

In his pioneering study, Polhamus [14] devised a novel framework for understanding the intricate dynamics of vertex slip along the sharp leading edges of Delta Wings. Through a nuanced analogy to leading-edge suction, he sought to mitigate the formation of separation vortex and its associated drag penalties. This framework provided a methodological breakthrough for calculating the vortex lift of double delta wings, validated rigorously against empirical and computational data. Its foundation lay in the elegant alignment between vortex lift and leading-edge suction within the framework of potential flow.

By integrating this analogy with an advanced adaptation of potential flow theory,

accounting for nonlinear effects and the attenuation of lift components, Polhamus achieved remarkable predictive accuracy. This method facilitated comprehensive predictions of total lift across a broad spectrum of delta wing configurations, including high angles of attack. The proposed equivalence between vortex lift and leading-edge suction offered engineers a systematic approach to aerodynamic design, transcending conventional limitations. Across varied angles of attack and aspect ratios, this framework provided invaluable insights for optimizing performance and efficiency.

Furthermore, in the realm of supersonic speeds, the framework accurately anticipated a reduction in vortex lift with increasing Mach number, culminating in a complete estimation when the Mach line coincided with the leading edge. This insight provided a crucial foundation for navigating the complexities of high-speed aerodynamics.

2.2 Experimental Study

Li's [15] experimental study in a water tunnel focused on vortex development and bursting phenomena on baseline and modified double delta wing models. Tests covered flow velocities up to 1.0 ft/sec and angles of attack from 0° to 50° in 5° increments, using dye injection for visualization. Findings showed smooth, attached flow at lower angles (<10°). At 15° AoA, strake and wing vortices were well-developed and intertwined. Increasing AoA to 20° led to earlier vortex coiling. The modified model's fillet promoted earlier coiling but had no effect at high angles of attack. In dynamic conditions, both models exhibited earlier strake vortex bursts during pitch down motions compared to static conditions.

Study of Wood et al. [16] examined how geometry affects Delta wing vortices and aerodynamics at supersonic speeds. Using a range of delta wing models tested at Mach No.from 1.7 to 2.0. Tests were conducted at Langley's Unitary Plan Wind Tunnel, capturing surface pressure data, vapor screen images, and oil flow photographs. Findings showed attached flow at 0° AoA, with the diamond airfoil exhibiting abrupt expansion around its maximum thickness ridge line. At 8º AoA, thicker sections delayed leading-edge separation, correlated with an angle of attack approximately half the leading edge included angle. At 16º AoA, all wings displayed leading-edge vortex influence with secondary separation. Computer Enhanced Photographs confirmed the presence of a cross-flow shock on the lee-side of the diamond airfoil. Despite pressure

differences between circular-arc and diamond airfoils, resultant flow characteristics remained similar.

A low-speed wind tunnel study on a 76º/40º double-delta wing was conducted by Verhaagen et al. [17] to understand vortical flow behavior and validate Computational Fluid Dynamics (CFD) methods. Tests covered angles of attack from -10º to 25º and Reynolds numbers from 0.5 to 1.5 million. Data from flow visualization, upper surface pressure recordings, and flow field surveys were collected at NASA Langley Research Center's Basic Aerodynamics Research Tunnel (BART). The tunnel features a test section with 1.5 million cells and extensive flow conditioning. CFD modeling, based on compressible thin-layer Navier-Stokes equations, was compared to experimental results.

Hebber et al. [18] conducted experiments on a cropped double delta wing in a water tunnel, focusing on vortex interaction, bursting, and control at high angles of attack (AoA). The study used dye-injection techniques and evaluated the effect of fillets on vortex trajectories, interactions, and breakdown on the leeward surface, with variations in sideslip angle. Four wing shapes were tested: a baseline model and three derivatives with fillets increasing wing area by 1%. Results showed at low AoA, vortices coiled up due to interaction, while at high AoA, one vortex often burst before interaction, triggering the burst of the other. At 10° AoA, the strake vortex core of the baseline model was closer to the centerline than those of filleted models. As AoA increased from 10° to 30°, vortex cores moved inboard for all models, with a delayed inboard movement for the diamond-fillet model. Vortex interactions occurred at specific locations along the wing, with no interaction at 30° AoA due to vortex bursting. The study noted that vortex core shedding from a sharp leading edge and its burst location were insensitive to Reynolds number, but interactions between vortices were Reynolds number dependent. During pitch-down motion, strake vortex bursting occurred earlier relative to static conditions, resulting in an increased equivalent angle of attack. Conversely, during pitch-up motion, strake vortex bursting occurred further downstream compared to pitch-down motion and static conditions.

An experimental study employing the Pressure Sensitive Paint (PSP) technique to visualize aerodynamic effects on a double delta wing aircraft model was done by Klein and Engler [19]. Additionally, they utilized an optical pressure measurement system.

PSP, complemented by the laser sheet method, facilitated precise surface pressure measurements, providing insights into flow behavior over the wing in a wind tunnel. This technique, emerging at the time of the study, enabled instantaneous pressure distribution recording, facilitating accurate analysis of vortex dynamics with minimal error. The study successfully identified vortex breakdown processes and Kelvin-Helmholtz instabilities, particularly noting vortex breakdown occurring at high angles of attack near primary vortices and the leading edge.

Pashilkar [20] proposed a straightforward aerodynamic modeling approach for the longitudinal static characteristics of a simple delta wing, parameterizing surface pressure distribution. The model demonstrated strong independence of normal force and pitching moment coefficients on leeward flow, extending successfully to wing/body combinations, consistent with experimental data. It serves as a useful first approximation for load estimation, with plausible parameters and potential for further refinement, including extension to model unsteady aerodynamic pressures.

The effects of linear, diamond, and parabolic fillets on a double delta wing across Mach 0.18 to 0.7 and angles of attack from -4° to 42° was investigated by Gonzalez et al. [21] at NASA Langley's High-Speed Tunnel. Measurements revealed increased lift coefficients and reduced induced drag with fillets, primarily affecting suction and vortex footprint broadening. Lift increased with Mach number, while drag decreased. All fillets augmented lift across various angles of attack, with the parabolic fillet generating the most lift, and the linear and diamond fillets enhancing lift to varying degrees at different angles of attack.

Sohn and Jang [22] conducted experiments to visualize and measure vortical flow over a double delta wing. They used off-surface visualization, 5-hole probe, and hot film measurements, with an AoA range of 10° to 30° and side slip angles from 0° to -15°. The study showed good agreement between flow field measurements and visualizations, revealing vortex behavior and interactions, particularly noting changes in vortex movement and coiling at non-zero side slips and different angles of attack.

Gai et al.’s [23] wind tunnel and water studies aimed to elucidate the fluid mechanics of strake and wing vortex interaction on a generic double-delta wing, including investigations of passive control using fences. Various diagnostic methods were

employed, showing different interaction mechanisms and their effects on vortex flow, such as enveloping and spiraling or coiling interactions.

Lee and Kim [24] utilized computational methods to investigate vortical flows over sharp-edged delta wings with and without leading edge extensions. The study provided insights into the effects of angle of attack and yaw angle on vortex development and aerodynamic characteristics, showing reasonable predictions compared to wind tunnel measurements, particularly noting the stabilizing effects of leading-edge extensions on wing vortex behavior.

Erickson and Gonzalez's [25] experiment focused on vortex flow manipulation on a double delta wing using Pressure Sensitive Paint (PSP) technique. Tests were conducted on a 76°/40° wing at varying AoAs and Mach numbers. Different fillet shapes were fabricated to manipulate vortex flows, with PSP technique providing static pressure measurements. Laser vapor screening was employed for visualizing vortex sheets, lines of separation and attachment, revealing changes in pressure coefficient with different Mach numbers and span-wise locations.

The influence of a center body on the vortex flow of a unique double-delta wing was investigated by Sohn and Chang [26]. Through off-surface flow visualization and wing-surface pressure measurements, they analyzed a specially shaped double-delta wing formed by attaching a leading-edge extension to a 65° sweep delta wing. Visualization results indicated that the presence of a center body slightly advanced coiling interaction of wing and extension vortices. Quantitative analysis of wing-surface pressure measurements highlighted prominent effects of the center body, particularly at higher angles of attack and sideslip angles.

Nath et al. [27] focused on the distinctive feature of delta wings characterized by leading edge vortices, which introduce nonlinear forces and moments, especially at high angles of attack where vortex breakdown occurs. Experimental and numerical investigations aimed to understand these complex flow fields, crucial for designing highly maneuverable aerospace vehicles.

Atazhbaz and Ommian [28] conducted experiments on a 65° delta wing at a low subsonic wind tunnel facility, varying angle of attack, sideslip, and speed. Oil and tuft flow visualization along with static pressure measurements captured various flow

features. Three-dimensional numerical simulations provided insights into vortex breakdown, showing asymmetric behavior with side slip. Surface flow visualization and laser sheet visualization techniques were employed. Suction pressure distributions were measured under sideslip conditions, showing good agreement between computed and experimental pressure distributions at low angles of attack.

Gopinath and Parammasivam [29] performed experiments on a 60° delta wing, focusing on the effect of leading-edge radius on flow phenomena. Pressure measurements revealed changes in flow separation and vortex formation with different leading-edge profiles and angles of attack.

Nettelbeck [30] investigated wing rock on highly swept slender wings, employing pressure measurements and flow visualization on a 76°/40° double delta wing. Unsteady pressure measurements were taken to understand vortex behavior during wing rock motion, facilitating future research on flow management techniques to suppress wing rock.

Al-Garni et al. [31] conducted experimental and numerical investigations on 65° delta and 65°/40° double-delta wings, comparing results with theory and experimental data. The study provided insights into lift, drag, and vortex breakdown characteristics, showing good agreement between experiments, numerical predictions, and theoretical calculations.

Majumdar and Saha [32] studied the surface flow pattern on a double delta wing experimentally and computationally, using oil flow visualization and CFD analysis. Results highlighted vortex behavior and flow patterns at different angles of attack, providing valuable insights for aerodynamic analysis and design optimization.

Saeed [33] conducted experimental and numerical studies on side-slipping delta wings, focusing on aerodynamic characteristics at various pitch and sideslip angles. Results compared well with literature and theoretical predictions, offering comprehensive understanding of wing behavior under different flight conditions.

Naimuddin et al. [34] investigated a compound delta wing experimentally and computationally, focusing on leading edge vortices and their characteristics at different

angles of attack. Surface oil flow visualization and CFD analysis provided insights into vortex behavior and shedding, crucial for wing design and control optimization.

Ekaterinaris and Schiff [35] conducted numerical and experimental investigations on a 76°/40° double delta wing, focusing on strake and wing vortex interactions and vortex breakdown. Pressure sensitive paint was used to study the effect of wing fillets on vortex-induced static pressure.

Aswin Kumar et al. [36] examined the flow field characteristics of a sharp-edged 81°/45° double delta wing through numerical and experimental methods, covering angles of attack from 0° to 30° in a subsonic wind tunnel and using FLUENT software for simulations.

Gai et al. [37] conducted wind tunnel and water tunnel studies to clarify the fluid mechanics of strake and wing vortex interactions on a 76°/40° double delta wing, including passive control studies using apex and kink fences. Diagnostic methods included laser sheet flow visualization, fluorescent dyes, and pressure sensitive paints. Interaction mechanisms included enveloping and spiraling/coiling interactions.

Renac et al. [38] performed experimental and numerical research on leading edge vortices and vortex breakdown on a delta wing. Experiments were conducted in a subsonic, closed-return wind tunnel with a rounded leading edge delta wing. Objectives included characterizing vortical structures and testing a device to affect vortex structure and breakdown location. Chaderjian and Schiff [39] investigated pressure measurements on a 65° delta wing across a range of flow conditions, from attached flow to fully stalled flow, providing data for validating Computational Unsteady Aerodynamics codes.

Water tunnel flow visualization experiments on low aspect ratio cropped wings was examined by Wang and Tu [40] at low Reynolds numbers. Results indicated that sweep angle influences leading-edge vortex formation and development, with dual vortex structures observed at higher sweep angles and certain angles of attack.

Kaurinkoski and Siikonen [41] studied transonic flow past a round leading-edge cropped delta wing using Reynolds-averaged Navier-Stokes equations. The study

analyzed laminar and turbulent flows at Mach 0.85 and varying Reynolds numbers, employing three algebraic turbulence models.

Experimental and computational studies on an 81°/45° blunt leading-edge double delta wing was conducted by Sreenivasulu et al. [42] at Reynolds number 2.54 × 10^5 and velocities of 16 to 20 m/s. Techniques included oil flow visualization, tuft flow visualization, and static pressure measurements, examining the effects of angle of attack, speed variation, and vortex breakdown location, and comparing results with a single delta wing with the same t/c ratio.

2.3 Numerical Study

Muller and Rizzi [43] simulated a 65° delta wing using a 3D Navier-Stokes laminar compressible flow solver. The wing featured rounded leading edges and cropped tips. The finite volume technique was used for spatial discretization, employing a novel variant for viscous fluxes. Time integration was performed using an explicit three-stage Runge-Kutta scheme with local time steps. The simulation computed primary and secondary separation vortices at transonic speeds, comparing results with experimental data and Euler solutions. The study investigated Reynolds number effects at an angle of attack of 10° and Reynolds number of 2.38x10^5, finding that higher Reynolds numbers brought the vortices closer to the leading edge.

Hsu and Liu [44] investigated vortical flows over a thin round-edged double-delta wing with an 80°/60° sweep and aspect ratio of 2.05 using 3D computations with an implicit upwind-relaxation finite difference scheme. The study examined grid and angle of attack effects on Navier-Stokes computations at a Reynolds number of 1.3x10^6. Fine-grid computations accurately simulated vortex formation, interaction, and breakdown, with computed lift coefficients and spanwise surface pressure distributions agreeing well with experimental data up to 25° AoA.

Allan et al. [45] conducted CFD investigations on wind tunnel interference effects on delta wing aerodynamics, finding that tunnel walls promote vortex breakdown and affect lift, drag, and pitching moments. The presence of side walls increased the effective incidence of the wing, delaying vortex breakdown and increasing the helix angle of vortices. These effects were influenced by model span to tunnel width ratio,

sweep angle, and AoA.

Luckring [46] performed experiments and numerical investigations on a 65° delta wing, studying Reynolds number, compressibility, and leading-edge bluntness effects. Results showed that increasing Reynolds number delayed leading-edge vortex separation, while increasing Mach number promoted it. These effects were significant at angles of attack representative of manoeuvring conditions.

Singh et al. [47] used Euler computations to simulate transonic flow over a cropped delta wing with a deflected aileron at M=0.9 and AoA=1° and 3°. Comparisons with experimental data and other computational results showed good agreement, although further improvements were needed to capture the suction peak accurately.

Hamidi and Rahimi [48] conducted numerical studies on a 76°/45° double-delta wing at high angles of attack using FLUENT. The study focused on vortex formation, interaction, and breakdown characteristics at angles of attack from 10° to 40°, finding that the double delta wing maintained lift at high angles of attack.

Liu et al. [49] applied an improved delayed detached eddy simulation (IDDES) model based on the k-ω SST turbulence model to predict unsteady vortex breakdown over an 80°/65° double delta wing at angles of attack from 30° to 40°. The study validated the model with NACA0021 wing data and investigated unsteady properties such as force frequencies and pressure fluctuations. Results showed dominant modes with Strouhal numbers of 1.0 and 0.7 at different AoAs, and the vortex breakdown moved upstream and downstream alternately.

Aerodynamic predictions can be achieved through theoretical, experimental, or numerical approaches. This dissertation will focus solely on the latter two methods. The existing literature, that were consulted, reports on various experimental investigations and numerical predictions These studies have been conducted to gain fundamental understanding as well as to assess the performance of prototype designs. Summaries of research work related to of vortex flow aerodynamics have been provided by Squire [50] and Luckring [51].

2.4 Scope of Present Work

Summarizing, the fundamental character of these experimental and numerical inquiries is limited and private. Specifically, the outcomes and data from practical research are scarcely accessible to the public. Despite efforts to understand the basic physics behind these low-speed phenomena problems, solutions for military aircraft have largely been derived empirically through wind-tunnel studies based on a qualitative understanding of the involved phenomena.

A thorough analysis of limited available literature indicates that there has been minimal research published in public sources about the forces generated by wings and airfoils at Reynolds numbers around 10^5. In this range, wing performance significantly decreases, but potential improvements may occur at slightly higher Reynolds numbers. The issues of boundary instability over a double delta wing, particularly when operating at low subsonic speeds, are still in an early stage with many aspects remaining unknown from publicly available literature. A comprehensive study examining the three-dimensional flow structures and interactions of vortices for the wing need further investigation. The present investigation will try to address some of the flow features around a double delta wing at a Reynolds Number around 10^5.

In order to expand the knowledge of flow field dynamics and widen the understanding of double delta wing properties, both experimental and numerical investigations were conducted on a wing model having dimensions as mentioned in Chapter 4 at very low subsonic conditions. The current study has been segmented as follows:

1. Implementation of flow visualization techniques on the wing model's surface to understand strake and wing vortex generation patterns and its interaction with the flow field.

2. Assessment of forces generated by a fixed low Reynolds number operating condition on a double delta wing.

3. Measurement of velocity distribution over different heights and orientations on the leeward surface of the wing to understand flow structure over its surface.

4. Execution of surface pressure measurement techniques to observe the impact of a shape on surface pressure distribution, which governs force generation.

5. Utilization of three-dimensional computational simulation via commercially available CFD software for predicting airflow around the wing model. Comparative analysis between experimental data and numerically computed results was subsequently done for further investigation.

CHAPTER 3

Experimental Facility and Instrumentation

Experimental investigations were carried out in a subsonic open circuit type wind tunnel. The wind tunnel is located in the Fluid Mechanics and Machinery Laboratory on the 1st floor of the Department of Power Engineering of Jadavpur University, Kolkata, India. A model of cropped double delta wing was designed and fabricated for the present investigation. The model was suitably instrumented in order to measure desired parameters. The tunnel was provided with options to measure pressure, velocity, etc. The maneuvering device to control the pitching movement and sideslip of the test wing was also employed. The following sections will discuss experimental apparatus employed and related descriptions of the equipment used in the experiment. A brief account of facilities is also given along with the instruments used for measurements.

3.1 Wind Tunnel

The wind tunnel used in the present experimentation is an open circuit, subsonic, low turbulence tunnel as shown in Plate 3.1. Two counter-rotating fans run the tunnel. The details of the wind tunnel in the form of schematic diagram is shown in Figure 3.1. A honeycomb mesh is provided at the inlet to reduce the turbulence level. Subsequently two nylon screens are included in the settling chamber. Test section includes a removable plexiglass on three sides of wall for easy access as well as to facilitate flow visualization. Fan section is mounted on a concrete isolation block to reduce the transfer of vibration to the tunnel walls. The generated velocities are very stable over time and the flow across the test section is reasonably uniform with low turbulence intensity. The tunnel can achieve free-stream velocity upto 15m/s. turbulence intensity of the tunnel is less than 0.1% of mean stream velocity.

The tunnel free-stream velocity is obtained by a Pitot tube mounted on one of the side walls, which is connected to the electronic manometer.

Some necessary modifications were performed on the tunnel walls for the installation of the double delta wing. A slot was provided along the centreline of the bottom wall of the tunnel at the end of the test section. A traversing mechanism (model positioning

system), describe in section 3.3.1, was positioned beneath the test section and to a side of the slot to attach the balance and to traverse it to the required position. Some slots were also cut on the top wall to provide the pressure probe within the test section as described in section 3.3.2

3.2 Model

The wing model in this experiment is a 75°/45° cropped double delta wing. The geometry of the model is given in Figure 3.2. The model is made out of composite material. The windward surface is made up with plexiglass and the other side, called as leeward side is with flat industrial grade aluminum plate. The model is having sharp leading edge. The leading edge is single beveled with 20° whereas the trailing edge is made blunt. The root chord of the wing model is 189mm and the span is 194mm. Thickness of the wing is 10mm. Aspect ratio is 2.36. The windward beveling of the model uniformly done at 20° and a sharp leading edge is provided to ensure the proper formation of the leading-edge vortices, as reported by Miau et al. [52]. On the other hand, the leeward side is made flat. In the wind tunnel, the model is positioned upside down, that is to say the leeward side facing up with the help of model positioning system from the rear of the model. The sector of the model positioning system was attached to the model with screws, which were countersunk into the model's leeward surface. Any irregularities or rough surfaces in the proximity of the screws were filled up with suitable filler, so that a smooth suction surface was produced. Suitable holes were tapped to accommodate different attachments and instruments with the wing following the same concept. The blockage ratio within the tunnel due to model positioning was calculated nearly 4.93% in the worst case, which was for the wing at $\alpha = 30°$. Some basic parameters of wing model are tabulated in Table 3.1.

3.3 Traversing System

Two different traversing arrangements were employed during the experiment. One beneath the wind tunnel to facilitate model wing movement along with the balance during experimenting aerodynamic characters and with normal attachment prepared in-house for force, velocity and other measurements. Another traversing was employed on top of wind tunnel for positioning the pressure probe.

3.3.1 Model Positioning System

A specially designed model positioning system is procured for the purpose of traversing the balance with the model from Hitech Engineering Equipment, Bengaluru (Plate 3.2). It is a two axis system with a motorized movement, pitch angle (α) ranging between -10° to +30° and hand operated yaw angle (β) with range ±22.5°. The centre of the arc sector coincides with the balance centre and is designed to meet at the centre of the test section of the wind tunnel also. The whole assembly is mounted below the test section with suitable footings with clamps, nuts and bolts so that only the sector enters the wind tunnel through the slotted opening in the bottom wall of the test section. It was ensured that when the sector is at 0°, it coincide the tunnel central axis.

The model can be positioned to an angular accuracy of ± 0.1°. A sting made out of high strength alloy steel is also attached to the sector. The rear end of the balance is fitted to the sting attachment using screws. Figure 3.3 shows a schematic of model positing system.

For giving motorized motion to pitch angle, a stepper motor arrangement is employed. This system is also controllable with PC interface. A specially designed software package is supplied with data acquisition system used for this. End limit switches are provided to stop the movement at the extreme end locations. A mechanical scale is also provided for manual checking of set angle. For yaw motion, a handle wheel with a pointer is supplied to facilitate the angle setting.

3.3.2 Pressure probe traverse mechanism

Another traversing facility was fabricated in house to accommodate the movement of pressure probe within flow domain (Plate 3.3). This facility has three degrees of freedom such that it can move the probe in span wise, chord wise and perpendicular to flow direction. Movements to all three directions are controlled by three AC synchronous motors that can rotate in both clockwise and anticlockwise direction. A panel is provided to control the movements of the motors. Each single-phase motor can produce a torque of 10kg.cm and 0.008HP when operated at 60rpm in 240V, 50Hz with maximum current of 125mA. Lead screw is provided in each direction for precise positioning of the probe in desired location. Graduated rulers are fitted with the lead screws with a pointer to measure distance of movement.

3.4 Balance

A flat plate type 3-Component strain gage-based balance is used to measure the lift, drag and moment on the wing experiencing air flow. The balance has a maximum plate thickness of 4mm and length of 210mm. It is made out of Alloy Steel 17-4-PH. The balance (Plate 3.4) consists of 2 normal force gage stations for determination of normal force and pitching moment, and one axial force measuring bridge. Balance center is located at the center of the 2 normal force-measuring units. All gage sections are of the bending type. Four strain gages are bounded to each of the gage station to form 4 active arms of a Whetstone bridge.

Standard foil type transducer class strain gages have been used in the balance. The gages are temperature compensated for steel with a nominal resistance of 350 Ohms and a gage factor of 2. All the gages are water proofed.

3.4.1 Calibration of Flat plate type 3-Component Strain Gage Balance

A simple calibration rig was used for balance calibration. The calibration rig has provision for movement in the pitch and roll planes. A voltmeter (DVM) has been used to accumulate the data from the strain gage bridges. For calibration, direct acting dead loads have been used.

During calibration, to load the balance accurately, it is necessary is to have calibrator body, which will transmit the loads to balance, should follow the same manner as the model would transmit the loads during the tunnel experiment. Loading points on the calibration body are positioned precisely, such that they act at stations N_1, N_2, where individual loads N_1, N_2 can be applied. Similarly, provision is available for applying pure positive axial force.

The model end of the balance is fixed to the calibration body. This assembly is attached on to the Calibration Rig with suitable fixture. The calibration body is then loaded with only a single component of load say, N_1 or N_2 in steps of, say, 10% of the full load and output read outs of all the bridges are noted. In order to apply only one component of the load, the following care has to be made. For example, for applying N_1 or N_2, the orientation of the calibration body must be such, that the vertical load due to dead weights should point the direction of N_1 or N_2. The position of the calibration body has to be maintained in horizontal position even under load. With this procedure, pure

positive N_1 and N_2 loads (dead weight) can be applied individually in the pan attached to the calibrator. Negative N_1 and N_2 load can be applied by turning the balance by 180^0 to that of positive direction and then re-fixing the calibration attachment. The calibration body is leveled after every loading to ensure that only one pure component load can be applied. For axial force calibration, the balance along with the calibration body would be mounted perfectly directing upwards.

The output from each of the bridges for every loading is acquired by the Digital Volt Meter. All output voltages are normalized in reference to the excitation voltage. A linear least square fit for the deviation of the normalized yields with respect to a particular load is obtained. The values of the proportionality constants, which form the coefficients of the matrix to be described later, have been designed to be self-explanatory. For example, c_{n1n1} refers to the constant of proportionality for the N_1 bridge output due to N_1 loading; c_{n2af} refers to the constant of proportionality for the N2 bridge output due to A_f loading.

When the Balance involves all the components of loading, the outputs in the bridges are expressed by,

$$O_{Af} = C_{Af\,Af}\,Af + C_{Afn1}\,N_1 + C_{Afn2}\,N_2$$

$$On_1 = C_{n1Af\,Af} + C_{n1n1}\,N_1 + C_{n1n2}N_2 \qquad \ldots\ldots\ldots\ldots\ldots\ldots \quad 3.1$$

$$On_2 = C_{n2Af\,Af} + C_{n2n1}\,N_1 + C_{n2n2}N_2$$

i.e.

$$[O] = [C]\,[F] \qquad \ldots\ldots\ldots\ldots\ldots\ldots \quad 3.2$$

Where,

[O] is the output matrix

[C] is the Calibration Coefficients matrix.

[F] is the force matrix

It is obvious from (3.2) above that,

$$[F] = [C]^{-1}\,[O] \qquad \ldots\ldots\ldots\ldots\ldots\ldots \quad 3.3$$

During calibration, when the component loads, say, N1 is applied, then we can determine the three coefficients $C_{Afn1}N1$, $C_{n1n1}N1$, and $C_{n2n1}N1$ (These coefficients in calibration are expressed in units of mV/V/kg). From the above expression, using the inverse matrix of the calibration coefficients and the measured yields from the bridge stations, the unknown forces may be calculated.

3.4.2 Determination of the Loads on the Model from the Balance Output

The directions of positive loads with respect to the balance are shown in Figure 3.4. The normal loads acting on the balance can be resolved into two forces i.e., normal force forward (N_1) and normal force aft (N_2). The pitching moment is the resulting moment of the normal loads about the balance center. The distance from balance center to normal force gages is 20 mm. Axial force acting towards the fixed end along the axis of balance is taken as positive.

If one wants the loads and moments about any reference point, say, 'M' with respect to the Model, the following procedure can be applied.

i) The loads about the balance center have to be determined using the following equations.

$A_B = A$

$N_B = N1 + N_2$

$M_{yB} = (N_1 - N_2) \times l = (N_1 - N_2) \times (20)$ Kg mm 3.4

Where, the subscript 'B' indicates forces and moments about the balance center.

ii) The experimentalist has to find the distance 'L' of his reference point 'M' in mm form the balance center. L is taken as positive if it is downstream of the balance center. The loads about the reference point 'M' can be determined using the following equations.

$A_M = A_B$

$N_M = N_B$

$M_{yM} = M_yB + N_B \times L$ (Kg mm) 3.5

Where subscript 'M' indicates forces and moments about the Model reference point 'M'

The outputs measured from the individual bridges are found to be linear with respect to the corresponding loadings. In fact the deviation of the output from the mean is less than 0.5% FS. Therefore, the balance is considered to be extremely satisfactory and calibration coefficients may be used for force measurements in the Wind Tunnel.

3.5 Probe

Various pressure probes were employed in the present study. A Pitot-static tube (Plate 3.5) was utilized to determine fluid velocities during the calibration of a three-hole pressure probe, as well as to measure air velocity along the central axis of the test section. The three-hole pressure probe was used specifically for assessing the velocity distribution over the leeward surface of the wing.

3.5.1 Three-Hole Pressure Probe

A three-hole pressure probe (Plate 3.6) was utilized to measure the velocity profile within the flow area, enabling the determination of flow direction, static pressure, and free-stream velocity. The specific probe employed in this investigation was internally designed, created, and calibrated. It comprises three stainless steel tubes with an outer diameter of 1.2mm and an inner diameter of 1mm assembled together. These tubes are then enclosed within a steel jacket tube with an approximate outer diameter of 4mm. The short tip of the 'L'-shaped probe is thin and filled with molten solder to ensure that the three holes are aligned in one line. With the longer arm measuring at 250mm and shorter arm at 4mm for its 'L' shape integrated design reduced blockage effects at measurement points by less than 3%. Figure 3.5 depicts a schematic representation of this particular type of probe used in this study.

In order to utilize data collected through a probe, defining a coordinate system is essential. This system is then used for calibration and later for measuring in an unknown flow field. The coordinate system with respect to the flow for the three-hole pressure probe can be seen in Figure 3.5. The positive yaw angle was defined using the right-hand rule by aligning the right thumb with the negative z-direction. Before performing measurements using the three-hole pressure probe, it needs to be calibrated at the flow conditions. Two different methods, null technique and non-null techniques [53] [54], could be adopted for calibration; each has its own advantages and disadvantages related to them. Due to space restrictions, such as those found in turbo-machinery applications and wind tunnel blockage situations, probes are often required to be small which introduces difficulties associated with traversing and data acquisition when used in a null technique. In this study, calibration functions are identified to determine flow angles and velocity components in a two-dimensional plane with mean velocity using the non-null technique.

3.5.2 Non-Null Technique

The null technique often requires a significant amount of time for extensive data recording and may not be feasible when probe rotation is restricted due to space limitations or other constraints. In the non-null technique, the probe is positioned at a constant pitch and yaw angle with respect to a reference line. [55] Pressure values corresponding to each hole of the three-hole pressure probe are then recorded at different locations by moving the probe through the flow field. Calibration functions are determined for specific yaw angles, both positive and negative relative to the reference. While non-null technique offers simplicity, it can encounter singularity issues during calibration for large yaw angles. The nomenclature and convention used for three-hole pressure probe calibration can be found in Figure 3.5.

The probe was calibrated in an open type, low speed, low turbulence, blow down type wind tunnel installed in the same laboratory shown in Plate 3.7. a series of manometers were employed for measuring pressure differences as shown in Plate 3.8.

The steps involved in calibrating using non-null techniques include:

i. Noting of ambient pressure and temperature
ii. Checking of alignment of manometer fluid
iii. Setting up of the three-hole probe at zero pitch and yaw with the flow
iv. Measurement of free stream velocity of the flow with a pitot tube
v. Varying the movement of the probe in yaw within certain limit
vi. Record the date
vii. Analyse the data and prepare suitable solving tool

Coefficients of calibration can be found out from the following relations

for yaw angle ($\beta > 0$) are

$$f_1 = \frac{p_3 - p_1}{p_3 - p_2} \qquad f_3 = \frac{p_2 - p_3}{p_T - p_S} \quad f_5 = \frac{p_T - p_3}{p_2 - p_3} \qquad \text{..... 3.6}$$

for yaw angle ($\beta < 0$) are

$$f_2 = \frac{p_3 - p_2}{p_3 - p_1} \qquad f_4 = \frac{p_1 - p_3}{p_T - p_S} \quad f_6 = \frac{p_T - p_3}{p_1 - p_3} \qquad \text{..... 3.7}$$

Eqation 3.6 and 3.7 are used to obtain flow properties (P_T, P_S and β) along with yaw angle. Plotting β with f_1, f_2, f_3, f_4, f_5 and f_6 with suitable polynomial fit curve will provide calibration coefficients. Correlation between velocity components u_x and u_y with respect to x and y direction of the probe coordinate and yaw angle are

$$\bar{u} = \sqrt{(p_T - p_S)\frac{2}{\rho}} \quad \ldots\ldots\ldots\ldots\ldots 3.8$$

$$u_x = \bar{u} \times cos\beta \quad \ldots\ldots\ldots\ldots\ldots 3.9$$

$$u_y = \bar{u} \times sin\beta \quad \ldots\ldots\ldots\ldots\ldots 3.10$$

The calibration curve obtained is shown in Figure 3.6

3.6 Pressure Transmitter

A differential pressure transducer made by KIMO, France (Plate 3.9) having specifications is of type CP304-HOP and with configurable Range in between -10,000Pa to +10,000Pa was used to capture the pressure within the flow field. When this instrument is subjected to pressure, internal electronic strain gages that constitutes the Whitestone Bridge produces imbalance. Resulting voltage in turn gives the measurement of pressure. An LCD display displays the results. Its minimum configurable range lies within 0Pa to ±1000Pa. It has interchangeable measuring range and permanent self-calibration. Temperature compensation for air velocity and airflow is facilitated through the inclusion of thermocouple input in the transmitter, along with pre-installed Two 4-20mA and 0-10V outputs, 4-wire technology, RS232 input/output for connection to a class 200/300 transmitter, and 2 RCR relays rated at 6A/230V.

3.7 Experimental Program

Several techniques can be used for experimental research in delta wings aerodynamics as pointed out by Gursul et al, [56]. The following techniques were adopted for the investigation in present study.

a) Force balance measurements like lift force, drag force and moment etc. that provide time-averaged integral quantities.

b) Steady and unsteady pressure measurements over suction side including pressure-sensitive paint. These provide wing surface measurements of flow.
c) Surface flow visualization, for example, oil flow visualization. That gives an indication of surface flow streamlines and pattern, but again does not provide information on off-surface flow.
d) Multi-hole velocity-probe technique that measures three components of mean velocity.

The experiments were carried out in following stages i.e. oil flow visualization, force measurement, measurement of velocity profile and surface pressure distribution. The entire experiment was designed to carry out at a free stream velocity of 12m/s. within the test section. The velocity in test section was measured using pitot tube after the flow reached a steady state condition. Mass flow rate and subsequent flow velocity within test section was monitored by maintaining the pressure drop across the contraction cone during entire experiment. Certain experimental parameters are tabulated in Table 3.2.

3.7.1 Oil Flow Visualization

The technique of visualising flow over a stationary surface by implementing slightly additive oil mixture containing pigment became standard wind tunnel procedure over the years. Titanium di-oxide (TiO_2), kerosene and oleic acid ($C_{18}H_{34}O_2$) were utilized as pigment, solvent and additive of the oil mixture respectively for the present investigation. This oil mixture forms a whitish pattern over the surface of stationary wing model. Several trial and errors were carried out before getting the appropriate mix of oil and pigment for this specific test condition. The objective was to formulate a mixture of such a consistency that will run easily under the given free-stream flow leaving behind the flow pattern traced by the mixture.

To perform the experiment at each angle of attack, first, the leeward surface of the wing was meticulously cleaned to remove any dirt or remaining oil mixture from previous experiments. Following that oil mixture was gently applied with a brush over the wing model surface. After that, the wing was mounted to the traversing mechanism. Finally, after keeping the model under desired pitch angle, flow was allowed to pass over it for certain amount of time. A flow pattern was observed to be formed over leeward surface. Picture of that pattern was captured and recorded using digital camera. For better

understanding of the pictorial views, the photos were inverted in picture editable software and hence produced in this thesis.

3.7.2 Surface Pressure Distribution Measurement

To conduct surface pressure measurement, it was necessary to create pressure taps across the wing surface. Understandably, once the tap or hole on the wing's surface is done, one cannot use the wing for other experimental work. So, after all scheduled experiments were over, present study were conceived.

3.7.2.1Design of Pressure Taps

The placement of pressure taps was a matter of significance, and it has been suggested that the pressure taps should be positioned to cover the entire half span of the wing model due to symmetry conditions. Additionally, careful consideration was given to ensure that the effect caused by one pressure tap would minimally interfere with flow over other pressure taps. Informed by existing literature, it was determined that surface pressure stations would be distributed as depicted in Figure 3.7.

The span of the leeward side of the wing was divided into a specific number of sections, and pressure taps were distributed along these sections from the leading edge to the trailing edge. There was a total of five surface pressure measurement sections at x/c = 0.92 (a-section), 0.75 (b-section), 0.65 (c-section), 0.55 (d-section), and 0.35 (e-section) positioned on the wing surface in the streamwise direction, where x is the distance from the leading edge and c represents root chord length (0.189m). One of these sections was located in the strake portion while four remained in the wing portion.

As the span of the wing is not uniform, each section, i.e. a to e were carefully considered for selection of number of stations. As section e is in the strake portion and the span is narrow there, two number of stations were considered for measurement. The symmetry line provides the third one (e0). These two points (e1 and e2) were connected with the tip of the wing by a straight line and extended towards the tail. This imaginary line crosses over the section d,c,b, and a. the corresponding intersections were considered as the 1^{st} and 2^{nd} station of respective sections, while the symmetry line provide zeroth to all. Now other stations were marked considering equal distance from each other and space available. Following the aforesaid procedure, a total of twenty-eight stations were marked for pressure measurement.

1.3mm diameter pressure holes were created on the wing model using a precision pen drill to ensure accuracy. PVC tubes were then threaded through these holes and carefully guided through the interior hollow of the airfoil, exiting on the windward side of the model. The protruding ends of the PVC tubes were trimmed flush with the wing surface, and connected to a pressure transmitter as detailed in section 3.7.2.2. A bubble test was conducted for each hole to check for blockage before arranging, identifying, and labelling each tube according to predetermined nomenclature from the design phase. Attention was given to maintaining an orderly arrangement without any loose ends that could disrupt airflow within the test section.

Great care was taken to ensure the correct connection of the PVC tube with the pressure transmitter. To minimize pressure drop during measurement, one PVC tube from a specific pressure tap was connected to the pressure transmitter port while the other PVC tubes from remaining taps were temporarily sealed. This temporary sealing aimed to prevent any disturbance in the boundary layer over the thermoplastic wing model caused by air suction through these PVC tubes and their corresponding pressure taps. The setup and preparations for overall surface pressure measurements are illustrated in Plate 3.10.

3.7.2.2Measurement, Logging and Calculation of Pressure Data

A Kimo pressure transmitter was employed to gauge the pressure of all the pressure taps. After allowing for the stabilization of flow velocity within the test section, differential pressure was assessed by linking one end of a PV8C tube extending from the pressure taps to one of the ports on the pressure transmitter, while leaving another port open to atmospheric conditions. Data were acquired for each individual pressure tap across a thermoplastic wing surface at various angles of attack between 0° and 30°.

The coefficient of pressure (C_p), The non-dimensional form of pressure was calculated using the following equation,

$$C_p = \frac{p - p_\infty}{\frac{1}{2}\rho_\infty {u_\infty}^2} \qquad \text{..... 3.11}$$

3.7.3 Aerodynamic Force Measurement

In order to perform force measurement, three-component balance was fixed with composite wing model with proper fixing. The other end of the balance is fitted using two screws to sting connected to the sector of wing model traversing mechanism.

Post mounting the wind model with traversing system, and after connecting this combination with the PC interface, input from PC is given for particular pitch angles. To have an accurate measurement inclinometer was employed. The coordinate system of the wing model is illustrated in Figure 3.8. After reaching steady flow condition inside test section, balance readings were taken by the data accusation system in a computer run by Intel Pentium Processor. Reading was taken by varying angle of attack between 0° to 30°. At every angle of attack data were collected after the flow gets stabe and for 2 minutes with 1 second interval. For every angle of attack 121 numbers of readings were collected. Axial load O_a, normal load measured at station 1 O_{n1} and normal load measured at station 2 O_{n2} was saved for each and every data set. These axial, normal load values were averaged and multiplied by gravitation force (g) to convert them in to force values F_A, F_{N1} and F_{N2} respectively. Further calculations were made using equations 3.1 through equation 3.3 from section 3.4.1. Forces obtained from the experiments were used to calculate force coefficients according to equations as discussed in previous chapter.

3.7.4 Velocity Measurement

A calibrated three-hole pressure probe was used to measure velocity profile over wing surface during the experiment. Non-null type calibration technique was accomplished for calibration of the three-hole pressure probe. Numerical algorithm was written to calculate calibration coefficients. These calculated calibration coefficients were used to estimate the unknown flow components over the surface of wing by employing another set of algorithms.

3.7.4.1 Preparation of Measuring Stations and Velocity Traversing Mechanism

It was very important to set the locations where the velocity profile will be measured. For measurement of velocity, similar arguments were considered as for surface pressure measurement and it was decided to measure velocity profile on similar configurations. Total five numbers of chord-wise velocity measurement sections namely A, B, C, D and E were marked on the wing surface. At every chord-wise section were divided into suitable number of span-wise stations. Those stations were marked through 1 to 28 as a total of twenty-eight velocity measurement locations were finalised for experiment.

Velocity profiles were measured at 0° and 10° angles of attack. To facilitate the experiment, Three-hole pressure probe traversing mechanism was placed over the test section. Suitable arrangements were made for traversing of the probe. Appropriate slots were cut on the top of test section, just over the model wing to move the probe towards and away from the wing at aforementioned twenty-eight locations. It was also guaranteed that whenever a slot is being used for measurement of velocity, other slots remain covered and not allowed any additional flow within test section.

3.7.4.2 Measurement, Logging and Calculation of Three-Hole Pressure Probe Data

During experiment, a KIMO make pressure transmitter was used, which measured pressure related to atmospheric in each of three hole of the pressure probe. To start with the experiment, first the probe is moved to a desired location by moving the traversing carefully. When the probe reach at exact location, wind tunnel was switched on and a sufficient time was allowed to the flow to settle. After that measurements, observed from pressure transmitter, were noted in data sheet. Numerical code were applied to calculate free stream velocity, velocity components and flow angles with the help of calibration coefficients

3.8 Error and Uncertainty Analysis

In measuring physical quantities, it is commonly acknowledged and accepted that certain amount of error will present, but upto a certain limit. If an experiment is repeated time and again, it may produce different values each time. The inaccuracy of the experiment is generally expressed as ‘uncertainty’ and its value should be provided by an ‘uncertainty analysis’ An error in measurement means the difference between the true value and the measured or recorded value, whereas uncertainty expresses the possibility of the error present. A researcher must be careful enough to reduce error and record or achieve measured value close to true value. It is indeed required to find out the sources of such errors and to minimize as much as possible.

3.8.1 Sources of Errors

The errors in the present experiment can be generated from several methods. few of them are discussed below,

1. Fabrication of a particular wing model as used in present investigation could have caused error. The double delta wing configuration
2. The wing model was designed and fabricated in-house. To keep the wing surface smooth and also to keep the wing model according to the design specification, utmost care was taken during fabrication. Presence of any unevenness on the wing surface results into drastic change in flow structure and performance of the wing model.
3. Error induced from measurements of several different parameter were tried to be avoided by careful and repeated inspection.
4. For aerodynamic parameter measurement error could have caused from simply wrong alignment of strain gage balance with wing model. To avoid error, care was taken during fabrication process of wing also during fixing of the strain gage balance. The strain gage balance is made using alloy steel 17-4PH, having ultimate strength of 120kg/mm2. But under experimental condition presence of any slight deformity in strain gage balance could have caused wrong output. Calibration data indicate a deviation of 0.5% with respect to full scale.

   The uncertainty of strain gage balance was calculated by implementing method of Kline and McClintock [57]. For uncertainty analysis of measured quantity r, U_r variable is taken as uncertainty of measured quantity. Relative uncertainties of measured aerodynamic parameters are expressed in below expression [58].

$$\frac{U_{C_L}}{C_L} = \sqrt{\left(\frac{U_l}{l}\right)^2 + \left(\frac{U_{q_\infty}}{q_\infty}\right)^2 + \left(\frac{U_S}{S}\right)^2} \quad \ldots\ldots\ldots\ldots\ldots 3.12$$

$$\frac{U_{C_D}}{C_L} = \sqrt{\left(\frac{U_d}{l}\right)^2 + \left(\frac{U_{q_\infty}}{q_\infty}\right)^2 + \left(\frac{U_S}{S}\right)^2} \quad \ldots\ldots\ldots\ldots\ldots 3.13$$

$$\frac{U_{C_M}}{C_M} = \sqrt{\left(\frac{U_{M_c}}{M_c}\right)^2 + \left(\frac{U_{q_\infty}}{q_\infty}\right)^2 + \left(\frac{U_S}{S}\right)^2 + \left(\frac{U_{C_{MAC}}}{C_{MAC}}\right)^2} \quad \ldots\ldots\ldots\ldots 3.14$$

   Where U_{C_L}, U_{C_D}, U_{C_M} indicate the uncertainties of measured parameter lift, drag and moment respectively. U_{q_∞}, U_S, $U_{C_{MAC}}$ represent uncertainty in measurement of dynamic pressure, planform area, and mean aerodynamic chord. Lift, drag, and moment uncertainties particularly

are function of uncertainties present in normal force U_{C_N}, axial force U_{C_A}, moment about chord U_{M_C}, angle of attack U_α [59].

5. For surface pressure measurement, electronic pressure transmitter was used. Any fluctuation in input power could have caused the instabilities in reading. To eliminate any such chance of error, the calibration setting of pressure transmitter was checked and also reproducibility of any measurement obtained from the instrument was ensured.
6. Error could have caused from model traversing mechanism. As discussed in section 3.3.1 wing model traversing mechanism has a pitch angle accuracy of ±0.1. The 0° angle of attack position of sector was confirmed to be coincident with wind tunnel central axis. Additionally, any orientation of angle of attack of sector was also checked using spirit bubble to confirm its position.
7. One of the sources of error could have been caused due to design, fabrication, and alignment of the three-hole pressure probe traversing mechanism discussed in section 3.3.2. In order to minimize error in three-hole pressure probe traversing mechanism proper care was taken during fabrication and alignment. The traversing mechanism has alignment error in any linear direction within ±1mm. This was calculated on maximum backlash of the lead screw fitted in all three direction of the traversing mechanism. The protector used for three-hole pressure probe calibration had a least count of 1°. Error caused from fabrication of three-hole pressure probe was compensated implementing repeated calibration of the probe.

Method discussed and developed by Moffat [60] and Nakra and Chowdhury [61] are considered to estimate several errors and uncertainties. Error or uncertainties are measured on the repeated measurements taken at a particular point of interest and pre-determined identical conditions. The approximate uncertainties for some parameters are tabulated below in Table 3.3.

Table 3.1 Geometric parameters of Double Delta Wing

Span, b	0.194m
Wing Root Chord	0.189m
Aspect Ratio	2.36
Strake Angle	75°
Wing Angle	45°
Wing Thickness	10mm
End Bevel	20°

Table 3.2 Experimental Parameters

Free Stream Velocity, u_∞	12m/s
Ambient Pressure	102.3Pa
Ambient Temperature	26°C
Density, ρ	$1.181 kg/m^3$
Dynamic Viscosity, μ	$1.8536 \times 10\text{-}^5$
Chord Reynolds Number, Re_{MAC}	1.46×10^5

Table 3.3 Approximate Uncertainties

Quantity	Uncertainity	
	$u_\infty < 10m/s$	$u_\infty > 10m/s$
Mean Velocity	± 5%	± 1%
Pressure (Total and Static)	± 2%	± 0.2%
Dynamic Pressure	± 2%	± 0.2%
Angle of Attack	± 0.5%	± 0.5%

Plate 3.1 Photograph of wind tunnel

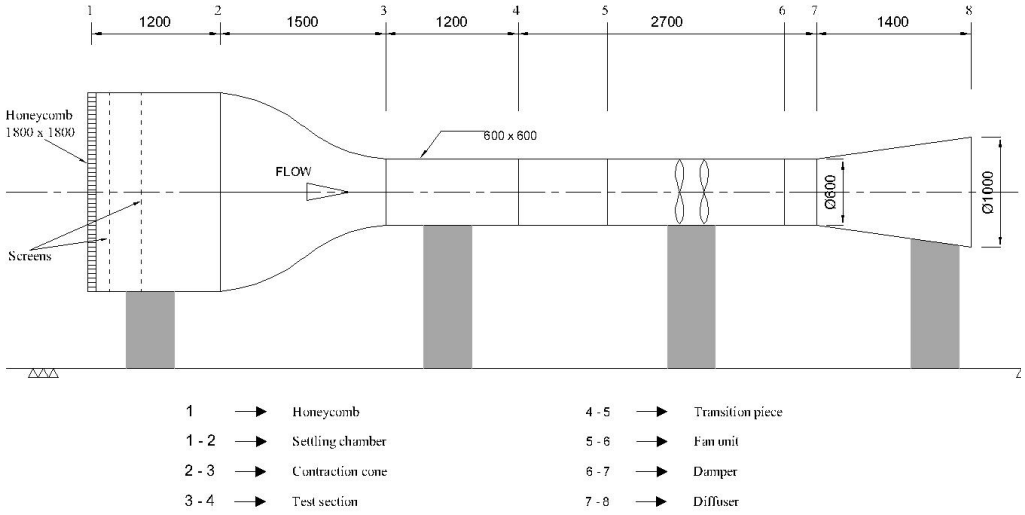

Figure 3.1 Schematic of wind tunnel

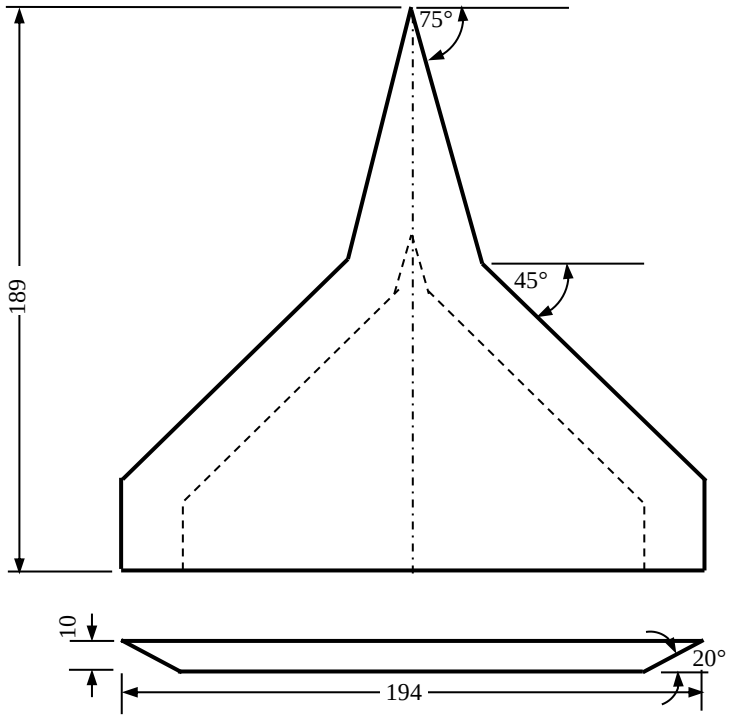

Figure 3.2 Schematic of double delta wing model

Plate 3.2 Photograph of wing traversing mechanism

Plate 3.3 Photograph of probe traversing mechanism

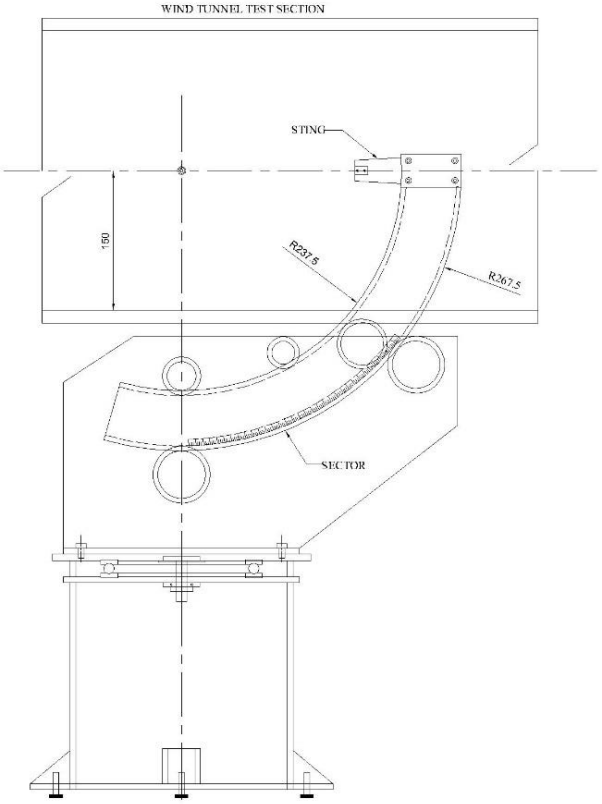

Figure 3.3 Schematic of model positioning system

Plate 3.4 Photograph of 3-component strain gage balance

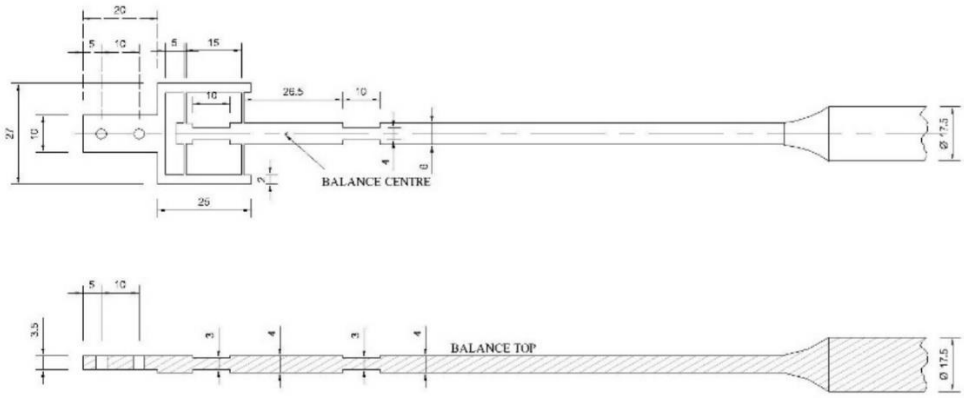

Figure 3.4 Schematic of 3-component strain gage balance

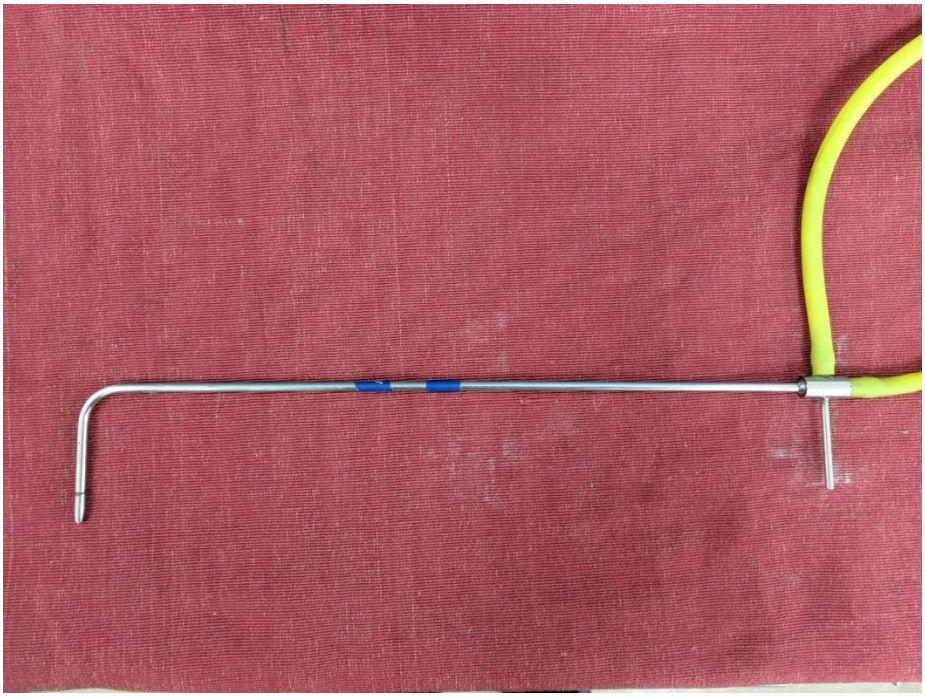

Plate 3.5 Photograph of pitot tube

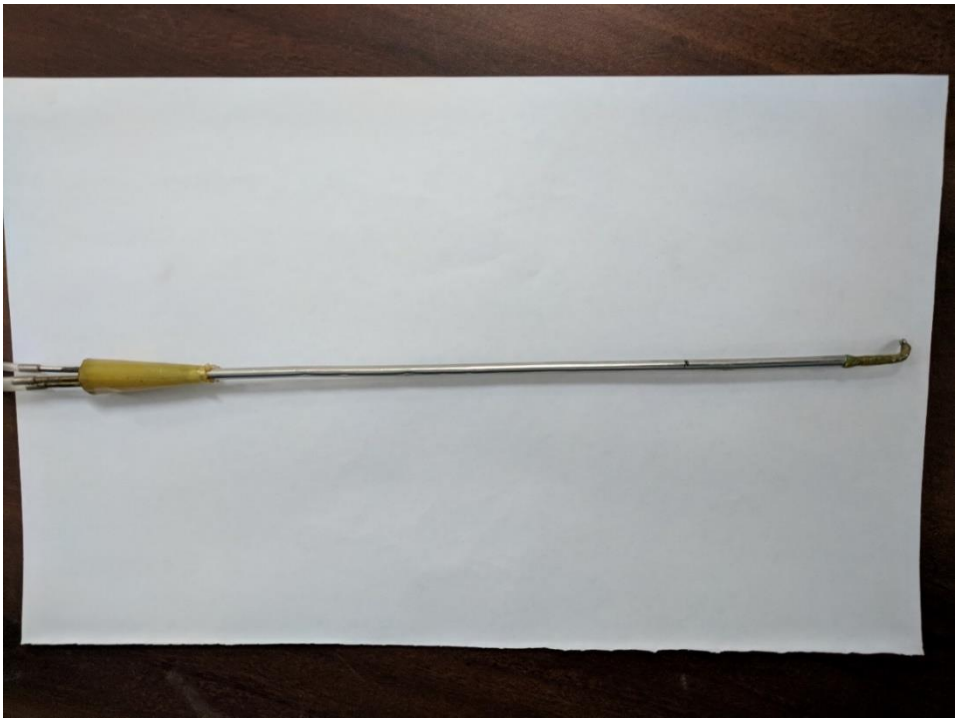

Plate 3.6 Photograph of 3-+hole pressure probe

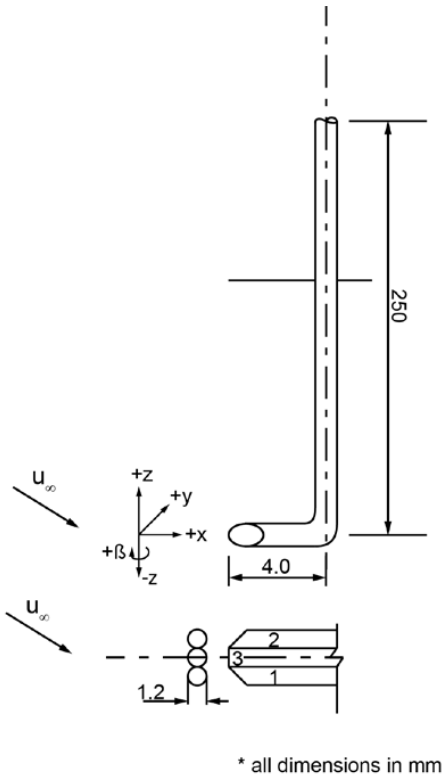

Figure 3.5 Schematic of 3-hole pressure probe

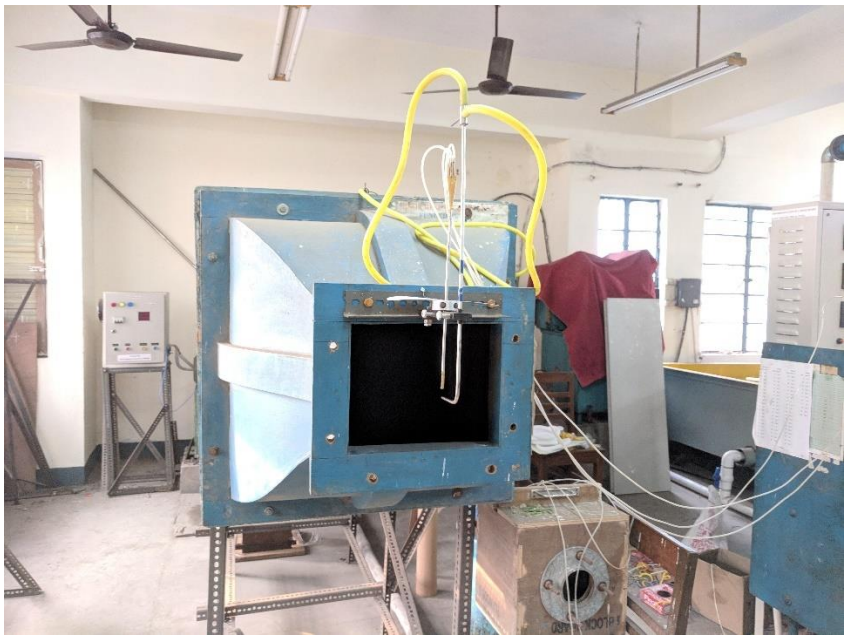

Plate 3.7 Photograph of blow down wind tunnel while calibrating 3-hole probe

Plate 3.8 Photograph of array of U-tube manometer during 3-hole probe calibration

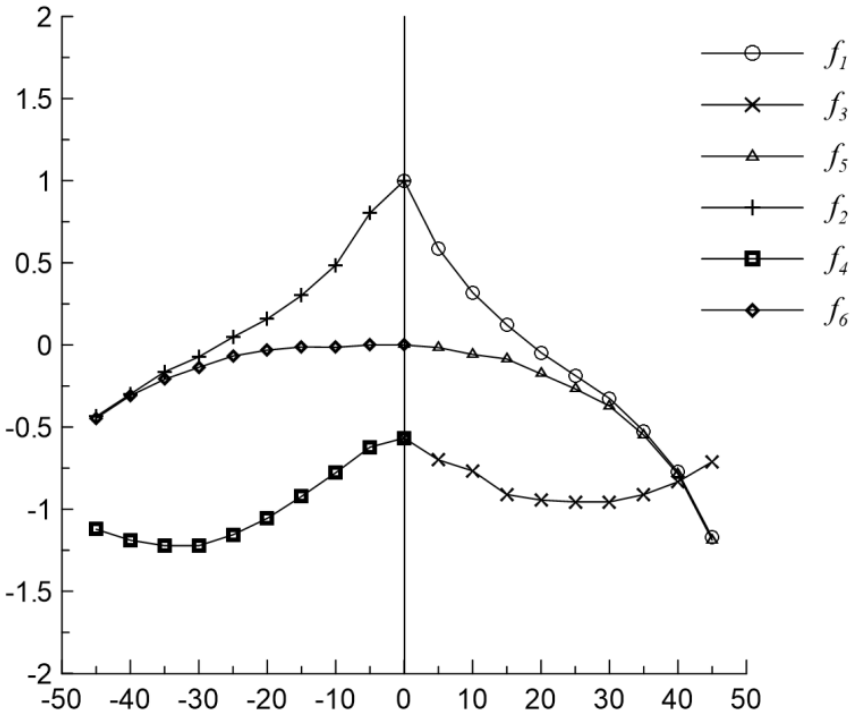

Figure 3.6 3-hole pressure probe calibration curve

Plate 3.9 Photograph of differential pressure transducer

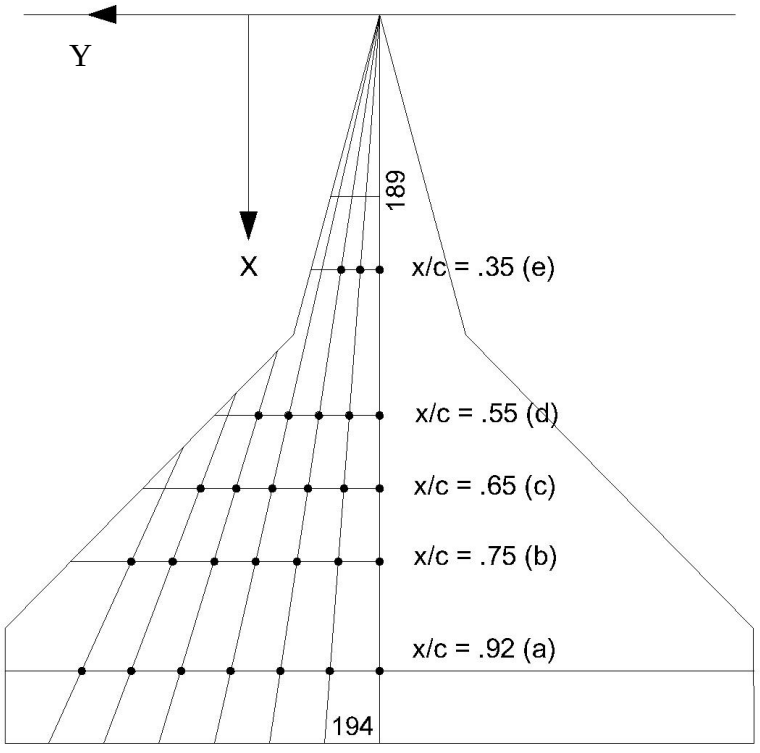

Figure 3.7 Location of pressure points of Model Wing

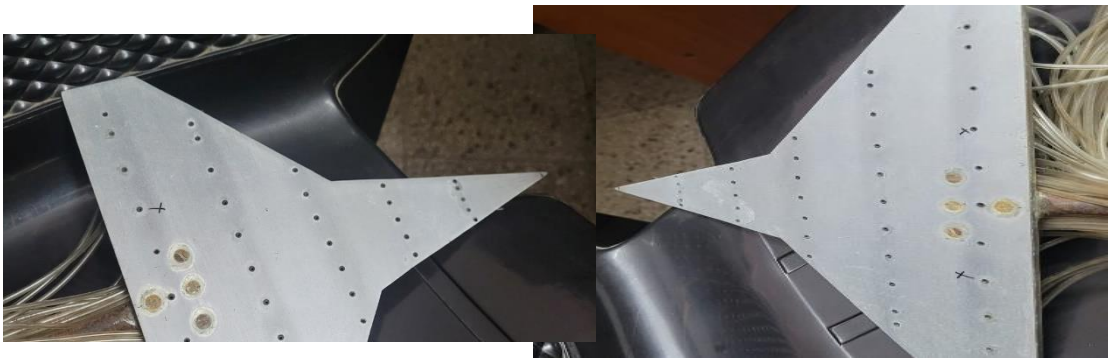

Plate 3.10 Surface pressure measurement station of wing

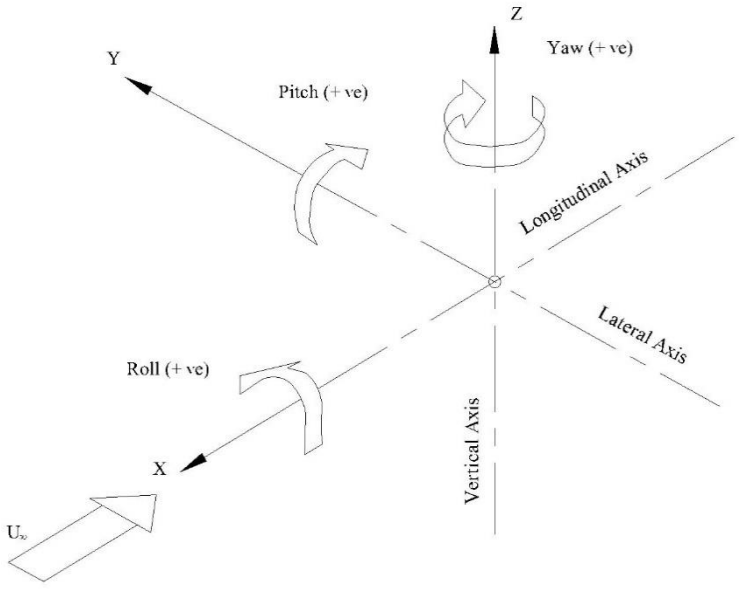

Figure 3.8 Model coordinate system

CHAPTER 4

Numerical Technique and Procedure

4.1 Introduction

In twentieth century advent of digital computers, respectful strides have been made in the field of computational fluid dynamics. Computational dynamics have been applied for modern practices in almost all engineering branches. New methodologies and schemes have been developed for Computation Fluid Dynamics (CFD) in order to resolve complex issues by predicting behavior of fluid. CFD harmonically complements experimental as well as theoretical fluid dynamics. Regardless of all these improvements complete solution to Navier-Stokes equations are still out of grasp. To make computational method, various simplification and assumptions are still needed. To obtain usable results from numerical methods often requires decision making of proper turbulence model, solving techniques and available computational resources, etc.

The purpose of this study was to carry out three-dimensional simulation of the 75º/45º double delta wing to find out the flow field structure around the wing model. CFD analyses were performed for comparative analysis of computational results in contrast to experimental results. Here in the present study, commercially available Ansys Fluent (version 19.1) was utilized to acquire aerodynamic characteristics and other flow pattern around double delta wing model. Simulations have been made using Intel(R) Core (TM) 2 Duo CPU in conjunction with RAM of 3GB. Numerical simulation consists of stages:

1. **Pre-Preprocessing (Modelling)**: This stage includes three-dimensional accurate modeling of the wing as well as of the flow problem and meshing of the domain.
2. **Processing (Computation)**: This stage includes application of selected turbulence model as well as solver settings and to converge for the solution.
3. **Post-processing**: This stage deals with analysis of results and represent with suitable plotting, visualization, etc.

The following sections briefly discuss the procedures taken in preparing the physical model, selecting appropriate meshing and mathematical model formation for turbulence analysis of the wing model.

4.2 Pre-Processing (Modelling)

Dimensionally accurate three-dimensional model of 75°/45° double delta wing model as shown in Figure 4.1 was created in SolidWorks. Flow domain having exact same dimension of suction type wind tunnel test section (as described in Chapter 3) in which the experiments were conducted, was created [Figure 4.2]. Wing model was imported to Ansys Design Modeler for processing. Then processed flow domain was transferred to Ansys ICEM CFD meshing.

Unstructured hybrid mesh grids were generated which are combinations of tetrahedron, wedge and pyramids using Ansys auto meshing (ANSYS ICEM CFD). Unstructured mesh conforms to complex geometrical model easily compared to structured mesh. Sectional view of the full mesh is shown in the Figure 4.3. A grid sensitivity or independence study was conducted for the chosen Spalart-Allmarasb (SA) turbulence model. Three different grid sizes with 16520, 175621 and 234880 number of cells were considered for this study. Drag coefficients and lift coefficient have been compared for AoA = 30° with experimentally obtained results, which is given in Table 4.1. Any more enhancements in grid sizes beyond *Mesh 3* configuration comes with a rise in computation time and subsequently cost significantly. Total 60975 numbers of nodes and 234880 numbers of elements are created in mesh. An inflation layer grown outward from the wing model was also provided for better production of boundary layer. It has been found in Ansys Manual [62] that for SA model y^+ one should use a very fine wall mess (on the order of $y^+ \approx 1$ for the first near-wall cell centre) for proper boundary layer resolution and simulation success. Near wall mesh sizes (average y^+ values of 1.7937) are arranged appropriately to resolve the boundary velocity profile. The mesh statistics are given in the Table 4.2. Ansys manual indicate that mesh quality criteria of Ansys mesh quality improves significantly as orthogonal quality of mesh moves towards 1. Also for good quality of mesh, skewness of the generated mesh should have value which is close to 0 [62]. For the present computation, mesh orthogonal quality found to be 0.91 and the average skewness of the mesh has been fixed at 0.29.

4.3 Processing (Computation)

The numerical solver used in the study is Ansys's Fluent solver. Fluent was chosen because it has a proven reliability in recording simulation of turbulent flows. Fluent provides an exhaustive list of modeling capacities for range of incompressible and compressible as well as turbulent or laminar flow. A wide range of theoretical models for transport phenomena is combined within Fluent, that gives the ability to simulate complex geometries. Spalart-Allmaras (SA) turbulence model is used in conjunction of steady state solution are considered for present study within the flow domain over a double delta wing having sweep angle of 75/45°.

Several turbulence models were engaged to predict grid sensitivity and model sensitivity at similar inlet conditions to the meshed wing model. As it has already been selected the number of cells to be 234880, the same wing model was used for three different turbulence models namely Spalart-Allmaras (SA), k-epsilon (*k*-ε) and k-omega SST (*k*-ω SST). for prediction of results. Numerical results of aerodynamic characteristics e.g., Lift Coefficient (C_L) and Drag Cofficient (C_D) at 30º angle of attack were compared to that of experimental results at the same pitch angle. The results were tabulated and percentage variations from experimental results were calculated to compare the proximity with experiment. For the present investigation, it was observed that the results predicted by SA and *k*-ω SST are in close proximity with the experimental results. The results were tabulated in Table 4.3. It has also been found in paper by J. Yuvaprakash et al. [63] and Nath et al. [64] that under low subsonic flow conditions of aerodynamic objects or flying vehicles, the Spalart-Allmaras (SA) model with fluent software calculates much faster with low computation cost, compared to other turbulence models. Dawei Liu et al. [65] also discussed that for supercritical airfoils computation results obtained applying Spalart-Allmaras turbulence model gives better result in line with experimental results compared to *k*-ω SST turbulence model. It can be concluded that at low subsonic flow conditions aerodynamic flow properties can be predicted within equitable accuracy compared to experimental data using Spalart-Allmaras turbulence model. Following this study, all further numerical simulations were performed on mesh configuration, having 234880 numbers of cells utilizing Spalart-Allmaras (SA) turbulence model.

The Spalart-Allmaras [66] is an one-equation effective for low Reynold number model assembled using empiricism and arguments of dimensional analysis, Galilean invariance, and selective dependence on the molecular viscosity [62]. The model solves for the variable, $\tilde{v}$, which is similar to the eddy viscosity referred as the Spalart-Allmaras variable Model was developed and calibrated for a certain class of flows, which mainly includes external flow over airfoil and wings (aerospace applications). The model has become one of the most widely used one equation models by researchers and industry because of its ability to predict flow feature without being burden on computational resources. Governing equation for SA model is written below,

4.3.1Governing Equation

Conservation equation of mass, momentum and energy are solved for obtaining solution over the double delta wing.

Conservation of mass is represented as

$$\frac{\partial \rho}{\partial t} + \left(\frac{\partial \rho u}{\partial x} + \frac{\partial \rho v}{\partial y} + \frac{\partial \rho w}{\partial z}\right) = 0 \qquad \ldots\ldots\ldots\ldots\ldots\ldots 4.1$$

From conservation of momentum we get,

$$\left.\begin{aligned} \rho \frac{Du}{Dt} &= -\frac{\partial p}{\partial x} + \frac{\partial \tau_{xx}}{\partial x} + \frac{\partial \tau_{yx}}{\partial y} + \frac{\partial \tau_{zx}}{\partial z} + \rho f_x \\ \rho \frac{Dv}{Dt} &= -\frac{\partial p}{\partial y} + \frac{\partial \tau_{xy}}{\partial x} + \frac{\partial \tau_{yy}}{\partial y} + \frac{\partial \tau_{zy}}{\partial z} + \rho f_y \\ \rho \frac{Dw}{Dt} &= -\frac{\partial p}{\partial z} + \frac{\partial \tau_{xz}}{\partial x} + \frac{\partial \tau_{yz}}{\partial y} + \frac{\partial \tau_{zz}}{\partial z} + \rho f_z \end{aligned}\right\} \qquad \ldots\ldots\ldots\ldots\ldots\ldots 4.2$$

And lastly conservation of energy equation give us,

$$\begin{aligned} \rho \frac{D}{Dt}\left(e + \frac{V^2}{2}\right) = \rho q &+ \frac{\partial}{\partial x}\left(k \frac{\partial T}{\partial x}\right) + \frac{\partial}{\partial y}\left(k \frac{\partial T}{\partial y}\right) + \frac{\partial}{\partial z}\left(k \frac{\partial T}{\partial z}\right) \\ &- \frac{\partial (up)}{\partial x} - \frac{\partial (vp)}{\partial y} - \frac{\partial (wp)}{\partial z} + \frac{\partial (u\tau_{xx})}{\partial x} + \frac{\partial (u\tau_{yx})}{\partial y} + \frac{\partial (u\tau_{zx})}{\partial z} \\ &+ \frac{\partial (v\tau_{xy})}{\partial x} + \frac{\partial (v\tau_{yy})}{\partial y} + \frac{\partial (v\tau_{zy})}{\partial z} + \frac{\partial (w\tau_{xz})}{\partial x} + \frac{\partial (w\tau_{yz})}{\partial y} + \frac{\partial (w\tau_{zz})}{\partial z} + \rho f \cdot V \end{aligned}$$

$$\ldots\ldots\ldots\ldots\ldots\ldots 4.3$$

Transport equation for Spalart-Allmaras is expressed as,

$$\frac{\partial}{\partial t}(\rho\tilde{v}) + \frac{\partial}{\partial x_i}(\rho\tilde{v}u_i) = G_v + \frac{1}{\sigma_{\tilde{v}}}\left[\frac{\partial}{\partial x_j}\left\{(\mu + \rho\tilde{v})\frac{\partial\tilde{v}}{\partial x_j}\right\} + C_{b2}\rho\left(\frac{\partial\tilde{v}}{\partial x_j}\right)^2\right] - Y_v + S_{\tilde{v}}$$

…… 4.4

where $\tilde{v}$ is the transport variable which is analogous to the turbulent kinematic viscosity except viscous dominated near wall region. G_v in the equation represents production of turbulent viscosity, Y_v represents the destruction of turbulent viscosity that mainly occur near wall region because of viscous damping and wall blocking, $\sigma_{\tilde{v}}$ and C_{b2} are constants and v represents molecular kinematic viscosity, $S_{\tilde{v}}$ is user-defined source term.

Turbulent viscosity (μ_t) is calculated using

$$\mu_t = \rho\tilde{v}f_{v1} \quad \text{…… 4.5}$$

where f_{v1} is viscous damping function and expressed as

$$f_{v1} = \frac{\chi^3}{\chi^3 + C_{v1}^3} \quad \text{…… 4.6}$$

In above equation $\chi \equiv \frac{\tilde{v}}{v}$

Turbulent viscosity production term G_v expressed as,

$$G_v = C_{b1}\rho\tilde{S}\tilde{v} \quad \text{…… 4.7}$$

where, $\tilde{S} \equiv S + \frac{\tilde{v}}{\kappa^2 d^2} f_{v2}$ …… 4.8

and, $f_{v2} = 1 - \frac{\chi}{1+\chi f_{v1}}$ …… 4.9

In equation (4.7 and 4.8) C_{b1} and κ are constants, d is the distance from wall, and S represents scalar measure of the deformation tensor.

The destruction of turbulent viscosity term is expressed as,

$$Y_v = C_{w1}\rho f_w \left(\frac{\tilde{v}}{d}\right)^2 \quad \text{…… 4.10}$$

where, $f_w = g\left[\frac{1+C_{w3}^6}{g^6+C_{w3}^6}\right]^{\frac{1}{6}}$

$$g = r + C_{w2}(r^6 - r)$$

and $r \equiv \frac{\tilde{v}}{\tilde{S}\kappa^2 d^2}$

For the above equations, C_{w1}, C_{w2}, C_{w3} are the constants. Modifications are also done in to include the effect of mean strain on S will also affect the value of $\tilde{S}$ which is required to compute r.

Model constants have following default values in fluent,

$$C_{b1} = 0.1355, C_{b2} = 0.622, \sigma_{\tilde{v}} = \frac{2}{3}, C_{v1} = 7.1,$$

$$C_{w1} = \frac{C_{b1}}{\kappa^2} + \frac{(1 + C_{b2})}{\sigma_{\tilde{v}}}, C_{w2} = 0.3, C_{w3} = 2, \kappa = 0.4187$$

At walls, the modified turbulent kinematic viscosity, $\tilde{v}$ is modeled to be zero.

Spalart-Allmaras is low Reynolds number model. It involves proper solution of boundary layer having viscous-effect region [62]. Also, where mesh resolution is not sufficiently fine, Spalart-Allmaras model can be applied for predicting wall functions. So Spalart-Allmaras model works remarkably well with comparatively coarse mesh. The near-wall gradients of the transported variable in the model are much smaller than the gradients of the transported variables in the compared to other turbulent models, which makes the model less sensitive to numerical error when non-layered meshes are used near walls.

Properties like density and viscosity were assumed as constant for the prevailing flow without any significant change in temperature, which is shown in the Table 4.4. Pressure-Velocity coupling method is used to solve these models and second order upwind spatial discretization scheme is applied for momentum. Solution was initialized uniformly throughout the domain using free stream inlet condition. Velocity inlet with free stream velocity magnitude of 12 m/s is used as inlet boundary condition. No-slip wall conditions are applied to the model surfaces without specifying any wall roughness. To simulate, angle of attack of stream velocity directions were adjusted in accordance to required angle of attack. A convergence criterion of 10^{-5} was selected for the residuals of flow parameters.

4.4 Post-Processing

Post-Processing software was used to process computational calculation results in useful data format. Post-Processors enable conversion of calculated numerical data into comprehensible and visual representation methods. This visualization of data helps to form additional inference about nature of analysis. Numerical data extracted from post-processor are analyzed with experimental data in chapter 6.

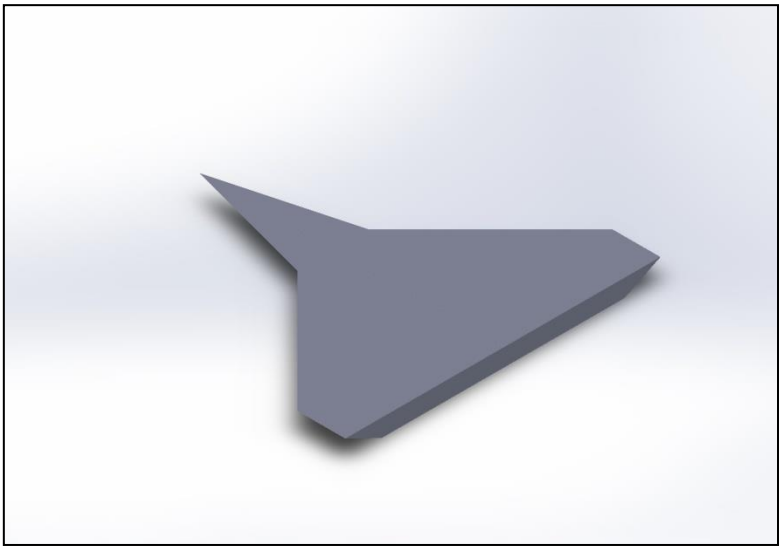

Figure 4.1 The-dimensional model of double delta wing.

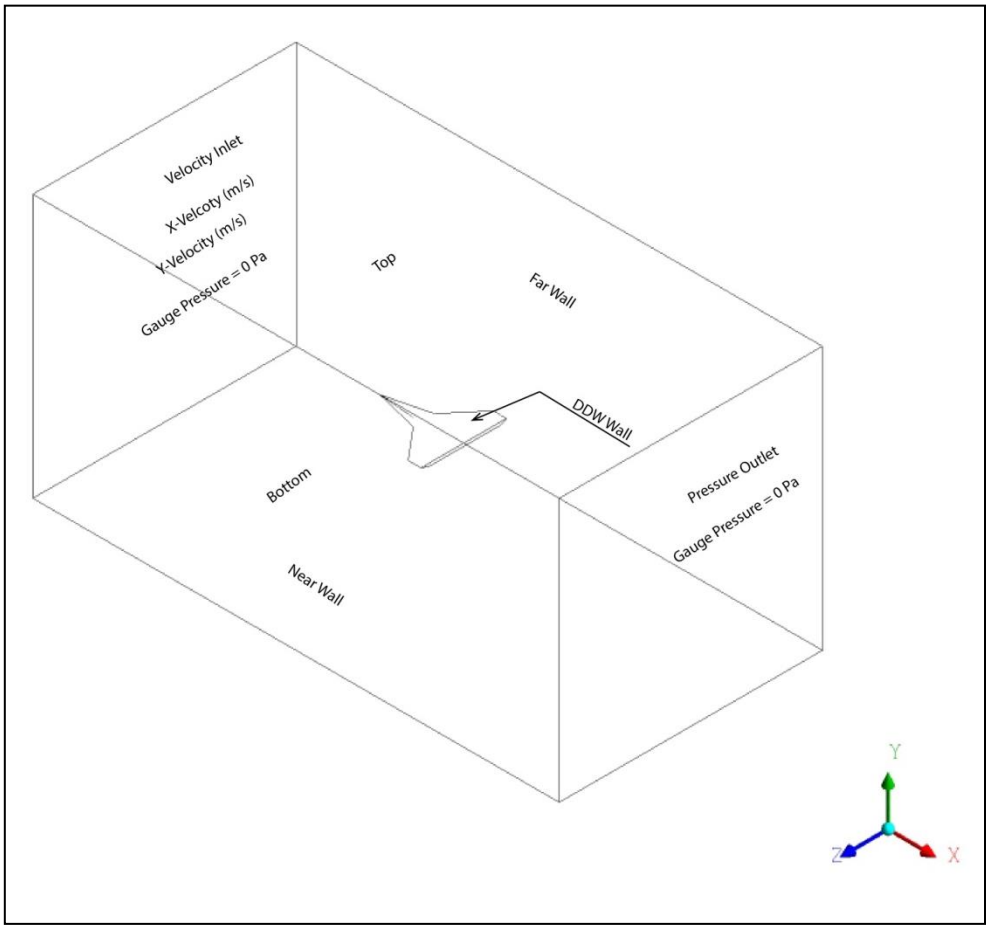

Figure 4.2 Computational domain of double delta wing.

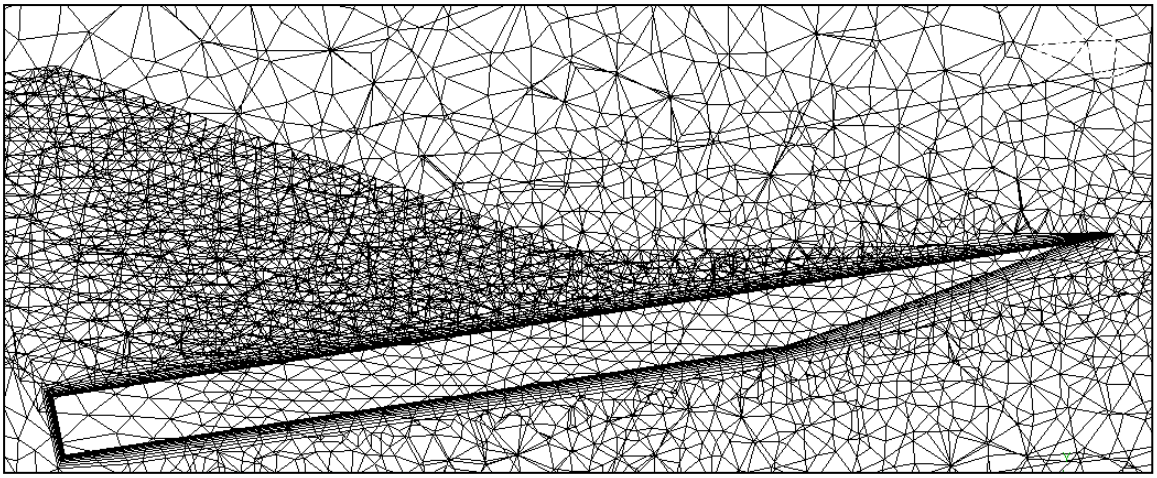

Figure 4.3 Cross-sectional view of the grid structure over wing.

Table 4.1 Comparison of results between different mesh configurations.

AoA = 30°	**Number of cells**	**C_D**	**C_L**	**Percent Difference C_D**	**Percent Difference C_L**
Experimental Data		0.63	0.95		
Mesh 1	16520	0.57	0.81	9.52	14.74
Mesh 2	175621	0.59	0.86	6.35	9.47
Mesh 3	234880	0.60	0.98	4.76	3.16

Table 4.2 Mesh Statistics.

Mesh Metric	**Minimum**	**Maximum**	**Average**
Orthogonal Quality	1.54×10^{-2}	0.99	0.91
Skewness	7.25×10^{-4}	0.98	0.29

Table 4.3 Comparison of results between different turbulence models.

AoA = 30°	**Number of cells**	**C_D**	**C_L**	**Percent Difference C_D**	**Percent Difference C_L**
Experimental Data		0.63	0.95		
Spalart-Allmaras (SA)	234880	0.58	0.90	7.94	5.26
K-Epsilon (k−ε)	234880	0.53	0.86	15.87	9.47
K-Omega (k−ω) SST	234880	0.56	0.87	11.11	8.42

Table 4.4 Parameters for numerical calculation.

Property	**Property value**
Gas	Air, Ideal Gas
Density, ρ (kg/m^3)	1.177
Dynamic Viscosity, μ (kg/m-s)	1.8536×10^{-05}
Velocity, v (Mach)	0.04
Velocity, v (m/s)	12
Temperature, T (K)	300

CHAPTER 5

Results and Discussions

Flow development over a double delta wing depends largely on the wing configuration. The present wing was exposed under different conditions of regulated flow to achieve the results as conceptualised. In the following sections, experimental results and discussions over 75º/45º are presented. Surface flow visualization, surface pressure distribution, force measurement and velocity distribution over leeward surface (top surface) of the wing were estimated. The entire set of experiments were carried out at a free-stream velocity (u_∞) of 12.0m/s and at mean aerodynamic chord-based Reynolds number Re_{MAC} of 1.46×10^5 at different angles of attack (AoA). An in-house fabricated and calibrated three-hole pressure probe was used for measurement of velocity distribution over the surface.

5.1 Flow Visualization

In order to visualize and grasp the flow structure over double delta wing profile flow visualization study was performed. Surface flow visualization method can predict the flow pattern formed over the wing surface in resemblance to actual flow behavior. Surface flow visualization is proved to be the most reliable method of experiment to understand the flow physics.

Figure 5.1(a) indicates the flow visualization result at 0° AoA. From Figure 5.1(a) it can be observed that flow patterns mostly move from leading edge to the trailing edge in mostly linear in fashion for both strake and wing portion. Absence of any possible cause of formation of vortices, separation or attachment pattern over the wing surface, makes the flow almost attached flow over entire portion of wing.

At 5° AoA possible formation of vortex impression can be observed from flow pattern in Figure 5.1(b). The separation and attachment line patterns in strake portion of wing show possible formation of strake vortex. The secondary attachment and separation structure impression starting from end of strake portion and near outboard portion of wing indicate towards formation of wing vortex as well.

For 10° AoA Figure 5.1(c) shows that with increase in AoA pattern formed for both strake and wing vortex become prominent because of increase in strength of the

vortices. Along with separation and attachment structure in strake and wing portion, distorted flow pattern can be observed near wing tip region. Also at this AoA slight inboard movement of strake and wing vortex can be seen, may be due to increased strength of vortices with increasing AoA.

Figure 5.1(d) and Figure 5.1(e) show the formation of flow pattern observed at 15° and 20° AoA respectively. Here the distinction between separation and attachment patterns formed near junction of strake and wing, may be as a result of merging of strake and wing vortex near the region The formation of flow pattern indicate compared to previous observations slight outboard movement of strake vortex and inboard shifting of wing vortex in these increased AoA.

Figure 5.1(f) and Figure 5.1(g) indicate the flow pattern formation at 25° and 30° AoA respectively. At these higher AoA the strake and wing vortices becomes more indistinguishable, which can be seen from the flow pattern. Both strake and wing vortices get more intertwined with each other to create a vortex core, which then rolls over the entire surface. Region of reattachment pattern observed to get reduced with high AoA. It can also be observed that at these higher AoA vortices appear to dissipate close to trailing portion of wing, which can be seen as less prominent reattachment line close to trailing edge of wing. Additionally with increase in AoA this dissipation of vortices appears to move slightly towards leading edge of wing points towards vortex breakdown over the wing surface occurs over the incrementally increasing area.

5.2 Force Analysis

Figure 5.2 illustrates the lift coefficient (C_L), drag Coefficient (C_D), moment coefficient (C_M), normal force coefficient (C_N), and axial force coefficient (C_A) which have been experimentally extracted with the help of three-component balance for varying AoA. In addition to that lift coefficient against drag coefficient is also plotted in order to grasp better understanding of the wing model aerodynamic performance.

Figure 5.2(a) illustrates the alteration of lift coefficient (C_L) with respect to AoA α. It can be seen from the Figure 5.2(a) that lift coefficient elevate almost linear fashion up to about 10° angles of attack. With further rise in AoA, rate of growth in curve appear to diminish slightly. This apparent loss of lift might be due to loss of strength in wing vortex and associated with appearance of strake-wing vortex merging as observed from surface flow visualization experiments. As the lift generation in case of delta wing is

linked with lift generation from vortices formed over the wing surface [67]. In case of double delta wing at these angles of attack the loss in strength of vortex generated lift might be compensated with the strake generated vortices by merging with wing vortices. It can be observed that from Figure 5.2, from 25° onwards the lift coefficient becomes essentially stagnant might be because of probable loss in strength of merged strake-wing vortex structure formed over the wing leeward surface.

Figure 5.2(b) represents alteration in drag Coefficient (C_D) with increasing AoA. Upon close inspection it can be seen that gradient of curve changes faintly at around 10° AoA in correspondence with lift coefficient curve. Following 10° AoA the rate of change in drag coefficient appear to rise more steeply with increase in AoA. This appearance of rapid rise in drag coefficient may be due to exposer of the wing body to the flow field with higher AoA. This also can be linked with appearance of merging phenomena of strake and wing vortices.

Figure 5.2(c) depicts the distribution of moment coefficient (C_M) against the growing angles of attack. The negative value of moment coefficient is due to counter-clockwise moment of the wing model. The change in slope of moment coefficient curve can be observed within 10° and 15° angles of attack. In between 10° and 15° angles of attack moment coefficient incrementally more negative in line with the loss in lift coefficient as observed previously. Post 15° moment coefficient portrays steady behavior without any significant change in slope of curve.

Figure 5.2(d) shows the change in normal force coefficients (C_N) with respect to AoA. As the normal force being the principle contributor in lift force, analogous to lift coefficient plot. It can be observed that normal force coefficient increases steadily up to about 10° AoA. Additionally like the nature of lift coefficient curve, the slope of the curve for normal force coefficient changes with increase in AoA post 10° AoA. This analogous behavior of normal force coefficient graph with variation of lift coefficient is the indication of effect of normal force in generation of lift.

Alteration in axial force coefficients (C_A) with respect to AoA is plotted in Figure 5.2(e). At par with observations from coefficients of drag it can be observed that post 10° AoA there is change in rate of rise in axial force coefficients. It can be seen that as the strake and wing vortex gets merged over the wing leeward surface it contributes to

rise in axial force, which in turn contribute towards drag forces. As axial force being the primary contributor in generation of drag force.

In order to comprehend the lift characteristics of the wing profile variation of drag coefficient (C_D) with respect to change in lift coefficient (C_L) is plotted Figure 5.2(f). The figure illustrates that lift coefficient rises in linear fashion with slight increase in drag coefficients upto about 10° AoA. The change in drag coefficient is quite trivial upto about lift coefficient of 0.6. However, afterwards drag coefficient is observed to be increase rapidly with very slight rise in lift coefficient.

Therefore, it can be assumed that merging of strake and wing vortices over wing leeward surface contributes to lift generation with rapid increase in drag.

5.3 Surface Pressure Distribution

Surface pressure is measured on the 75°/45° double delta wing model leeward surface at five different pre-determined chord wise locations for varying AoA between 0° to 30° with interval of 5°. Here the pressure distribution is plotted against z/s, where z is distance measured along span-wise direction of wing model and *s* is defined as span of wing model. Pressure distribution is measured utilizing pressure transmitter at pre-determined locations. Pressure distribution measuring locations are divided in to 5 different section along chord-wise direction named as a-section (x/c =0.92), b-section (x/c =0.75), c-section (x/c =0.65), d-section (x/c =0.55) and e-section (x/c =0.35). For these chord wise located sections x denoted the distance along chord wise direction starting from pointed tip portion of the strake part of the wing and c is length of the root chord. Also sections are arranged in such a mode that a-section is placed close to the trailing edge of the wing portion of double delta model and e-section is placed close to the tip of the model at strake portion. The a-section and b-sections are determined to have 7 measuring station each starting from 0 to 6. The c-section contains 6 measuring stations from c0 to c5. The d-section is designed to have 5 measuring station staring from d0 to d4 and finally the e-section contains 3 measuring station from e0 to e2. Surface pressure distributions are demonstrated along span-wise direction for different stations and different angles of attack.

In the Figure 5.3 surface pressure distributions are plotted for different sections and angles of attack for comparative analysis. In this figure different row portrays different AoA starting from top most row for 0° AoA and the bottom most rows for 30° AoA.

Whereas different columns represent different pre-determined sections over the double delta model leeward surface, starting a-section located in the left most columns and right most columns indicate e-section with all other sections are placed chronologically in between.

The first row of Figure 5.4, denoted as (a), represents pressure distribution at 0° AoA for different measuring sections. Here it can be seen that the pressure coefficient plots are mostly flat in nature and lies horizontally along the span wise axis. This phenomenon can be described due to probable attached flow with any indication of separation or vertical structure over the double delta model leeward surface. Pressure distributions indicate almost flat nature or attached flow structure for entire 5 different sections.

At 5° AoA, Figure 5.4 (b), suction pressure peak can be observed as a result of increment in pitch angle and also as an indication of onset of vortical/separated flow. Overall the curves are almost entirely insipid in nature with exclusive presence of rapid rise in pressure coefficient or suction pressure peak near the edge of the double delta wing model. Appearance of sudden rise in surface pressure distribution suggests the change in pressure coefficient due to onset of vortex structure. Characteristics of these vortex structures can also be anticipated from these pressure coefficient distribution plots. At 5° AoA the vortex made at strake part is almost indiscernible. It can also be seen that close to trailing edge of the double delta model or towards aft portion of the model pressure distribution attains less negative value or reaches lower peak value as flow loses strength in downstream portion, as observed from delta wing flow mechanics.

In pressure distribution at sections located in strake potion distinctive peak can be observed at 10° AoA from Figure 5.4 (c). So it can be assumed that formation of vortex structure in the strake portion of wing becomes more perceivable. Here the suction pressure peak continuously rises indicating growing contribution of strake and wing vortex structure to lift generation of double delta wing model. Upon close scrutiny it can be observed that reattachment location shifts slightly towards inboard portion of double delta model.

At 15° AoA the vortex formed in strake portion of double delta model becomes more pronounced [Figure 5.4 (d)]. This occurrence can be clarified effectively as the strength

of the strake vortices continues expanding. Upon close scrutiny the figure also indicates the assistance of strake vortices in vortices structures formed over the leeward surface of double delta model have grown significantly. Also, little peak like distribution towards y-axis before the actual peak in pressure distribution also points towards significant contribution of strake vortices in extra lift generation which is and additional benefit when contrasted with the delta wing. At this increased AoA the vortex structure seem to be displaced towards the inboard portion of double delta model or root chord, which can be seen in pressure distributions as the movement of reattachment location towards the inboard portion of the doubled delta model.

It can be seen that at 20° AoA, [Figure 5.4(e)] pressure distribution reaches apex at diminished value for downstream flow or sections located close to trailing edge of wing. Comparatively in strake portion of double delta model the peak in pressure distribution greatly augmented. Overall, this phenomenon can be interpreted utilizing the fact that at greater AoA the manifestation of strake vortex in suction pressure peak is unmistakable as the strength of wing vortex clearly diminishes. In addition to that it can also be seen that interplay between these two-vortex structure at double delta wing model junction influence in slight decrease in suction pressure peak at c–section (x/c =0.65) and its following sections. It can also be seen that similar to the observation from oil flow visualization the reattachment location moves further inboard which shows that flow remains separated for longer duration at elevated AoA.

At 25° AoA starting for strake-wing junction portion of double delta model and onwards the pressure distribution peaks diminishes compared to previous angles of attack and becomes more flatter profile as seen in Figure 5.4(f). This might be due to the reduction in overall vortex strength due to breakdown of vortices. Sections located in close proximity of strake potion of model slight improvement in strength of suction peak can be observed. It can also be observed from figure that in merged strake-wing vortices the interplay of strake and wing vortices manifest as single suction peak in pressure distribution. In line with previous observation the reattachment seem to move slightly towards the root chord portion of double delta model. This also can be assumed with movement of reattachment the vortex core also gets transited towards inboard portion of model. Specifically for 25° AoA the reattachment of flow observed to occur in very close proximity of centerline of model.

For 30° AoA from Figure 5.4(g) it can be seen that pressure distribution in almost all of the section in wing portion of the double delta model flat in nature with exception in section located in strake portion. This can be assumed that flow becomes almost detached in nature over the wing portion leeward surface of model. This flatter pressure profile also might be due to dissipation of vortex structure in downstream portion of wing. Upon close observation it can also be noted that suction pressure peak incrementally diminishes its strength towards the downstream sections of the double delta model.

5.4 Pressure Contour:

Surface pressure data is plotted in contour form for different angles of attack by using commercially available software SURFER. Surface pressure contour plots are made for better understanding of the flow phenomena happening over the double delta model leeward surface. From Figure 5.5(a) it can be seen that there is very few contour lines in strake part of the double delta model at 0° AoA. This might be due to absence of strake vortex at 0° AoA, which is also in line with the previous observations. In the in board portion of central region of wing a scarcity of contour line indicate presence of attached flow. Upon close scrutiny initiation of iso-pressure lines can be seen close to strake-wing junction of double delta model. This might be because of initiation of wing vortex formation. At 5° AoA in Figure 5.5(b) the contour lines appear to be distributed in similar fashion as observed from 0° AoA. Figure 5.5(c) illustrates that at 10° AoA appearance of pressure contour lines in strake portion of model suggests the formation of strake vortices. Scarcity of iso-pressure line in the central region of wing might be because of flow of attached nature. Formation of strake vortices can also be observed at 15° AoA from Figure 5.5(d). For 20° AoA Figure 5.5(e) indicate formation of strake vortices with significant amount of contour lines. Additionally, more contour lines in central region of the double delta model might be due to movement of reattachment region towards the inboard portion of model. Form Figure 5.5(f) and Figure 5.5(g) it can be observed that at 25° and 30° angles of attack further dispersion of contour lines can be observed close to trailing edge in wing portion of the doubled delta model. This phenomenon is an indication of movement of vortex dissipation region towards the leading edge of the model, which is also observed from the previous discussions. This

dispersion of contour lines are observed in wing portion of model. Density of contour lines in strake portion of model gets enhanced.

5.5 Velocity Distribution

For augmentation of the experimental findings, as discussed in previous sections, and for better understanding of the flow behaviour of the flow over and above the wing surface, a pre-calibrated three-hole probe was employed. The understanding was to plot velocity profiles at different AoAs for comparative analysis. Due to experimental limitations the investigation was restricted to 0º and 10º AoA at $Re_{MAC} = 1.46 \times 10^5$. No slip condition was considered at wing surface such that stream velocity will be zero at surface and will increase with increasing height from the surface.

Figure 5.6 and Figure 5.7 represents mean velocity (u) distribution at selected stations over the wing surface. Velocities along all stations were normalised with free stream velocity (u_∞). Similarly the distances over the wing surface were non-dimensionalized with root chord of the wing. For the present study half wing was considered for measurement including line of symmetry. Exposed half wing was distributed with 28 stations for measurements but for 0º AoA, only 16 stations were measured. This was due to the understanding that at this arrangement, the flow mostly attached, as observed in previous methods of experiments. The stations were marked as a, b, c, d and e where a is located at close trailing edge aft portion of the wing section (discussed in section 5.3).

Experimental results observed that at 0º AoA [Figure 5.6], mean velocity attains free stream velocity very close to wing surface at the strake portion of the wing (e section). As the flow approaches wing portion trailing edge, attainment of free stream velocity occurs at moderately elevated distance from the double delta wing model surface. This phenomenon can be observed at stations in near proximity of the edges of wing portion of model. At 10º AoA, as per the previous observation from the oil flow and surface pressure distribution experiments the velocity also seem to indicate the presence of vortex formation. Upon close observation the wavy nature of velocity distribution seem to indicate the presence of vortex generated because of the influence of strake portion and wind portion of the model [Figure 5.1(c)]. The observations of mean velocity distribution at 10º AoA are plotted in Figure 5.7. Here also at the symmetry line, there seem to be indication of minimal influence of any vortex flow, the velocity is stable

and attains free stream velocity very close to wing surface. As we approach span wise towards the edges, the velocity distributions become unstable and fluctuating in nature. This may be due to the effect of the two vortex formed as discussed earlier.

By using equation 3.9 and 3.10 and the calibration constants of the 3-hole probe, as discussed in section 3.5.2, the components of mean velocity were obtained. These components are namely chord-wise or stream-wise component (u_x) and span-wise or transverse component (u_y). Obtained values were plotted similarly as mean velocity plots. Figure 5.8 and 5.9 represents chord-wise velocity distribution in all measured location at 0º and 10º AoA respectively, whereas Figure 5.10 and 5.11 shows distribution of span-wise velocity at 0º and 10º AoA.

Figure 5.9 shows that at 0 º AoA, flow over the leeward surface is steady and it contributes mean velocity majorly. At 10º AoA, Figure 5.9, some fluctuations were observed in the outboard sections of the wing. This may be due to the initial stage of creation of vortices. Figure 5.10 shows that there is negligible existence of span-wise component at 0º AoA. At 10º some variations were observed that corroborate previous observation.

5.6 Two-Grid Vector Plot

To further visualize the effects of the velocity components in the immediate vicinity of the wing's leeward surface, two-grid vector graphs were plotted using the commercial software 'Surfer'. This two-grid vector map primarily utilizes distinct grid files for each velocity component to estimate the vector direction and magnitude at the specific height under investigation. For the present study, two-grid vector graphs were created by employing grids of the stream-wise and transverse velocity components. These grids of both the longitudinal and lateral velocity components were generated for 1mm and 2mm normal distances over the wing's leeward surface.

It has been observed from the vector plots at 1mm normal distance over the wing surface, that at 0° AoA, Figure 5.12, the velocity vector are aligned with the chord line and magnitude of the velocity vectors are slightly higher near the leading edge region and reduces towards the trailing edge. However, at 10° AoA, Figure 5.13, the velocity vectors are no longer aligned with the chord line and changes in their direction towards outboard near the trailing edge. Also, it was observed that magnitude of velocity is reduced towards the trailing edge.

The vector plots at 2mm normal distance over the wing surface show that the magnitude of the velocity vectors is lower compared to the 1mm case and the trend of velocity vector direction along the chord remains the same in the middle portion (Figure 5.15). At 10° AoA, increase in strength of the vector is observed (Figure 5.14).

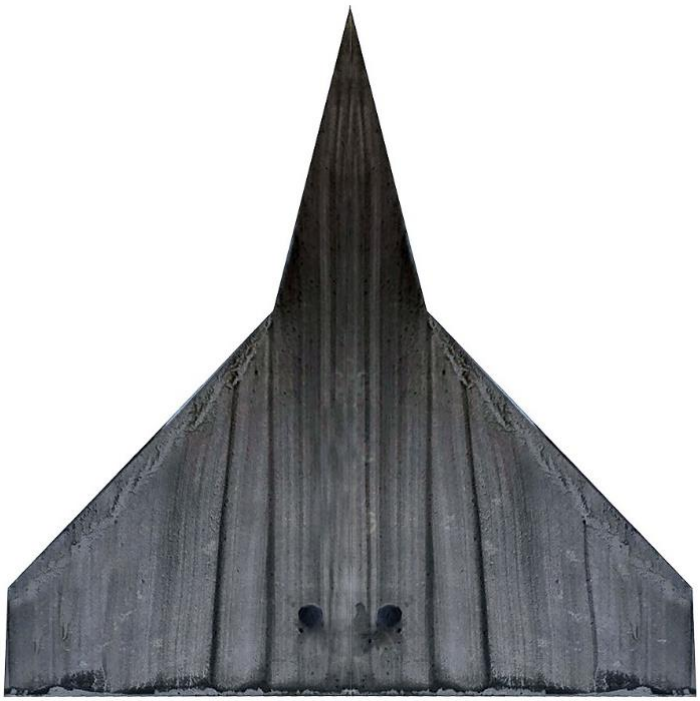

Figure 5.1(a) Oil Flow visualisation at 0º AoA

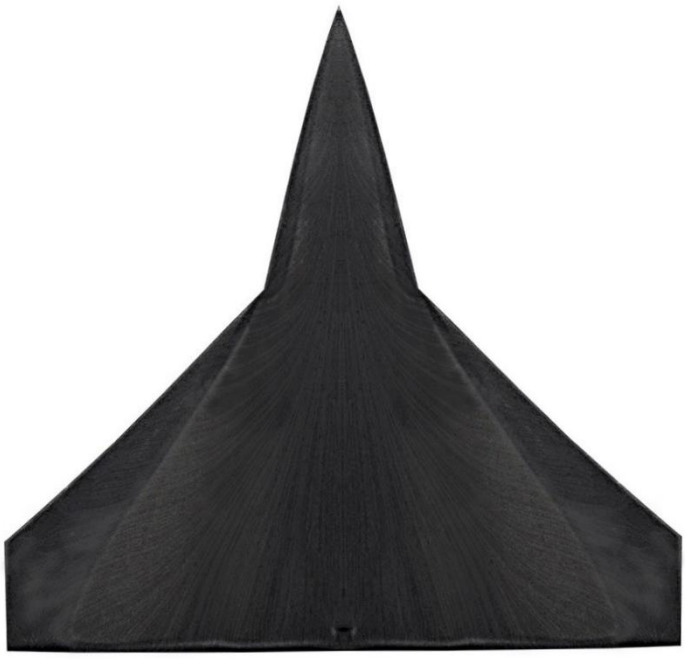

Figure 5.1(b) Oil Flow visualisation at 5º AoA

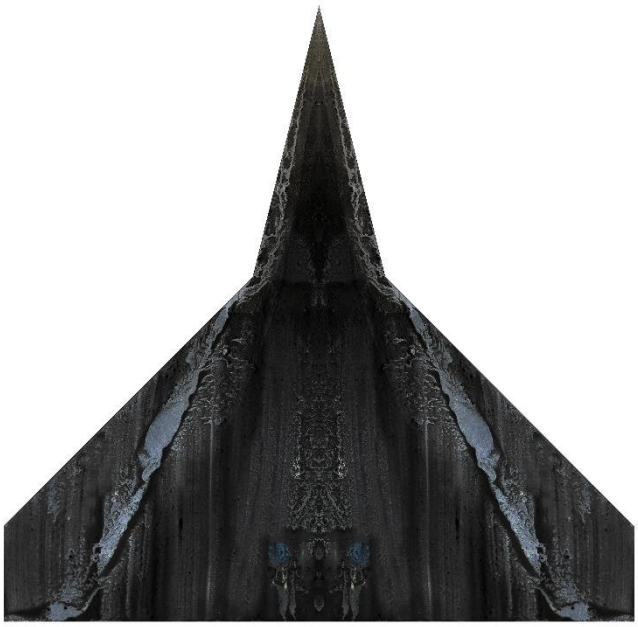

Figure 5.1(c) Oil Flow visualisation at 10º AoA

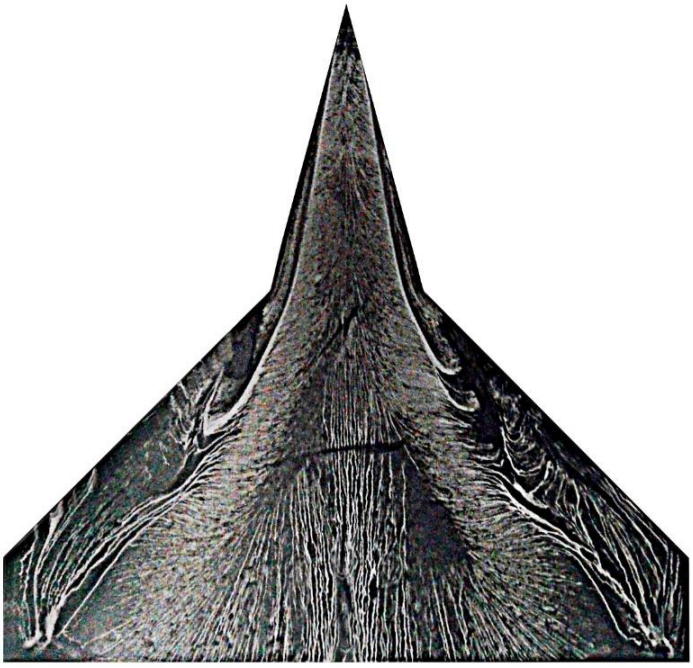

Figure 5.1(d) Oil Flow visualisation at 15º AoA

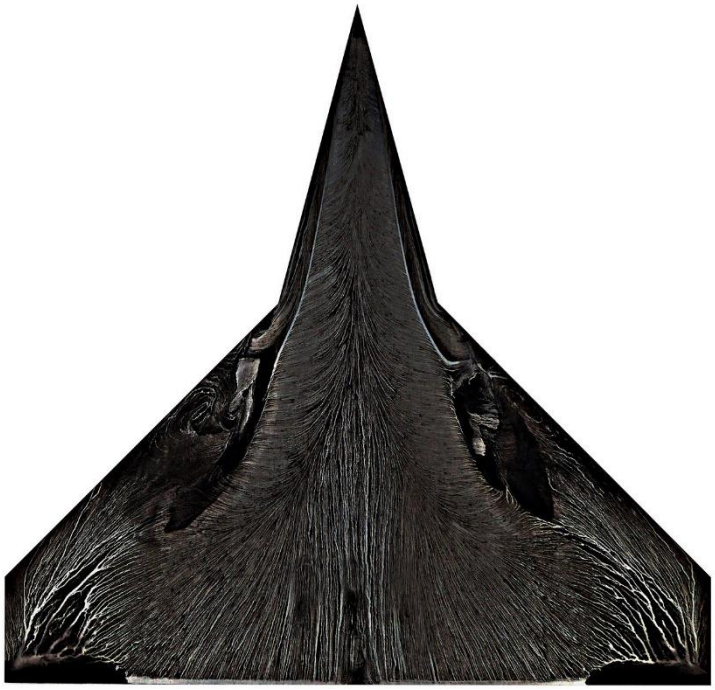

Figure 5.1(e) Oil Flow visualisation at 20º AoA

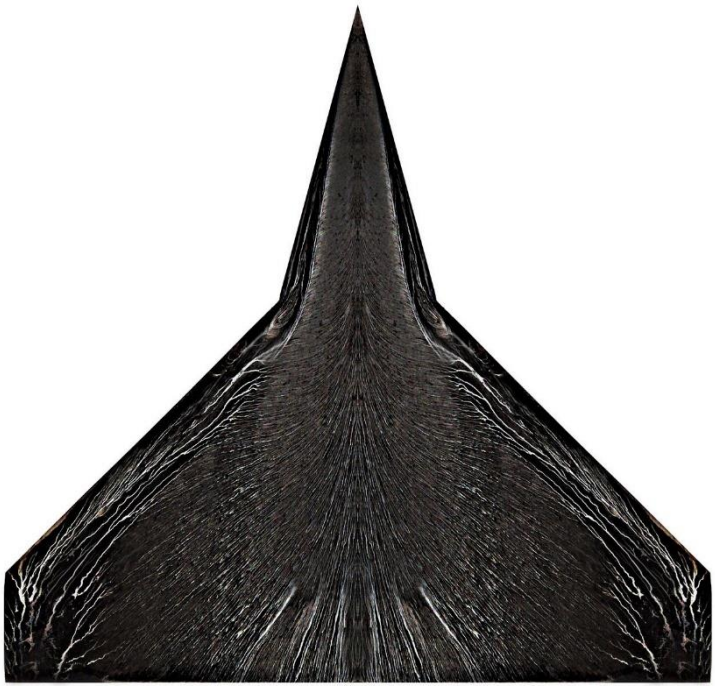

Figure 5.1(f) Oil Flow visualisation at 25º AoA

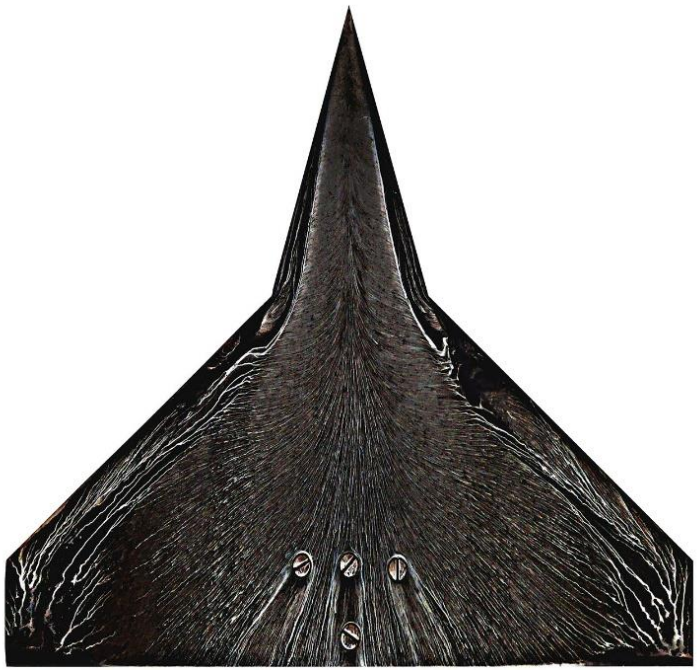

Figure 5.1(g) Oil Flow visualisation at 30º AoA

Figure 5.1 Oil Flow visualisation of model wing at (a) 0° AoA, (b) 5° AoA, (c) 10° AoA, (*d*) 15° AoA, (*e*) 20° AoA, (*f*) 25° AoA, (*g*) 30° AoA, [Experimental]

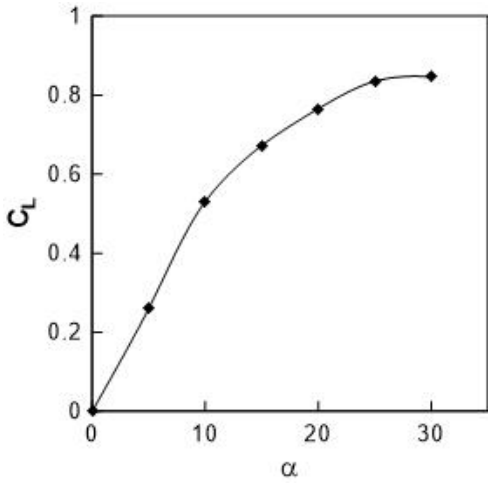

Figure 5.2(a) Experimental variation of lift coefficient with AoA

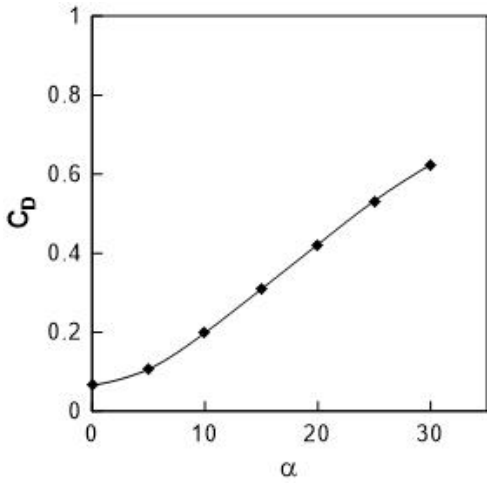

Figure 5.2(b) Experimental variation of drag coefficient with AoA

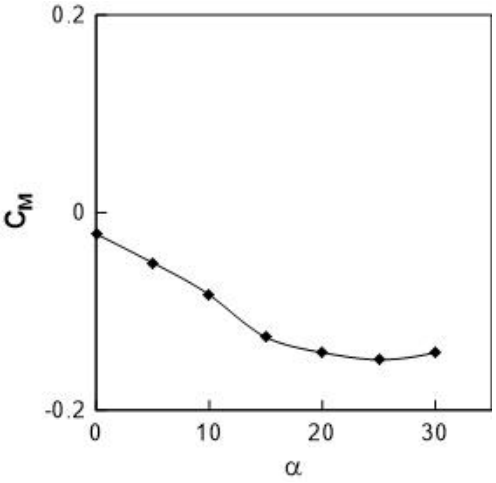

Figure 5.2(c) Experimental variation of moment coefficient with AoA

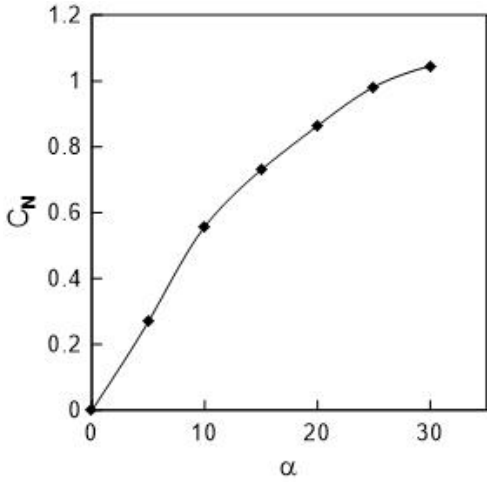

Figure 5.2(d) Experimental variation of normal force coefficient with AoA

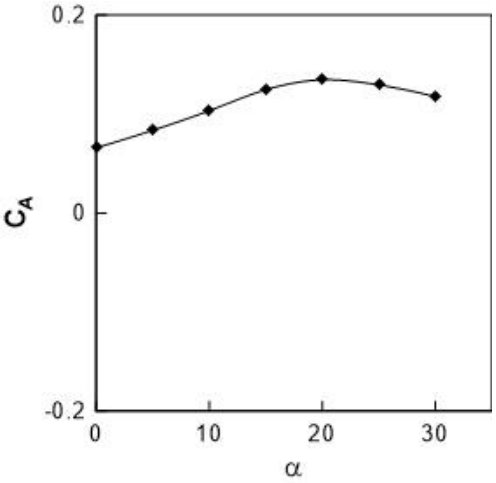

Figure 5.2(e) Experimental variation of axial force coefficient with AoA

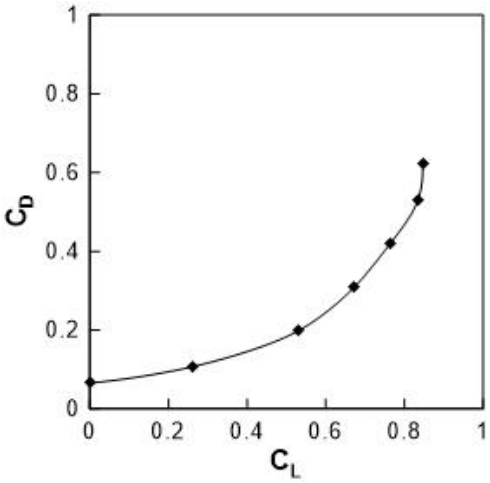

Figure 5.2(f) Experimental variation of lift coefficient with drag coefficient

Figure 5.2 Experimental variations of aerodynamic properties

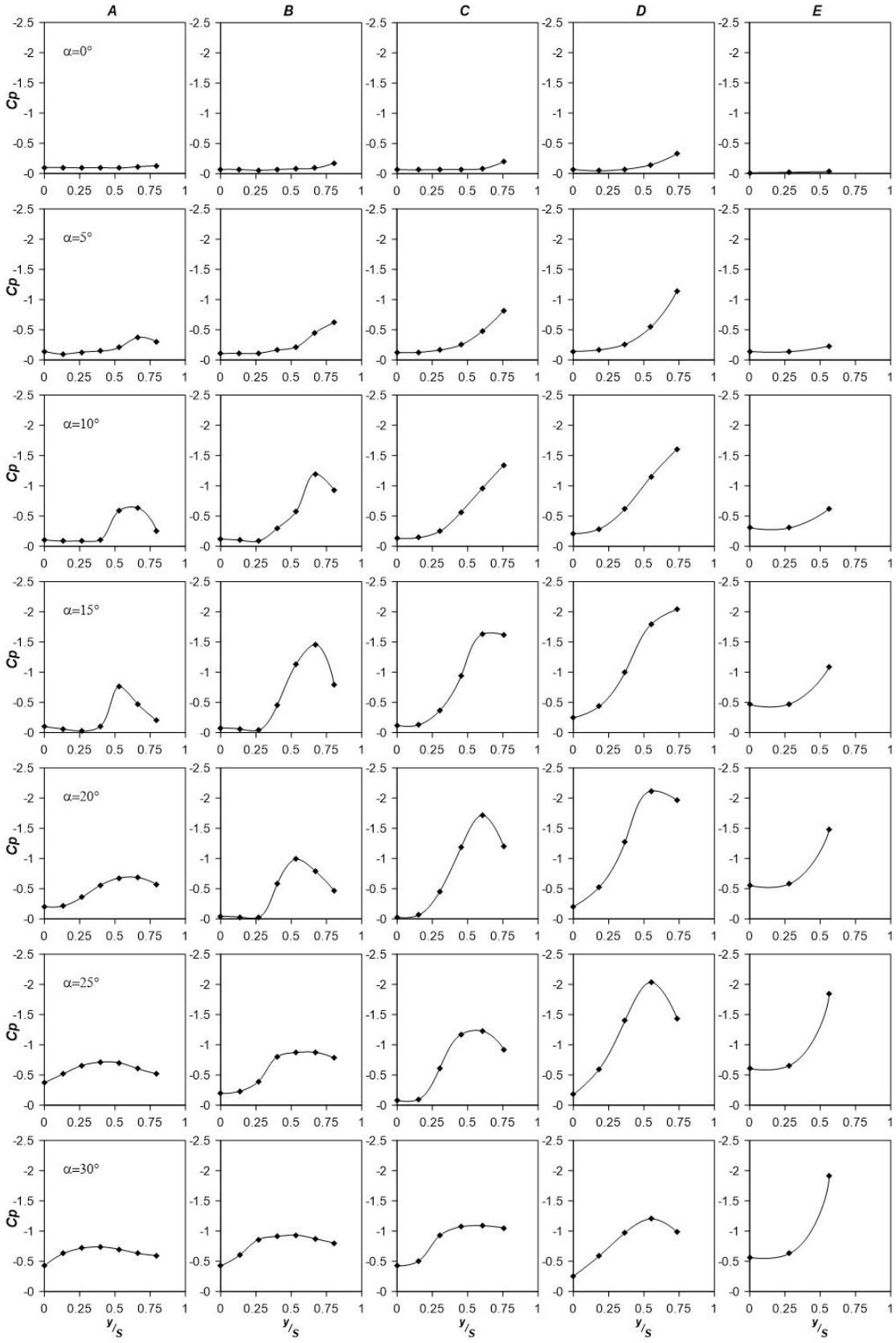

Figure 5.3 Experimental variation of C_p distribution over wing leeward surface

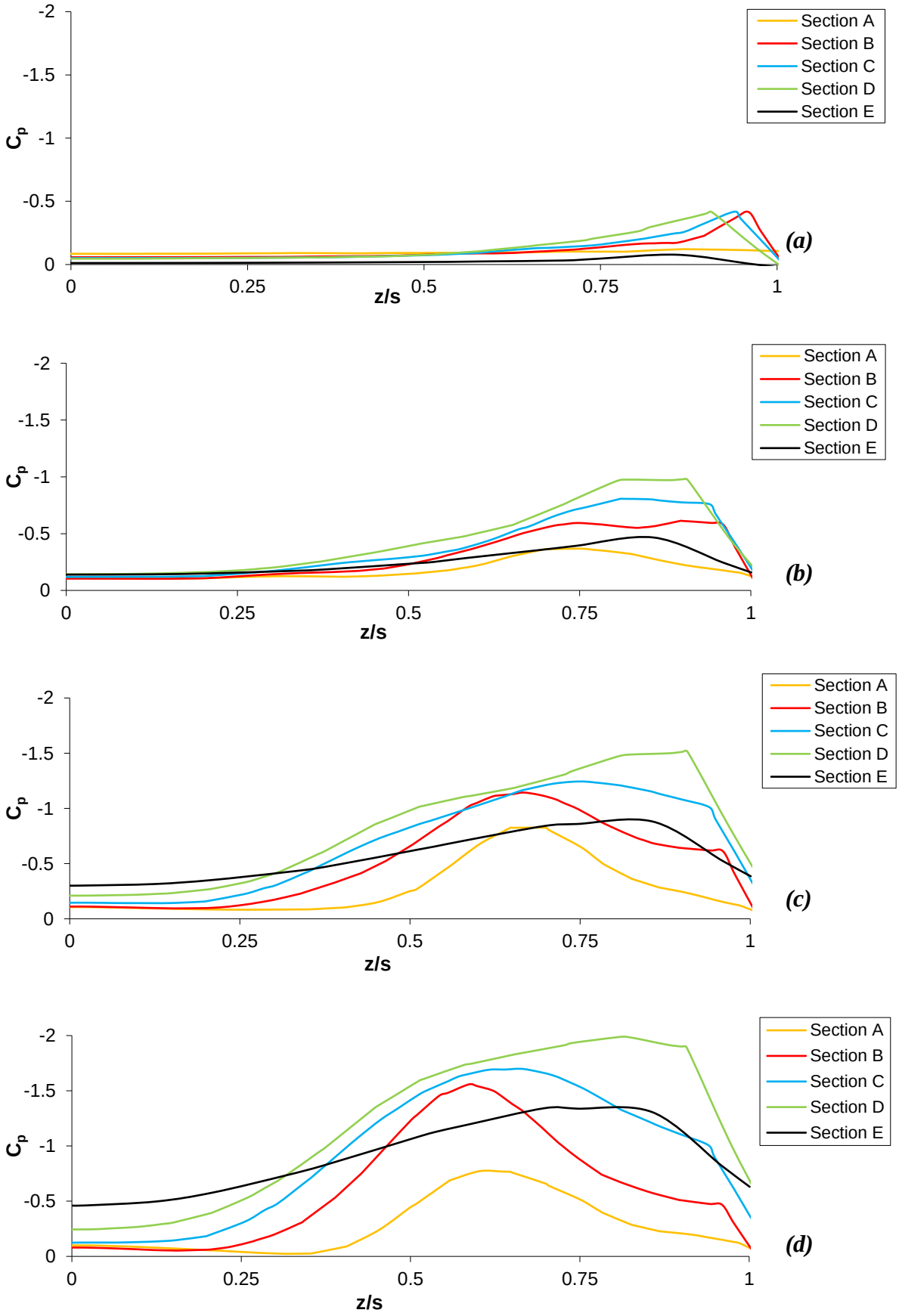

Figure 5.4 Cp distribution half span of model wing, [Experimental] contd…

(a)

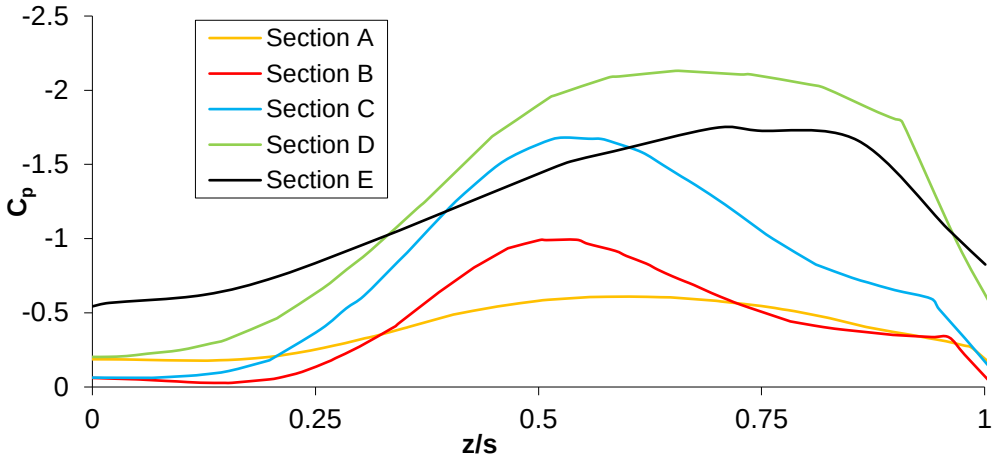

(e)

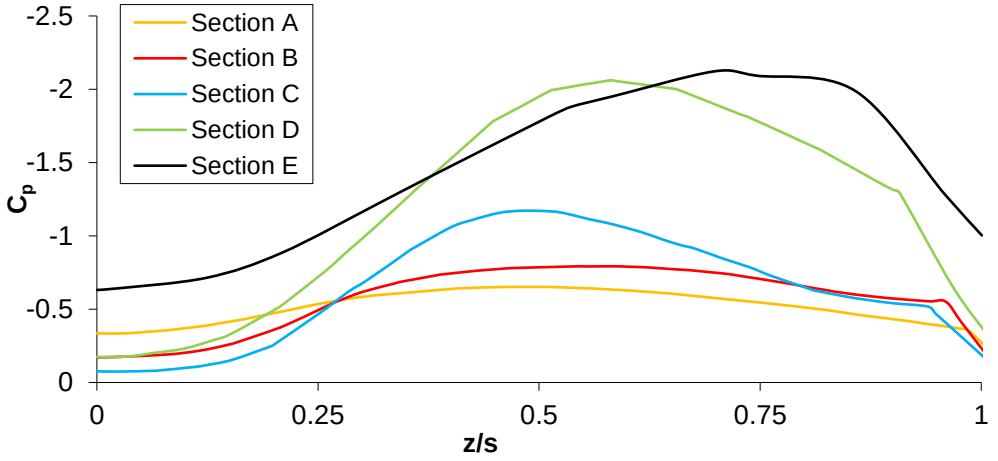

(f)

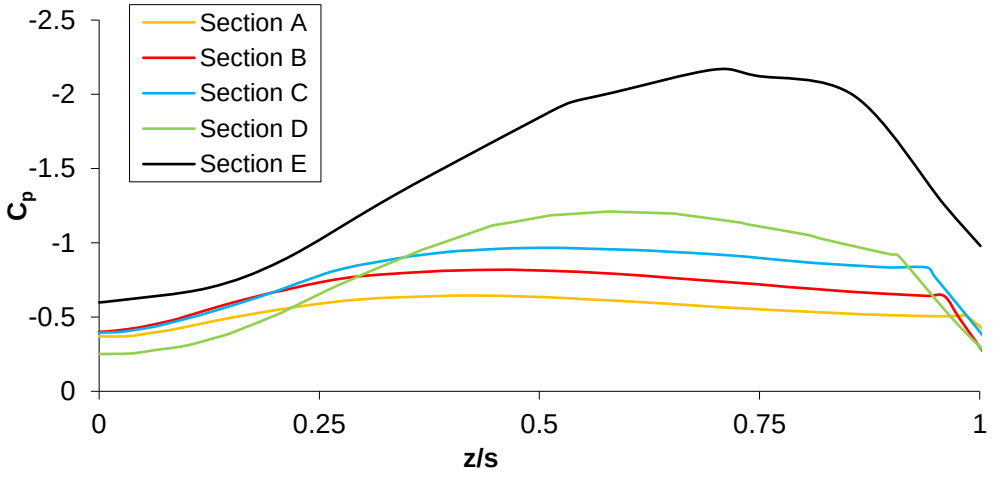

(g)

Figure 5.4 C_p distribution half span of model wing at (*a*) 0° AoA, (*b*) 5° AoA, (*c*) 10° AoA, (*d*) 15° AoA, (*e*) 20° AoA, (*f*) 25° AoA, (*g*) 30° AoA, [Experimental]

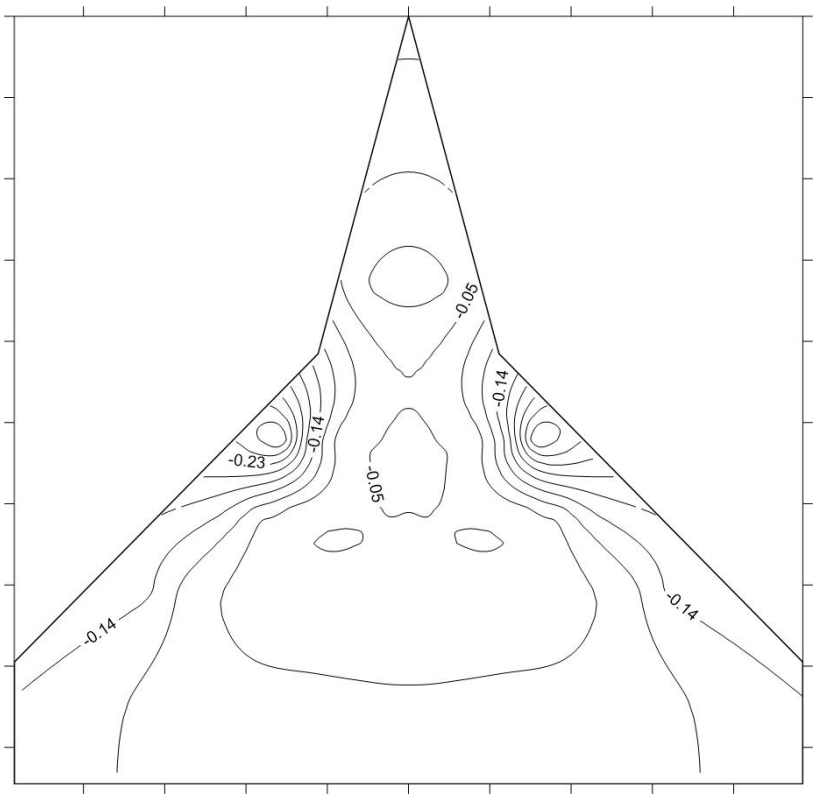

Figure 5.5(a) Contour of Cp over wing leeward surface at 0º AoA [Experimental]

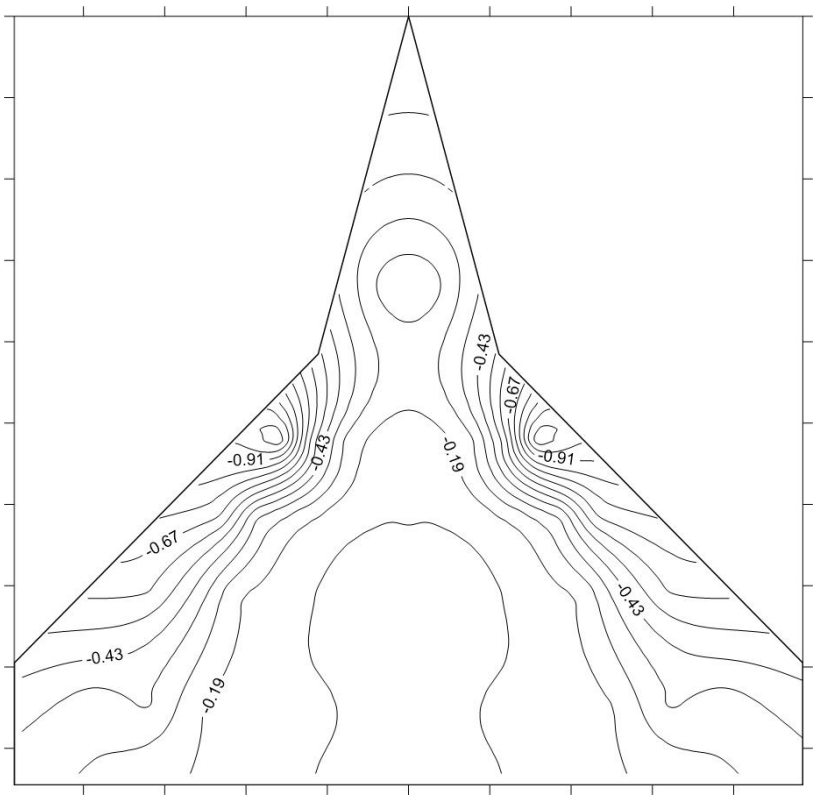

Figure 5.5(b) Contour of Cp over wing leeward surface at 5º AoA [Experimental]

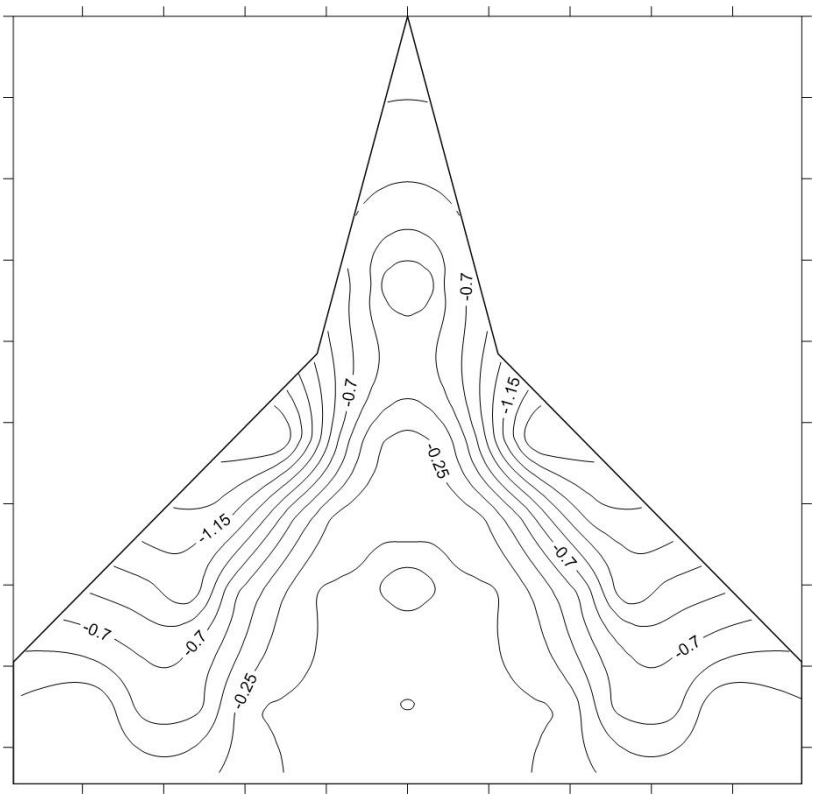

Figure 5.5(c) Contour of Cp over wing leeward surface at 10º AoA [Experimental]

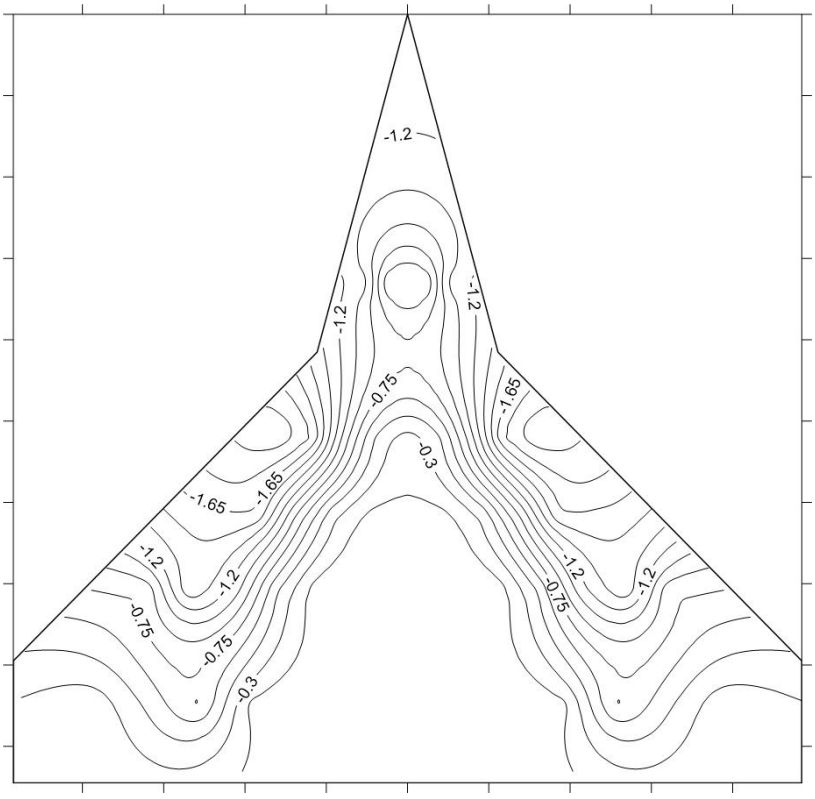

Figure 5.5(d) Contour of Cp over wing leeward surface at 15º AoA [Experimental]

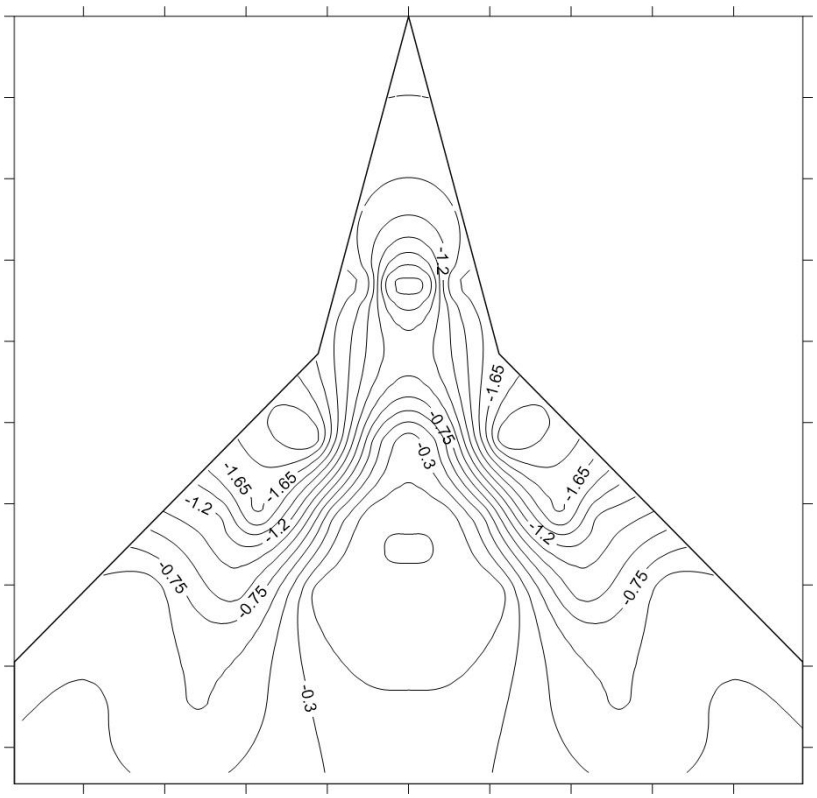

Figure 5.5(e) Contour of Cp over wing leeward surface at 20º AoA [Experimental]

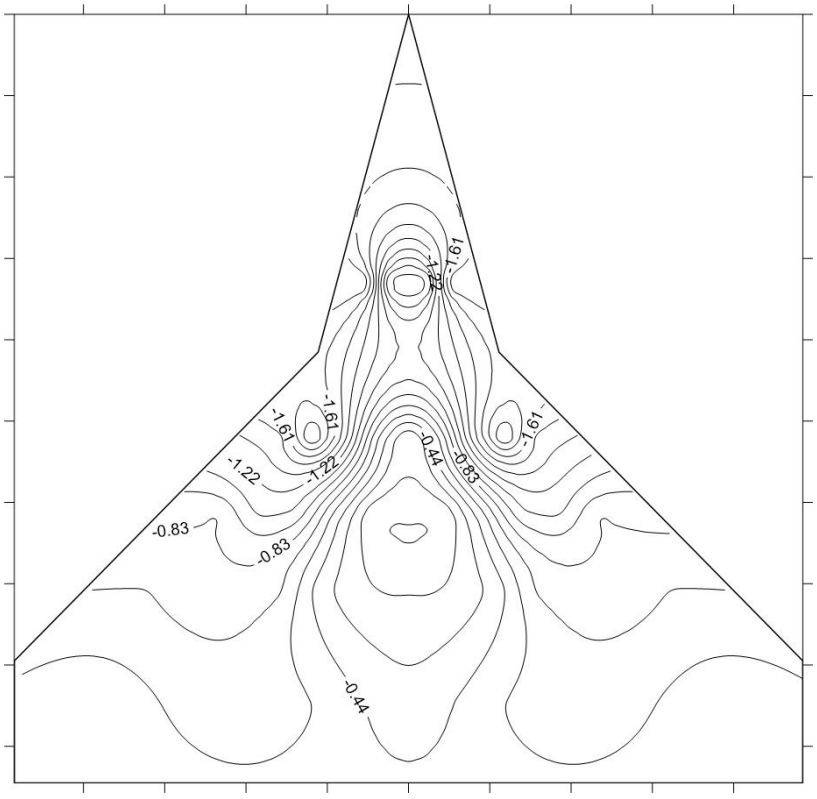

Figure 5.5(f) Contour of Cp over wing leeward surface at 25º AoA [Experimental]

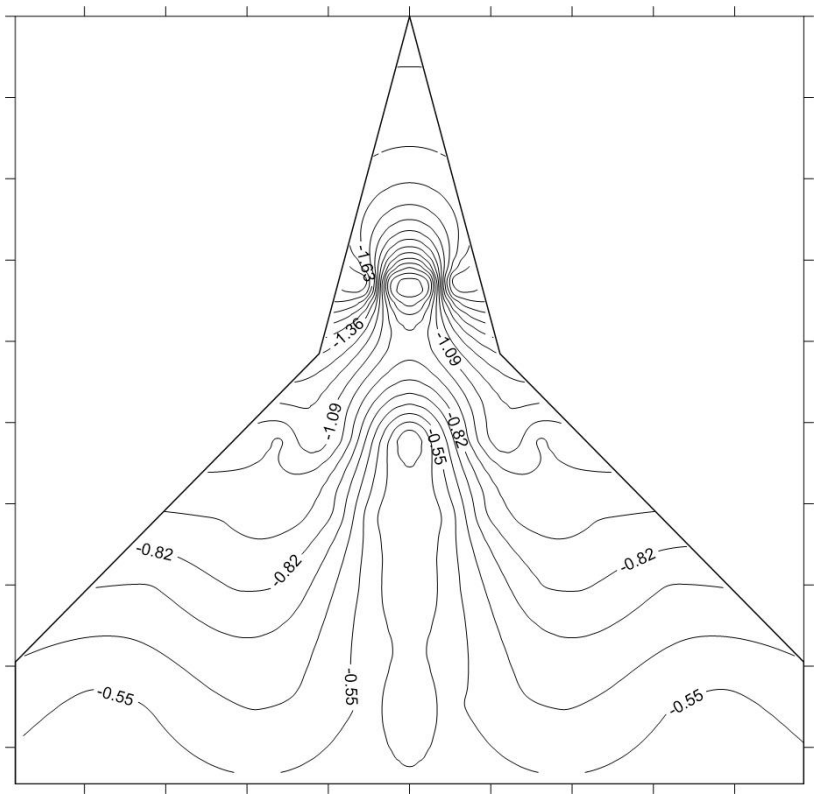

Figure 5.5(g) Contour of Cp over wing leeward surface at 30º AoA [Experimental]

Figure 5.5 Contour of Cp over wing leeward surface at (*a*) 0° AoA, (*b*) 5° AoA, (*c*) 10° AoA, (*d*) 15° AoA, (*e*) 20° AoA, (*f*) 25° AoA, (*g*) 30° AoA, [Experimental]

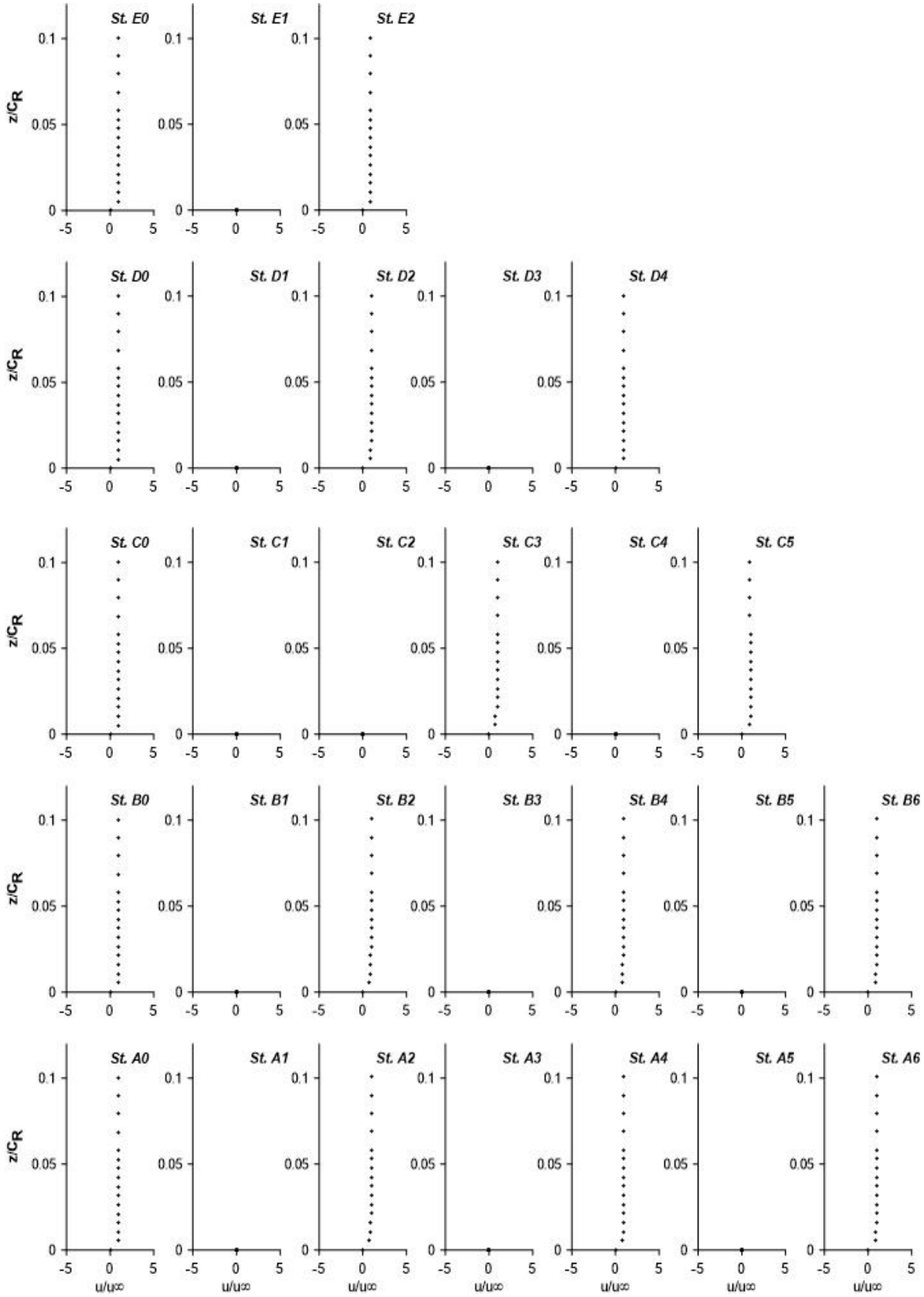

Figure 5.6 Variation of mean velocity at 0º AoA, station wise [Experimental]

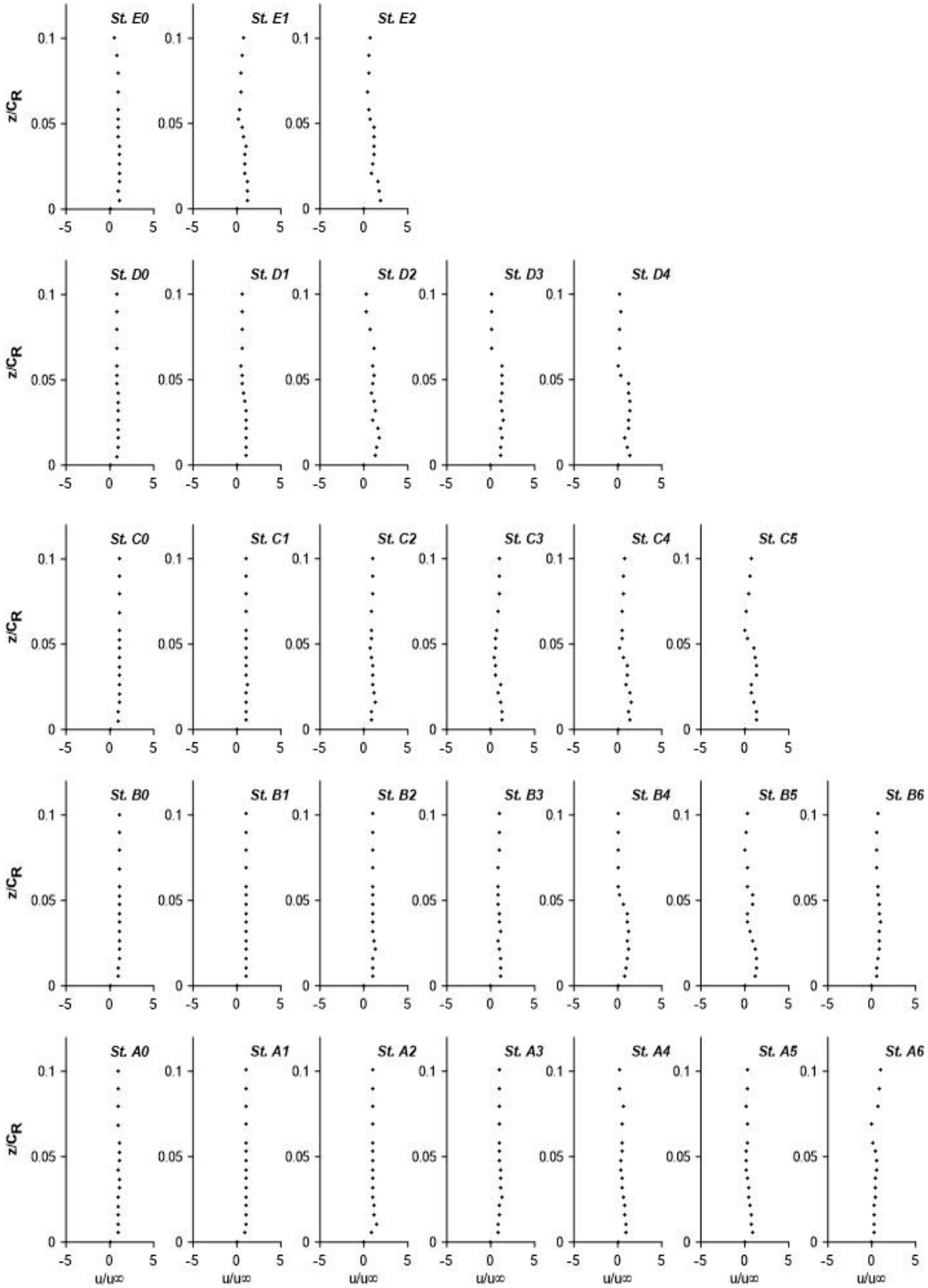

Figure 5.7 Variation of mean velocity at 10º AoA, station wise [Experimental]

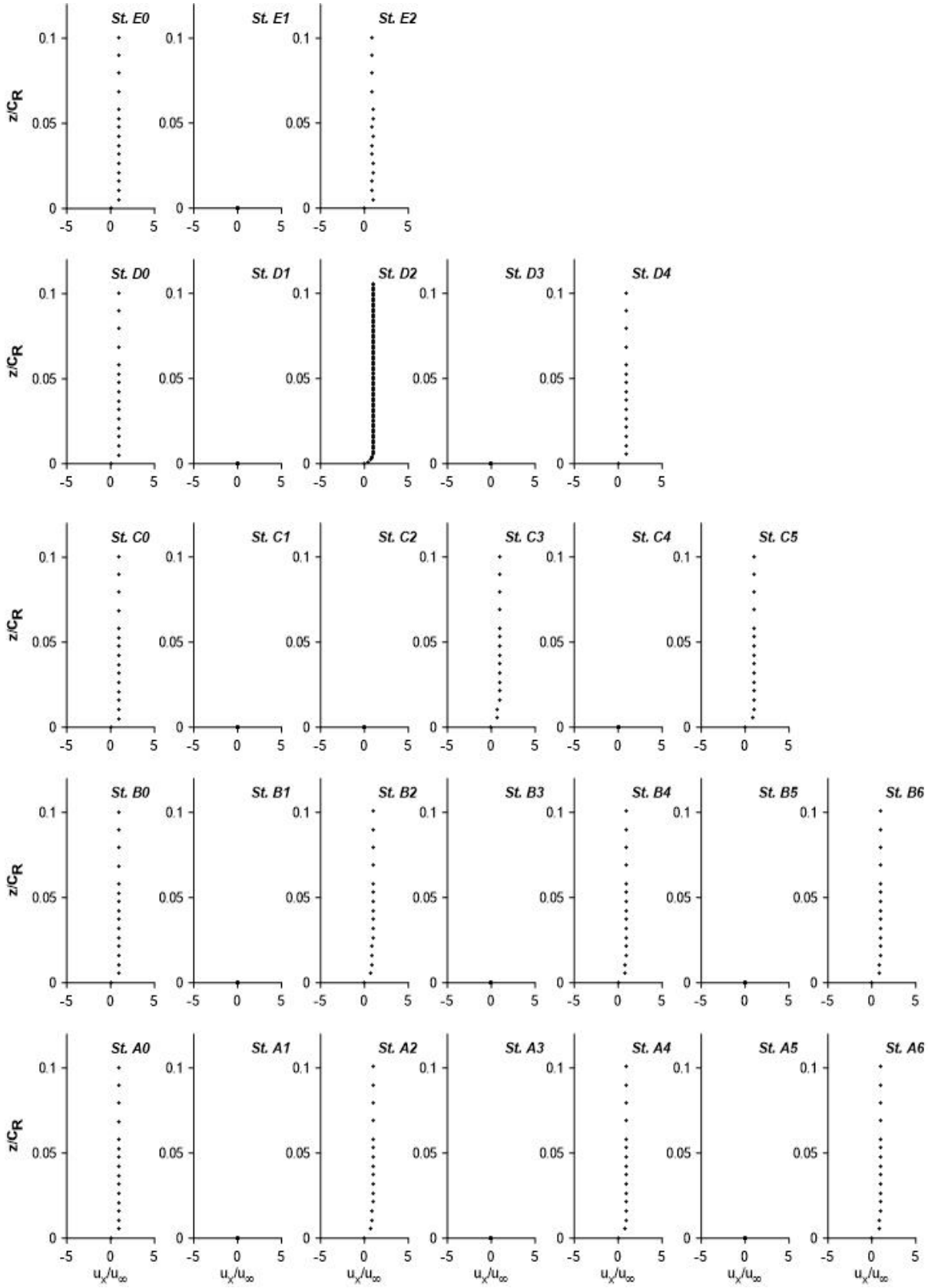

Figure 5.8 Variation of chord wise velocity at 0º AoA, station wise [Experimental]

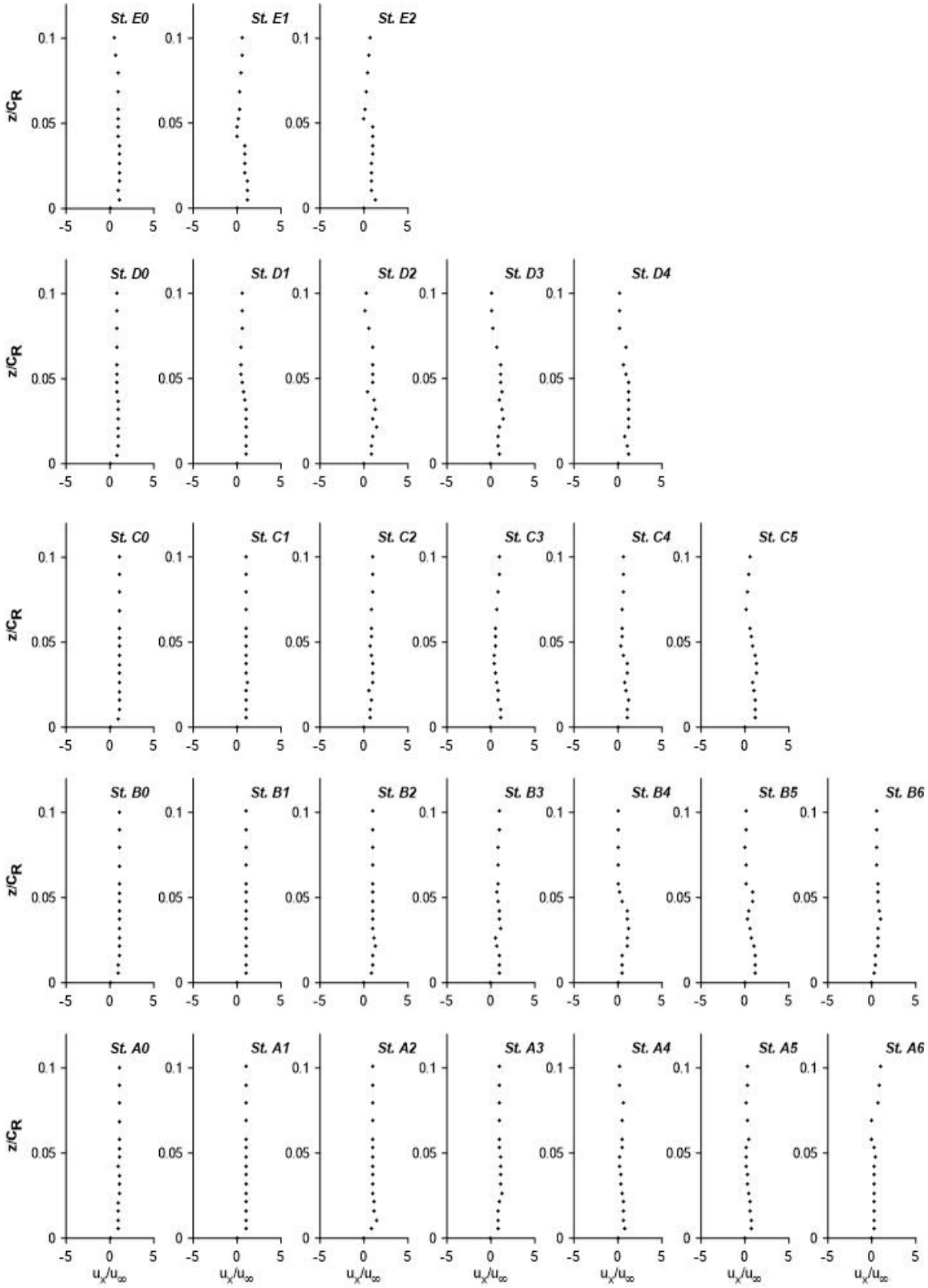

Figure 5.9 Variation of chord wise velocity at 10º AoA, station wise [Experimental]

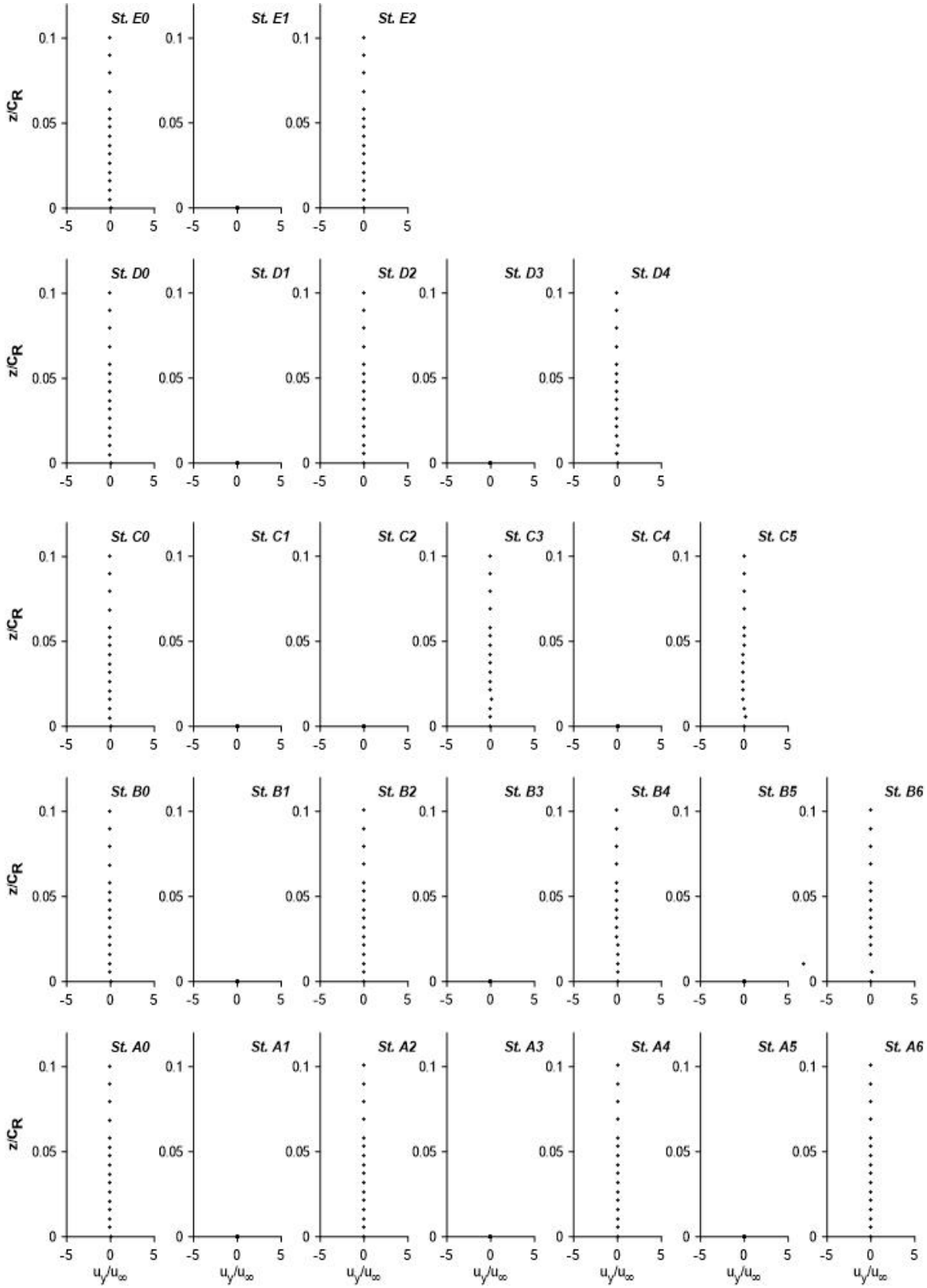

Figure 5.10 Variation of span wise velocity at 0º AoA, station wise [Experimental]

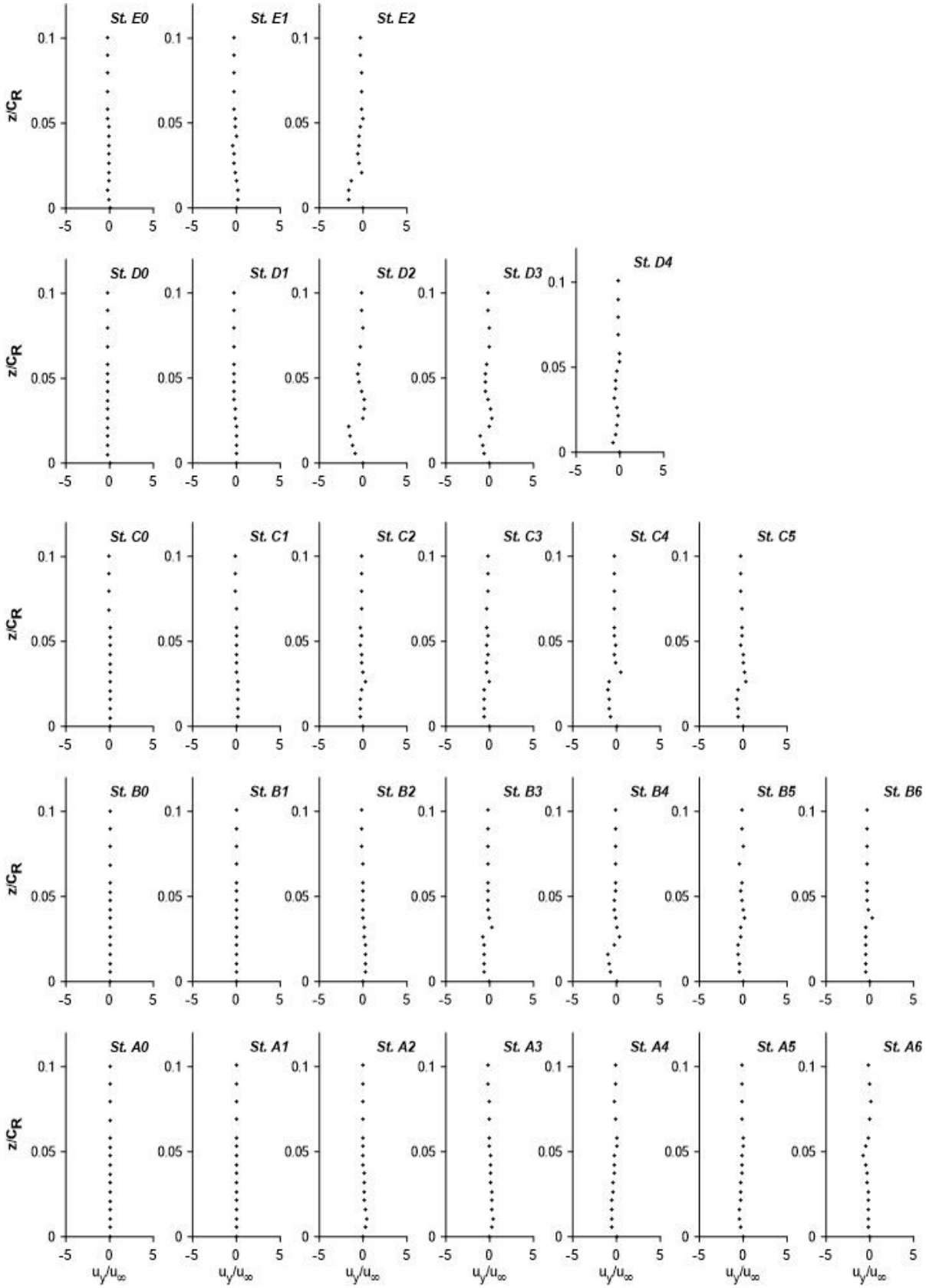

Figure 5.11 Variation of span wise velocity at 10º AoA, station wise [Experimental]

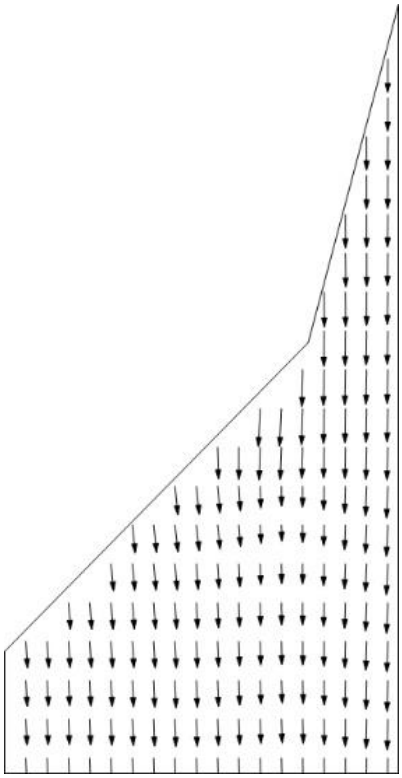

Figure 5.12 2-grid vector plot 1mm above leeward surface at 0 º AoA

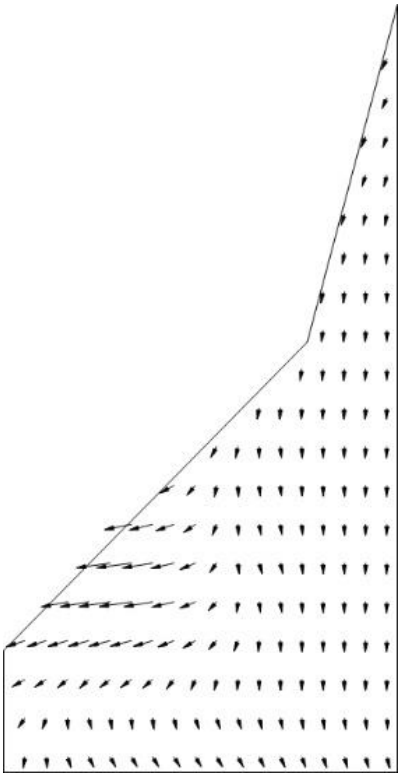

Figure 5.13 2-grid vector plot 2mm above leeward surface at 0 º AoA

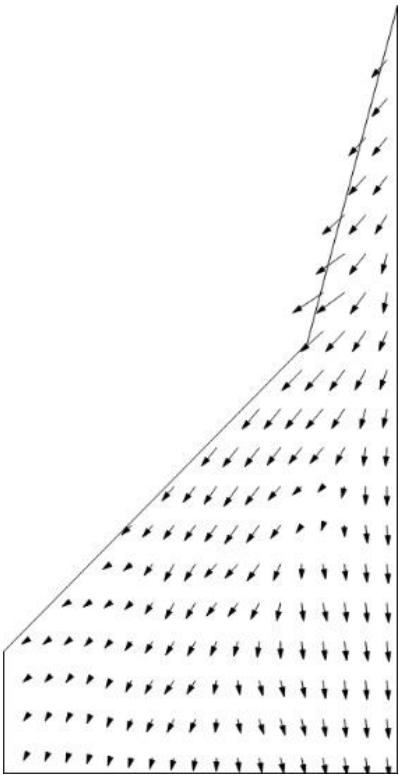

Figure 5.15 2-grid vector plot 1mm above leeward surface at 10 º AoA

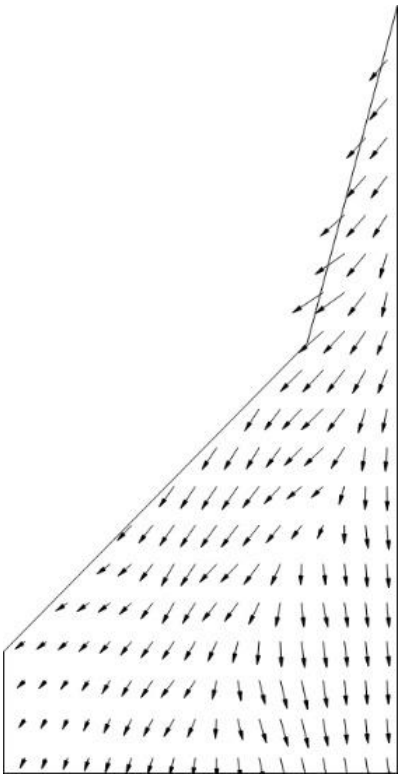

Figure 5.14 2-grid vector plot 2mm above leeward surface at 10 º AoA

CHAPTER 6

Numerical study

This chapter elaborates the comparative study between experimentally obtained results and results obtained from three-dimensional numerical simulation of the Double Delta wing model using Spalart-Allmaras (SA) turbulence model in Ansys Fluent as described earlier. This chapter also presents results of parametric studies for flow over wing models using computational technique. Like experimental investigations, numerical simulation of the wing model was conducted at a free-stream velocity (u_∞) of 12m/s and at $Re_{MAC}= 1.46\times10^5$ at different orientations of angles of attacks.

6.1 Flow Visualization

In order to perform comprehensive study, the experimentally obtained surface flow visualization results are plotted alongside numerically extracted data plots in Figure 6.1. The left portion of the wing represent numerically computed surface flow patterns whereas the right side of the wing portray experimental surface flow visualization results. Figure 6.1 represents both computationally and experimentally obtained surface flow pattern over leeward surface of the wing for angle of attack starting from 0° to 30° within an interval of 5° and at a Reynolds number of $Re_{MAC}= 1.46\times10^5$.

From Figure 6.1(a), at 0° angle of attack, numerically extracted surface flow distribution on the left side of wing exhibit close resemblance with its experimental counterpart. It can be seen that the flow patterns formed in both experimental and numerical method mostly move towards trailing edge primarily following linear fashion for both strake and wing portion of the wing. Formation of vortices, separation and attachment structure are found to be almost nonexistent. As a result it can be concluded that the flow over the leeward surface of the wing exhibit nature of almost attached flow over the entire portion of wing.

At 5° angle of attack, Figure 6.1(b), indicate towards possible formation of vortex through the formation of flow pattern in both experimental as well as numerical counterpart. Appearance of attachment and separation structure patterns in the strake portion signal towards probable formation of vortex (Strake Vortex). Addition to that formation of attachment and separation structure can also be observed starting from

close to junction of strake and wing towards outboard portion suggest formation of wing vortex likewise.

Figure 6.1(c) illustrates the comparative representation of flow pattern observed at 10° angle of attack as obtained from both numerical and experimental methods. More prominent formation of flow pattern suggests both strake and wing vortex formation which is stronger in nature. Distorted flow lines can be seen in the close proximity of wing tip region from both experimental and numerical results. Upon close inspection slight inboard shift of strake and wing vortex can also be observed in both experimental and numerical results and it be the result of stronger and bigger vortices with increment in angle of attack.

Figure 6.1(d) and Figure 6.1(e) indicate the formation of surface flow patterns at 15° and 20° angles of attack acquired from both experimental and numerical approach. It can be seen that at both these angles of attack a merging of strake and wing vortex can observed from the formation of flow pattern close to junction of strake and wing. Upon close scrutiny it can also be observed that with increment in angle of attack from 15° to 20° there is indication of slight movement of strake vortex towards outboard portion of wing. In comparison to that there is a slight shifting of wing vortex towards inboard portion with increment in angle of attack.

Configuration of flow pattern obtained from both experimental and numerical method at 25° and 30° angles of attack are demonstrated in Figure 6.1(f) and Figure 6.1(g). The figure depicts the flow pattern arrangement that both strake and wing vortices becomes incrementally more indistinguishable in nature at theses higher angle of attack. Here amalgamation of both strake and wing vortices becomes more interlaced with each other generating a vortex core, which sweep over the entire region. It can also be seen that with increment in angles of incidence reattachment pattern appear to move towards outboard portion of wing and in turn reducing region of the pattern formation. The numerical results exhibit qualitatively close agreement with experimental counterpart.

6.2 Force Analysis

Figure 6.2 illustrates the comparative plots of data obtained from both experimental and numerical methods for aerodynamic parameters such as lift coefficient (C_L), drag coefficient (C_D), moment coefficient (C_M), normal force coefficient (C_N), and axial

force coefficient (C_A) etc. The experimental and numerical data provide an allegorical nature of these parameters obtained from both methods.

Figure 6.2(a) shows the variation in lift coefficient (C_L) with correspondence to angles of attack. It can be seen that in the same manner as observed from the experimental results numerically calculated lift coefficients also indicate change in rate of increase following 10° angle of attack with appearance of merging of strake and wing vortices upon wing leeward surface. It can be seen that following the nature of experimental counterpart after 15° angle of attack the rate of growth in lift coefficient gets sluggish. From Figure 6.2 (b) it can be seen that drag coefficient (C_D) also indicate change in rate of variation post 10° angle of attack as discussed in experimental analysis. Moment coefficients (C_M) show visible alteration in rate in between 10° and 15° angles of attack in Figure 6.2 (c). Figure 6.2 (e) further depicts that lift coefficient appears to increase sluggishly accompanied with rapid rise in drag force post 10° angle of attack in case of numerical results as well as experimental observations.

Hence overall it can be seen from Figure 6.2 that numerically obtained results exhibit qualitatively similar pattern very close to each other with their experimental counterpart. Also the conclusions and observation formed from experimental results remains indistinguishable from the observations made with numerical data.

6.3 Surface Pressure Distribution

Surface pressure distribution on the 75°/45° double delta wing model leeward surface is shown in Figure 6.3 for varying angle of attack between 0° to 30° with interval of 5°. Here the pressure distribution extracted from both experimental as well as numerical methods are plotted against z/s, where z is distance measured along span-wise direction of wing model and *s* is defined as span of wing model. In this case, the line represents the pressure distribution obtained from numerical method and experimental data are represented with points.

In a similar fashion to previous discussion on experimental surface pressure distribution here the experimental and numerical data were plotted in combination for different angles of attack in Figure 6.3 for comparative analysis. In this figure different row portrays different angle of attack starting from the topmost row for 0° angle of attack and bottom most row for 30° angle of attack. Different columns represents different pre-determined sections over the double delta model leeward surface, starting a-section

located in the left most columns and right most columns indicate e-section with all other sections are placed in between.

From Figure 6.4 (a), it can be seen that at 0° angle of attack the numerically extracted pressure coefficient graph lies as almost horizontal line along span wise direction, which indicate probable absence of separation or vortex structure over the wing leeward surface. Flow physics at this angle of attack remains fairly straight forward in nature. At almost all 5 different sections along chord-wise location illustrate flow attached in nature.

Figure 6.4 (b) illustrates the numerical pressure coefficient distribution at 5° angle of attack. It can be observed that suction peak pressure begins to emerge in the plot as a result of increased pitching angle. Overall the curves are almost entirely insipid in nature with exclusive presence of rapid rise in pressure coefficient or suction pressure peak near the edge of the double delta wing model. Appearance of this sudden peak in surface pressure distribution suggests the change in pressure coefficient due to onset of vortex structure. Nature of these vortex structures can also be anticipated from these pressure coefficient distribution plots. At this particular 5° angle of attack the vortex made at strake part is almost indiscernible. The suction peak can be seen to be around $z/s = 0.9$ with an exception for a-section ($x/c = 0.92$) as a consequence of being located close to main wing portion of the double delta model. It can also be seen that with movement towards aft portion of the model pressure distribution attains less negative value or reaches lower peak value as flow loses strength in downstream portion, as observed from delta wing flow mechanics.

Appearance of distinctive peak in pressure distribution at sections located in strake potion can be observed at 10° angle of attack from Figure 6.4 (c) for both experimental and numerical data. So it can be assumed that formation of vortex structure in the strake portion of wing becomes more perceivable. The suction pressure peak continuously increases indicating growing contribution of strake and wing vortex structure to lift generation of double delta wing model. Upon close scrutiny it can be observed that reattachment location shifts slightly towards inboard portion of double delta model. The observations form experimental values agrees well with numerical data.

Figure 6.4 (d) indicates that following 15° angle of attack the vortex formed in strake portion of double delta model becomes more prominent. From overall surface pressure

distribution plots of entire angles of attack, it can be seen that pressure distribution reaches apex value at around d–section (x/c = 0.55) and following that pressure distributions are accompanied by drop in pressure. This occurrence can be clarified effectively as the strength of the strake vortices continues expanding. Upon close observation the Figure 6.4 (d) also indicates the assistance of strake vortices in vortices structures formed over the leeward surface of double delta model have grown significantly. Also little peak like distribution close to the y-axis before the actual peak in pressure distribution also points towards significant contribution of strake vortices in extra lift generation which is and additional benefit when contrasted with the delta wing. This peak like structure cause by strake vortex is quiet recognizable for e–section (x/c = 0.35) and d–section (x/c = 0.55). At this increased angle of attack the vortex structure seem to be displaced towards the inboard portion of double delta model or root chord, which can be seen in pressure distributions as the progress of reattachment location towards the inboard portion of the doubled delta model.

Figure 6.4 (e) illustrates the pressure coefficient distribution at 20° angle of attack. Here it can be seen that pressure distribution reaches apex at diminished value for downstream flow or sections located close to trailing edge of wing. Comparatively in strake portion of double delta model for e–section (x/c = 0.35) and d–section (x/c = 0.55) the peak in pressure distribution greatly augmented. Overall this phenomenon can be interpreted utilizing the fact that at greater angle of attack the manifestation of strake vortex in suction pressure peak is unmistakable as the strength of wing vortex clearly diminishes. In addition to that interplay between these two vortex structure at double delta wing model junction influence in slight decrease in suction pressure peak at c–section (x/c = 0.65) and its following sections. It can also be seen that the reattachment location moves further inboard which shows that flow remains separated for longer duration at elevated angle of attack.

From Figure 6.4 (f) it can be seen that at 25° angle of attack starting from strake portion of double delta model and onwards the pressure distribution peaks diminishes compared to previous angles of attack and becomes more flatter profile. This might be due to the reduction in overall vortex strength due to breakdown of vortices. Sections located in close proximity of strake potion of model like e–section (x/c = 0.35) and d–section (x/c = 0.55), slight improvement in strength of suction peak can be observed. It can also be observed from Figure 6.4 (f) that in merged strake-wing vortices the

interplay of strake and wing vortices manifest as single suction peak in pressure distribution. In line with previous observation the reattachment seem to move slightly towards the root chord portion of double delta model. This also can be assumed with movement of reattachment the vortex core also gets transited towards inboard portion of model. Specifically for 25° angle of attack the reattachment of flow occurs in very close proximity of centerline of model for e–section (x/c = 0.35) and d–section (x/c = 0.55). For all remaining sections the reattachment position lies close to mid axis.

For 30° angle of attack from figure 6.4 (g) it can be observed that pressure distribution in almost all of the section in wing portion of the double delta model flat in nature except in section located in strake portion. This can be assumed that flow becomes almost detached in nature over the wing portion leeward surface of model. This flatter pressure profile also might be due to dissipation of vortex structure in downstream portion of wing. Upon close observation it can also be noted that suction pressure peak diminishes its strength towards the downstream sections of the double delta model. It can be noted that in summery the numerical results qualitatively display similar behavior as their experimental counterparts.

6.4 Pressure Contour

Surface pressure contour obtained from both experimental and numerical methods are plotted side by side in Figure 6.5 for analyses purposes. In those figures left portion of the double delta model are represented by the contour lines obtained from numerical method and correspondingly the right portion of the images are from the contour lines drawn from experimental data. From Figure 6.5(a) it can be seen that there is very few contour lines in strake part of the double delta model at 0° angle of attack. This might be due to absence of strake vortex at 0° angle of attack, which is also in line with the previous observations. Numerically obtained results show same agreement with experimental results. In the inboard portion of central region of wing a scarcity of contour line indicate presence of attached flow. Upon close scrutiny initiation of iso-pressure lines can be seen close to strake-wing junction of double delta model. This might be because of formation of wing vortex. At 5° angle of attack in Figure6.5(b) the contour lines appear to be distributed in similar fashion as observed from 0° angle of attack. Figure 6.5(c) illustrates that at 10° angle of attack appearance of pressure contour lines in strake portion of model suggests the formation of strake vortices.

Scarcity of iso-pressure line in the central region of wing might be because of flow of attached nature. Formation of strake vortices can also be observed at 15° angle of attack in Figure 6.5(d) for both experimental as well as numerical contour lines. For 20° angle of attack Figure 6.5(e) indicate formation of strake vortices with significant amount of contour lines. Additionally, more contour lines in central region of the double delta model might be due to movement of reattachment region towards the inboard portion of model. Form Figure 6.5(f) and Figure 6.5(g) it can be observed that at 25° and 30° angles of attack further dispersion of contour lines can be observed close to trailing edge in wing portion of the doubled delta model. This phenomenon is an indication of movement of vortex dissipation region towards the leading edge of the model, which is also observed from the previous discussions. These dispersions of contour lines are observed in wing portion of model. Density of contour lines in strake portion of model gets enhanced. Here it can be observed the numerical results qualitative show similar pattern with experimental results.

6.5 Velocity Distribution

Figure 6.6 and Figure 6.7 is a compilation of experimentally achieved and numerically predicted data of mean velocity. Here also the absolute velocity measured or computed were normalized with free stream velocity. Absolute distance over the wing surface was also normalized with root chord. Location of the stations for numerical prediction are exactly same as for experiments. It can be observed that at 0º angle of attack, Figure 6.6, a very close resemblance was found with experimental values to numerical counterparts. Almost in all 16 stations the nature of curves is similar. As the flow is generally attached at 0º AoA, no disturbances were seen in the flow field. But as the angle of attack increased from 0º to 10º, [Figure 6.7] some observations were recorded. In general, the nature of the curves is similar and bears a good resemblance with each other. Especially in the middle portion of the wing, numerical prediction shows a good match with experiment. A close observation shows that as we move towards the edge, all stations show a fluctuation of data. This occurrence can be due to unforeseen experimental or numerical errors. The three-hole probe may affect the complex three-dimensional flow phenomenon during experiment near the edge of the model wing. A non-intrusive type probe would have been more accurate in such cases. On the other

hand, a mathematical model with exhaustive mathematical solver or better meshing technique may help to improve the prediction.

Comparing all the observations as discussed above, it can be stated that, for the particular wing formation and research, experimental outcome shows quiet good qualitative agreement with numerically predicted results. Therefore, with numerically computed data, further analysis was done.

Numerically obtained stream-wise component (u_x) and span-wise component (u_y) were plotted side by side with experimentally obtained data. Figure 6.8 shows transverse velocity component at 0º AoA. As such no deviation observed. At 10º AoA, outboard area shows slight deviation between numerical and experiential values. For span-wise component, Figure 6.10, at 0º AoA, depicts uniformity of results with experiment whereas at 10º (Figure 6.11) deviation at outboard area persists. This may be due to the use of intrusive type instruments in such flow field. Separate study is required for examining the reason behind.

6.6 Two-Grid Vector Plot

As discussed in section 5.6, similar two-grid vector plots were carried out with numerically obtained values of u_x and u_y. Comparison with the experiment is shown in Figures 6.12 to 6.15. By nature, all the plots show good agreement with experiment and numerical values.

6.7 Pathlines

A pathline is a concept in fluid dynamics that describes the trajectory followed by individual particles in a moving fluid over time. It's essentially the path traced by a single particle as it moves through the fluid, influenced by various forces such as pressure gradients and viscous forces. Pathlines provide insights into the behavior and motion of fluids, helping scientists and engineers understand phenomena like fluid flow patterns and turbulence. As we have observed that experiment and numerical values closely follow each other, pathlines were generated in post-processor of the Ansys with the numerical values presented in Figure 6.16.

Figure 6.16(a) depicts the pathline at 0º AoA created in numerical solver. It can be seen that there is no vortical structure present. Flow is attached and mostly appeared as

straight line over the surface. At 5º flow is attached and in almost linear formation in the middle portion of the wing [Figure 6.16(b)]. Appearance of strake vortex is seen from the tip of the wing. From the junction of strake and wing and toward the outboard portion of the wing, another vortical structure was observed. This may mark the onset of wing vortex. Figure 6.16(c) represent the pathline at 10º AoA. It shows both strake and wing vortex are prominent with increased strength. At 15º and 20º AoA, Figure 6.16(d) and 6.16(e), further strengthening of the vortical flow were seen. The wing vortex slightly shifted towards the edge as the angle of attack increases. As the angle increased, both the strake vortex and wing vortex closing each other. In Figure 6.16(f) computed pathline for 25º AoA is presented. It is now become difficult to distinguish between strake vortex and wing vortex. Both these vortex intertwined each other and creates a bigger vortex core. This vortex core spans over larger wing surface. Also as the angle of attack increases, the vortex created seems to disappear close to trailing edge of the wing. Figure 6.16(g) predicts pathline at 30º AoA. The vortical structure is quiet big and spreads over almost entire wing surface. Breakdown of vortex appears very close to trailing edge. Overall, the pathlines follows good agreement with the flow structure as observed in oil flow visualization.

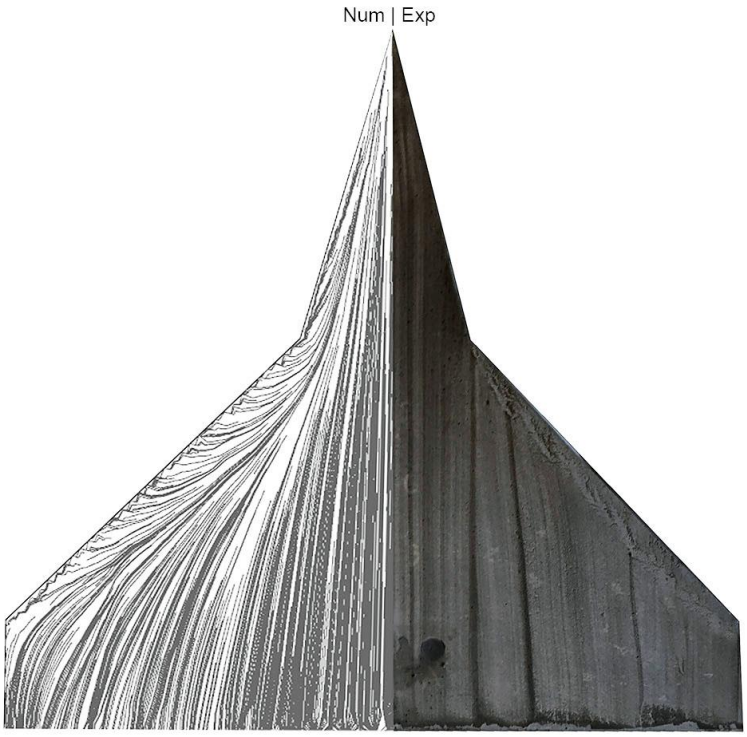

Figure 6.1(a) Oil Flow visualisation at 0º angle of attack

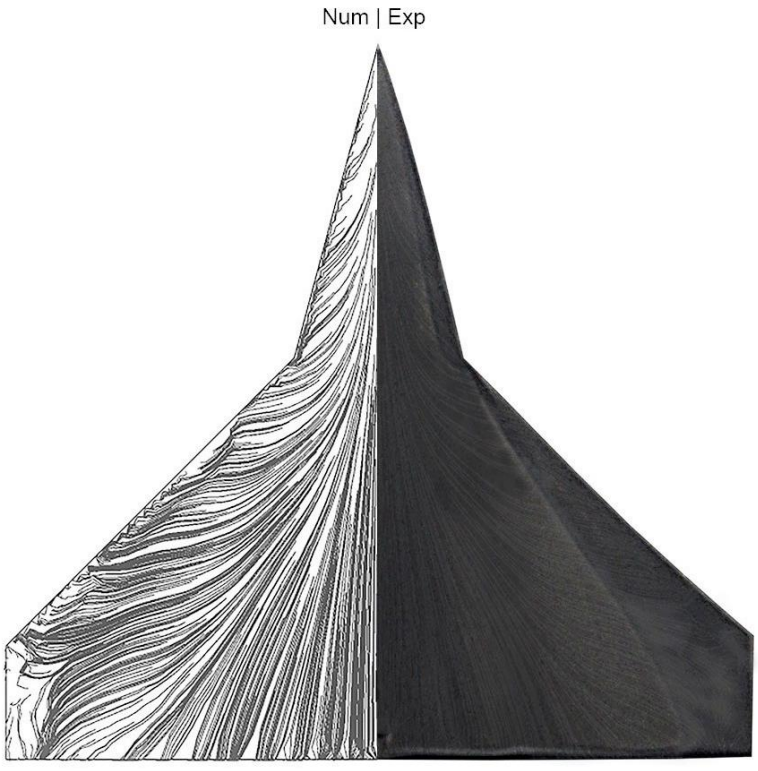

Figure 6.1(b) Oil Flow visualisation at 5º angle of attack

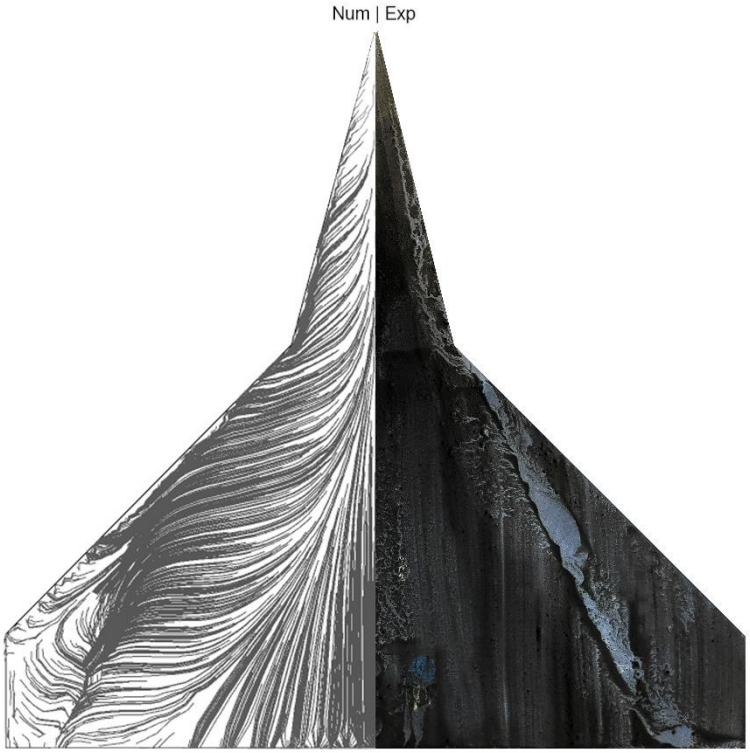

Figure 6.1(c) Oil Flow visualisation at 10º angle of attack

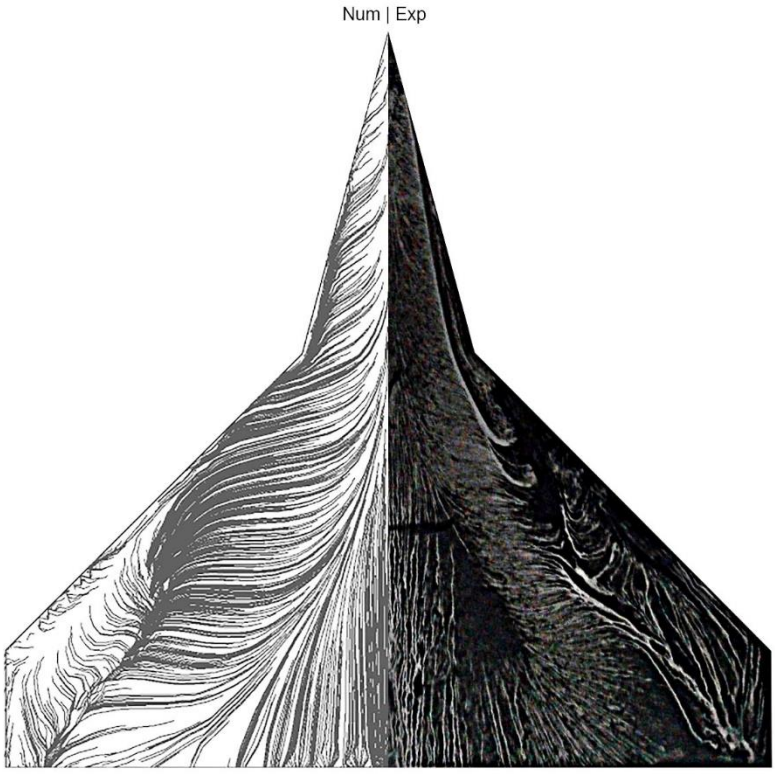

Figure 6.1(d) Oil Flow visualisation at 15º angle of attack

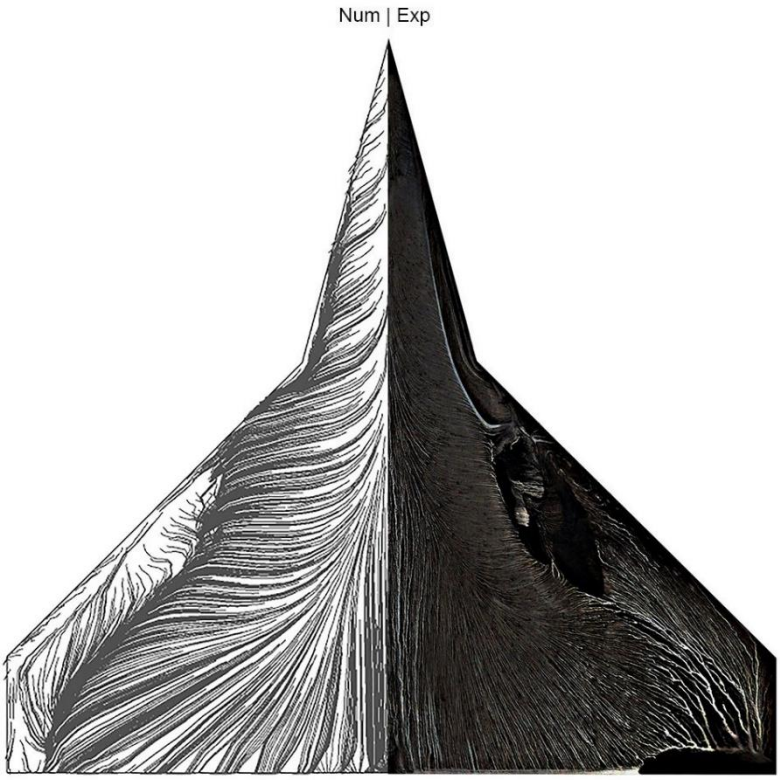

Figure 6.1(e) Oil Flow visualisation at 20º angle of attack

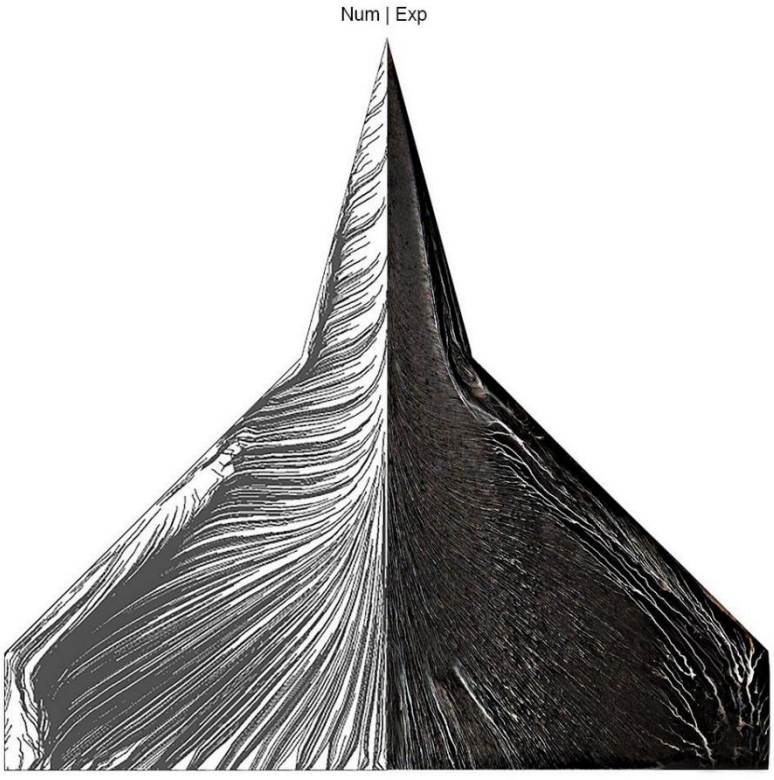

Figure 6.1(f) Oil Flow visualisation at 25º angle of attack

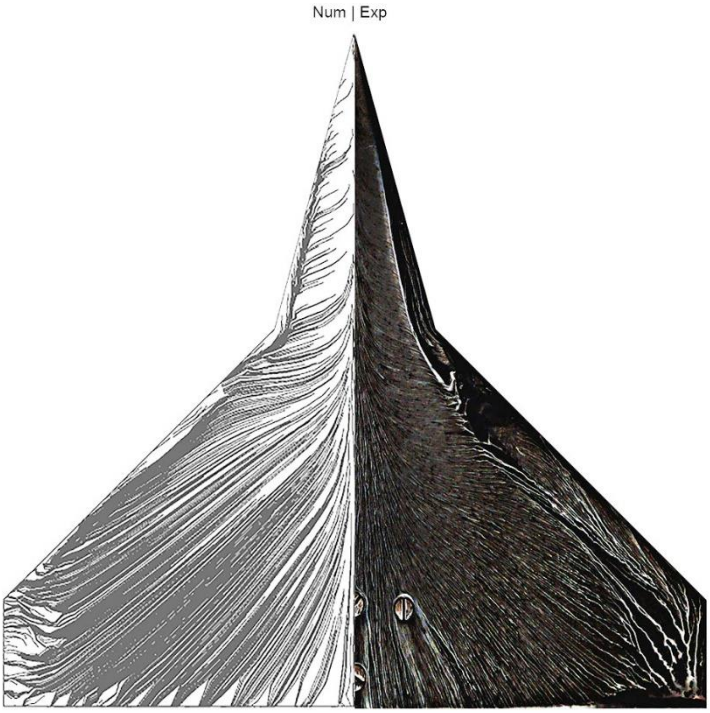

Figure 6.1(g) Oil Flow visualisation at 30º angle of attack

Figure 6.1 Oil Flow Visualisation [Num-Exp]

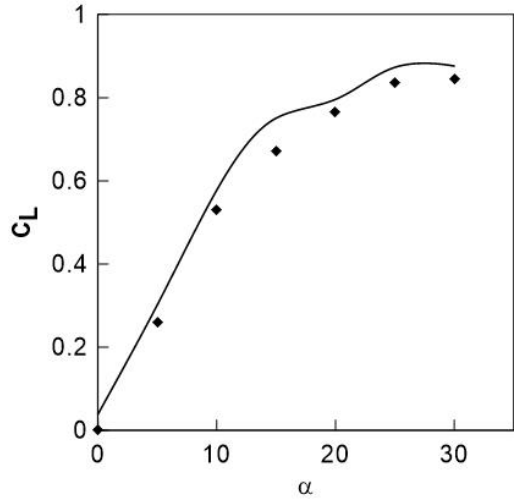

Figure 6.2(a) *V*ariation of lift coefficient with angle of attack

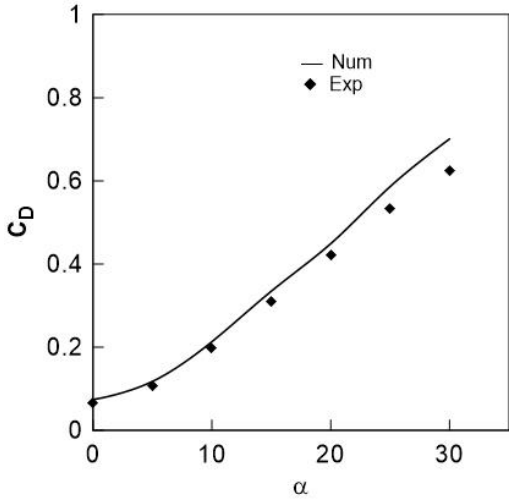

Figure 6.2(b) *V*ariation of drag coefficient with angle of attack

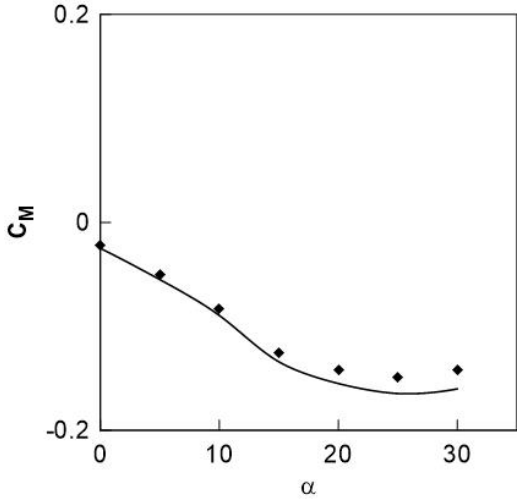

Figure 6.2(c) *V*ariation of moment coefficient with angle of attack

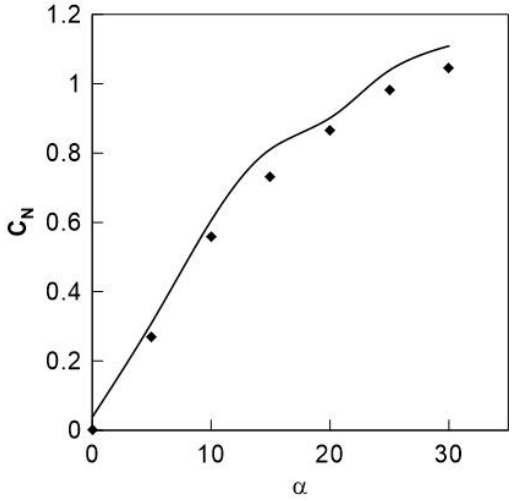

Figure 6.2(d) Variation of normal force coefficient with angle of attack

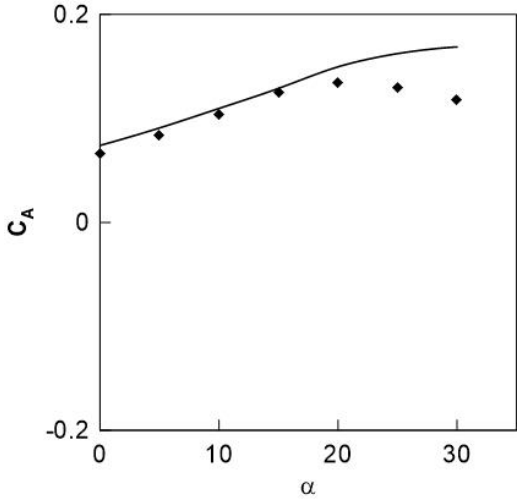

Figure 6.2(e) Variation of axial force coefficient with angle of attack

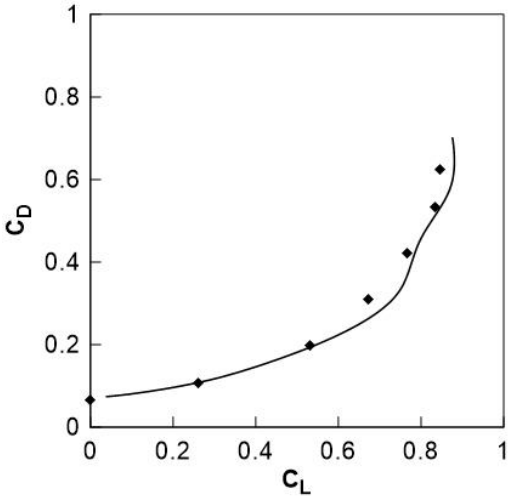

Figure 6.2(f) Variation of lift coefficient with drag coefficient

Figure 6.2 Variations of aerodynamic properties [Num-Exp]

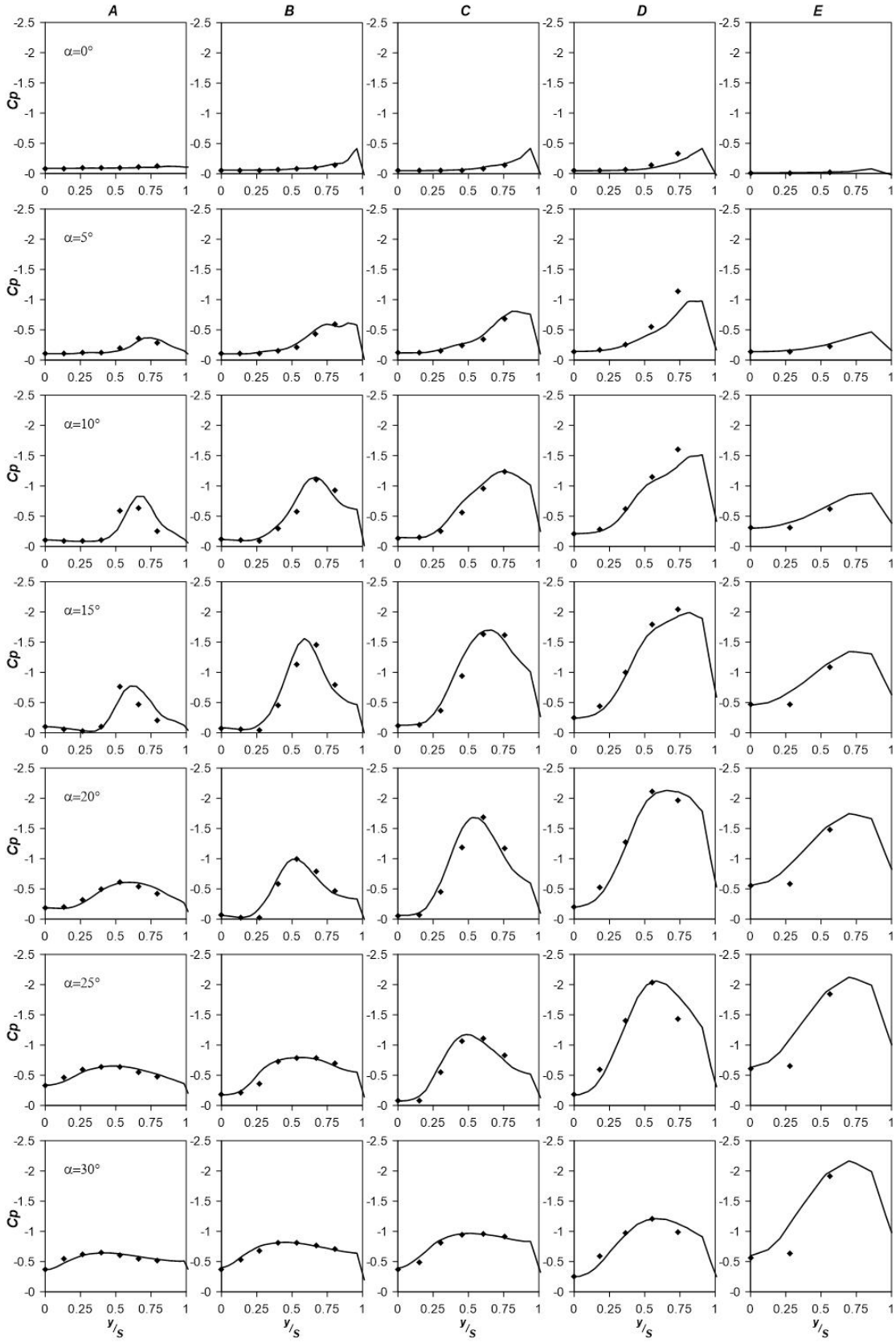

Figure 6.3 Variation of C_p distribution over wing leeward surface. [Num-Exp]

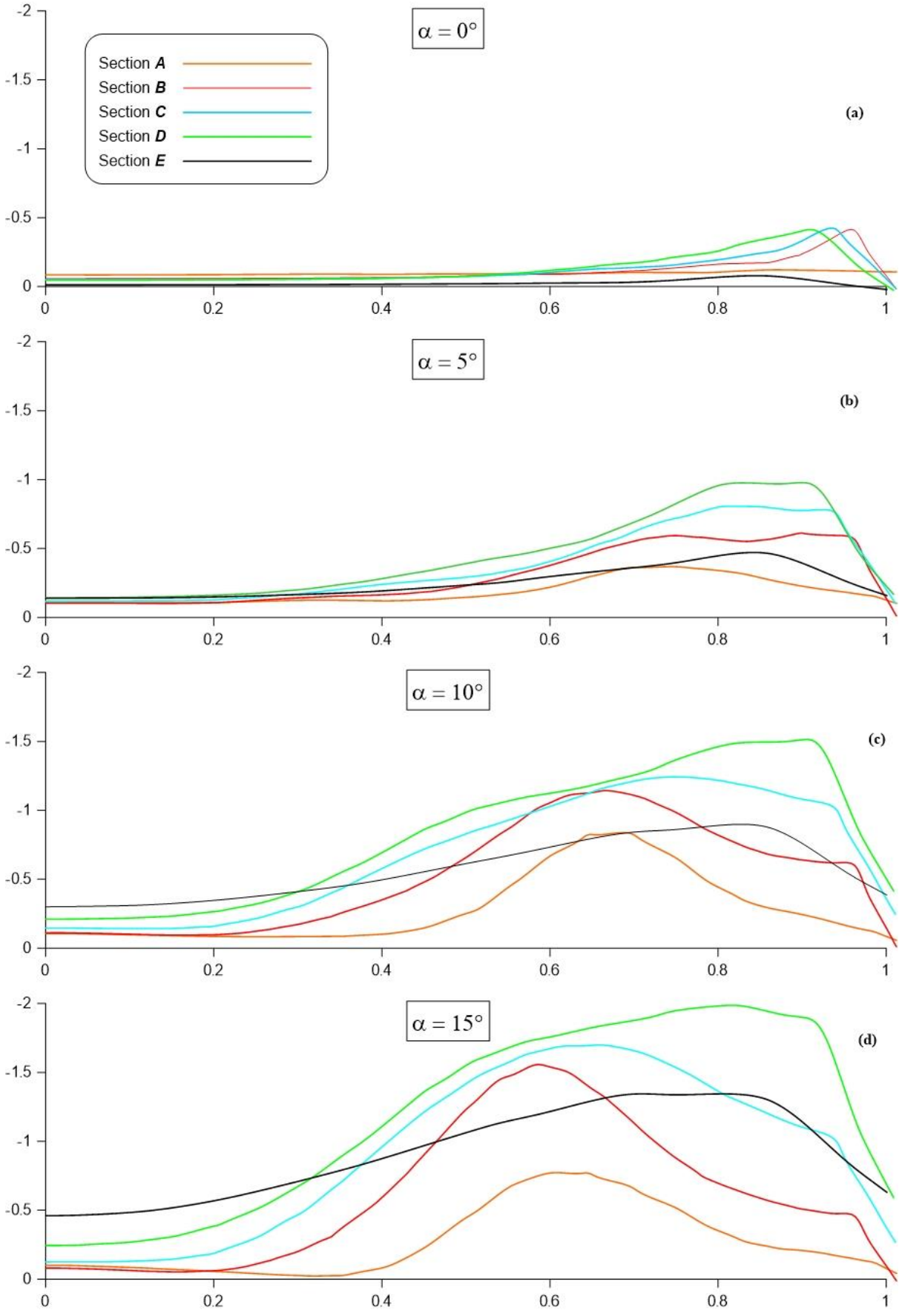

Figure 6.4 Cp distribution half span of model wing, [Numerical] contd…

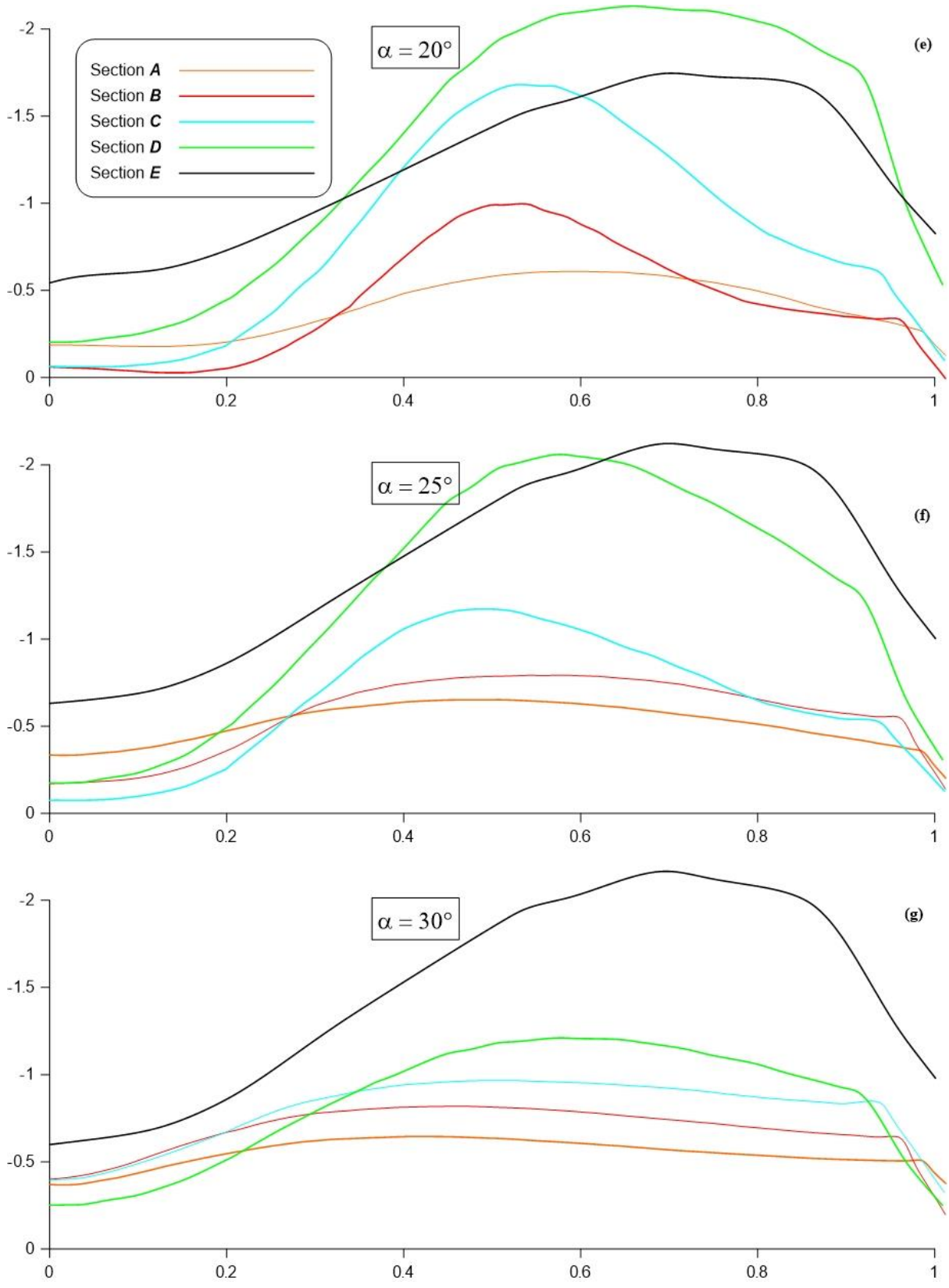

Figure 6.4 C_p distribution half span of model wing at (a) 0° AoA, (b) 5° AoA, (c) 10° AoA, (*d*) 15° AoA, (*e*) 20° AoA, (*f*) 25° AoA, (*g*) 30° AoA, [Numerical]

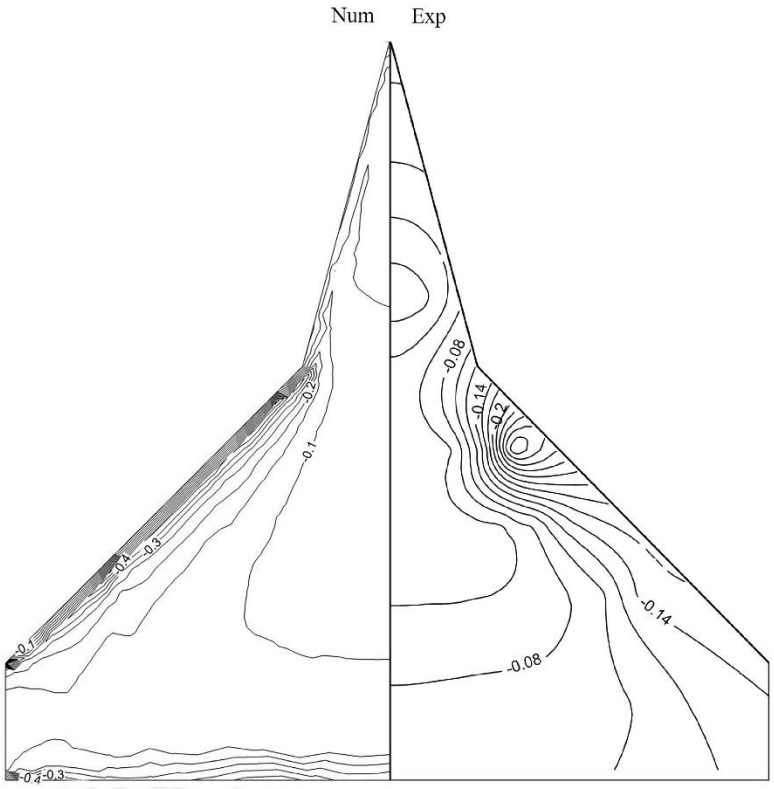

Figure 6.5(a) Contour of Cp over wing leeward surface at 0º angle of attack

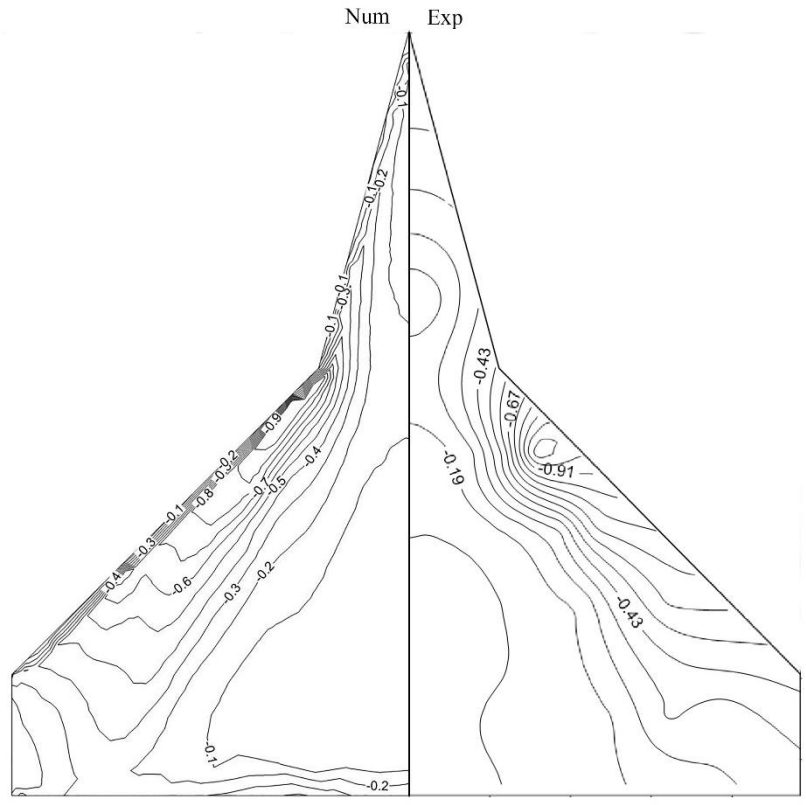

Figure 6.5(b) Contour of Cp over wing leeward surface at 5º angle of attack

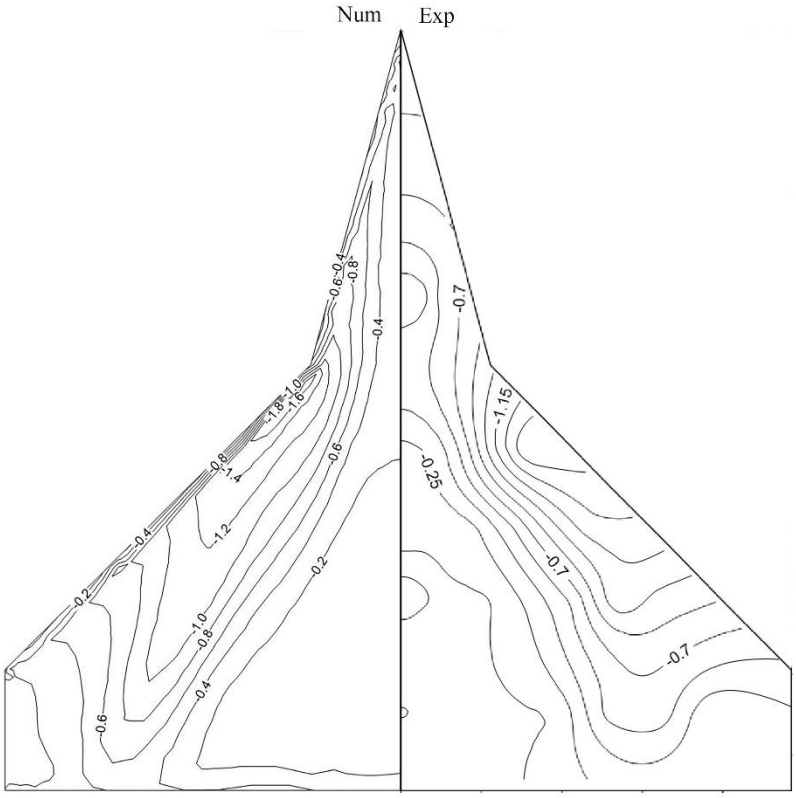

Figure 6.5(c) Contour of Cp over wing leeward surface at 10º angle of attack

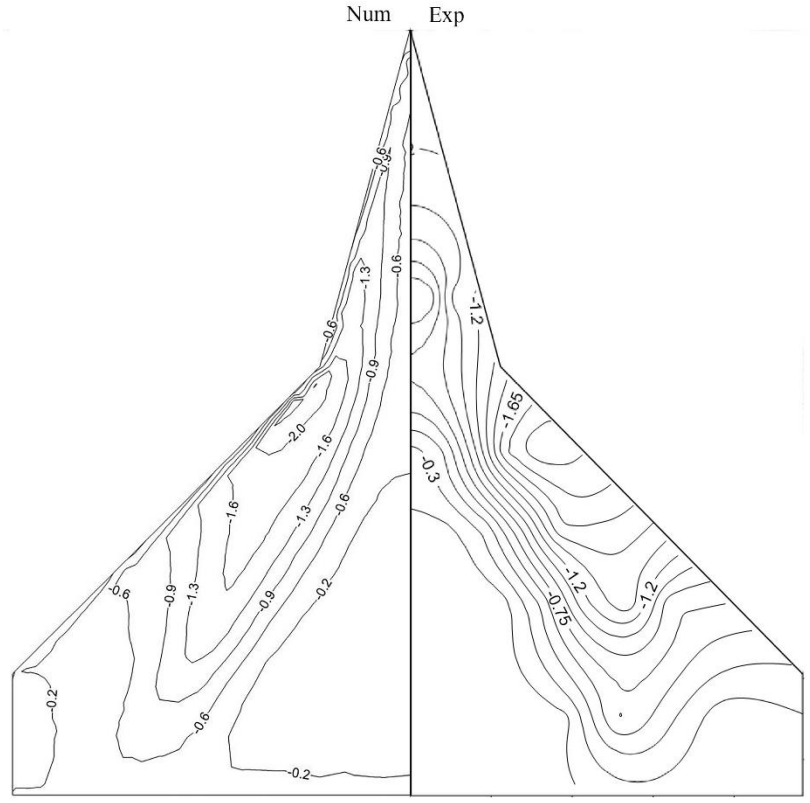

Figure 6.5(d) Contour of Cp over wing leeward surface at 15º angle of attack

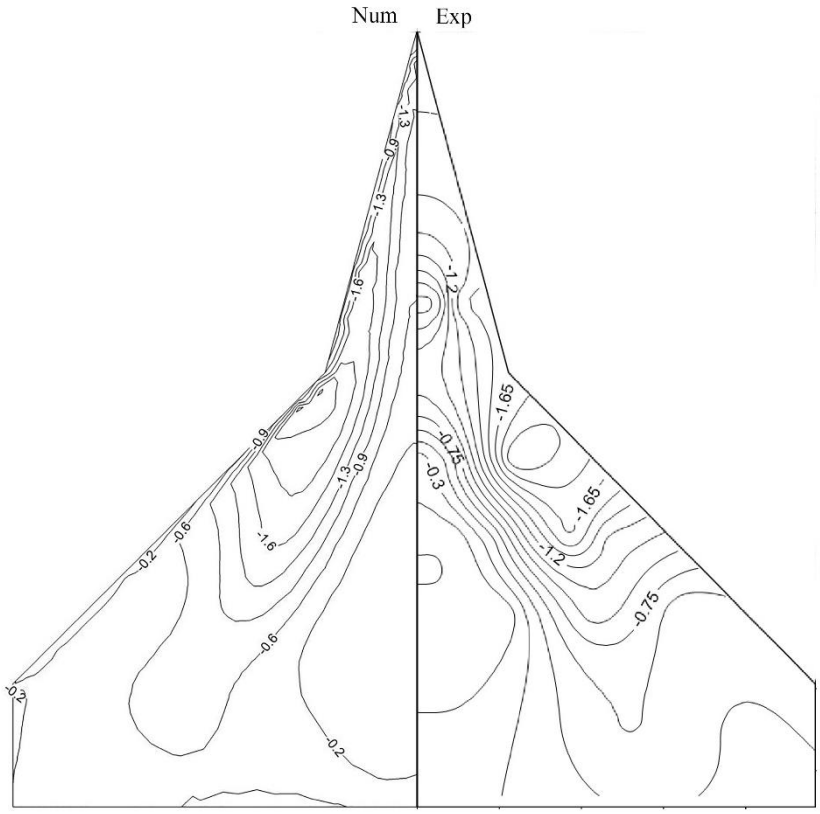

Figure 6.5(e) Contour of Cp over wing leeward surface at 20º angle of attack

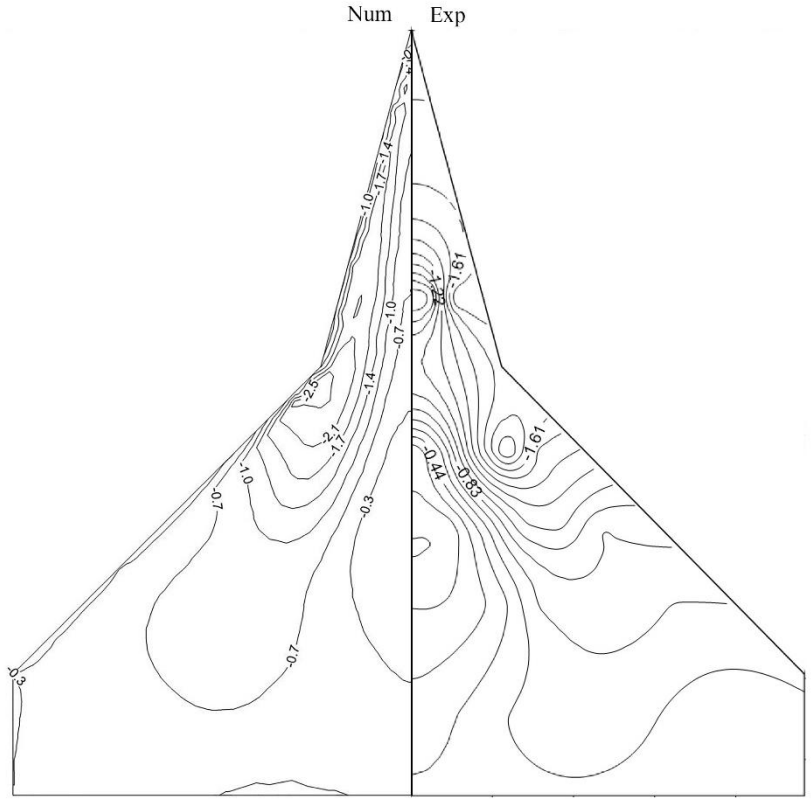

Figure 6.5(f) Contour of Cp over wing leeward surface at 25º angle of attack

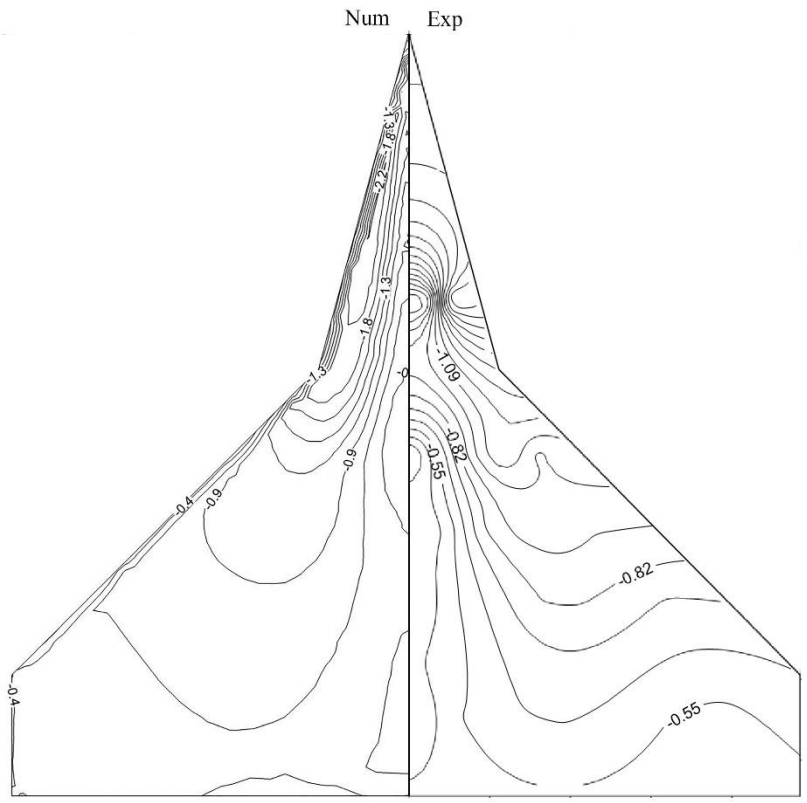

Figure 6.5(g) Contour of Cp over wing leeward surface at 30º angle of attack

Figure 6.5 Contour of Cp over wing leeward surface at (a) 0° AoA, (b) 5° AoA, (c) 10° AoA, (*d*) 15° AoA, (*e*) 20° AoA, (*f*) 25° AoA, (*g*) 30° AoA [Num-Exp]

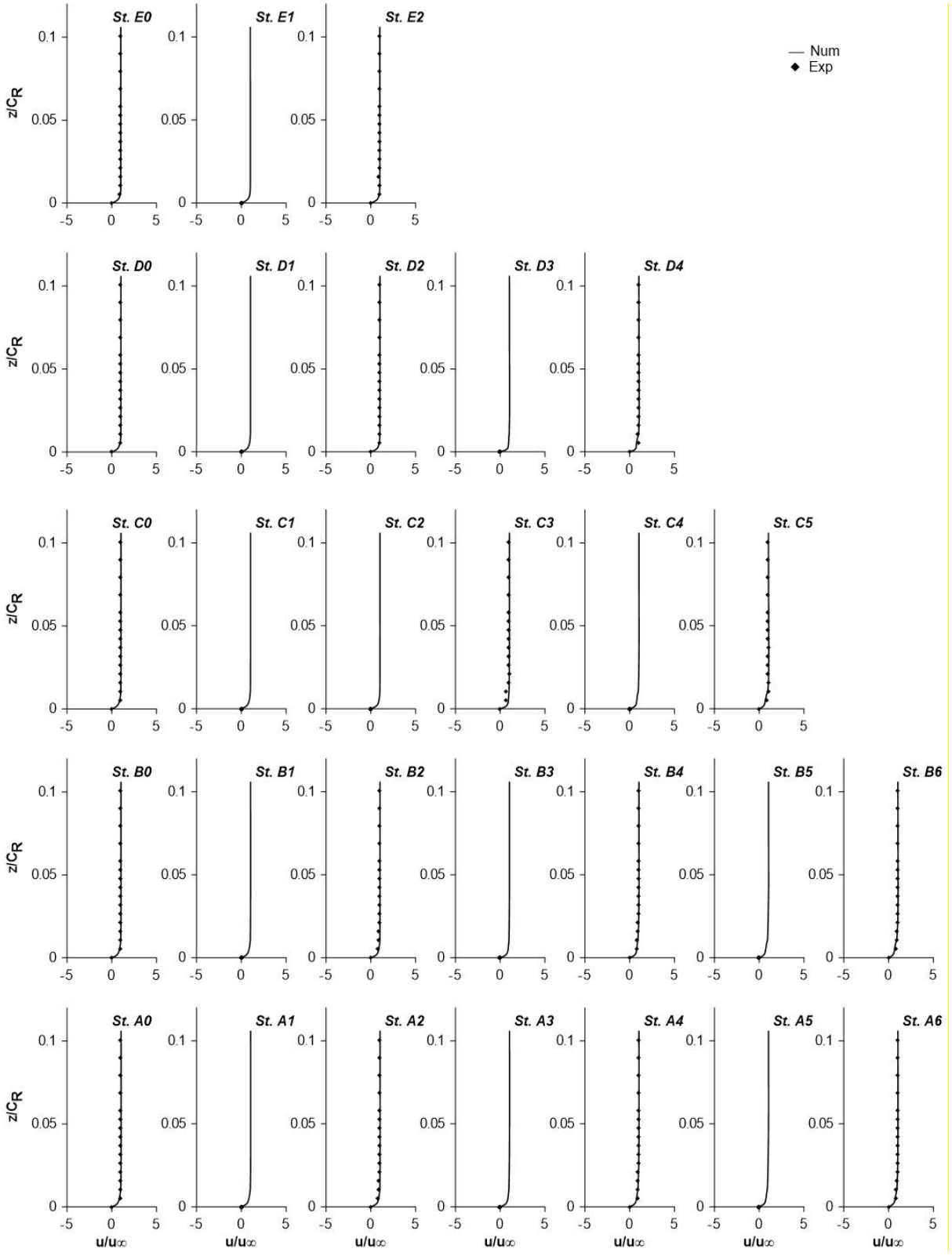

Figure 6.6 Variation of mean velocity at 0º angle of attack [Num-Exp]

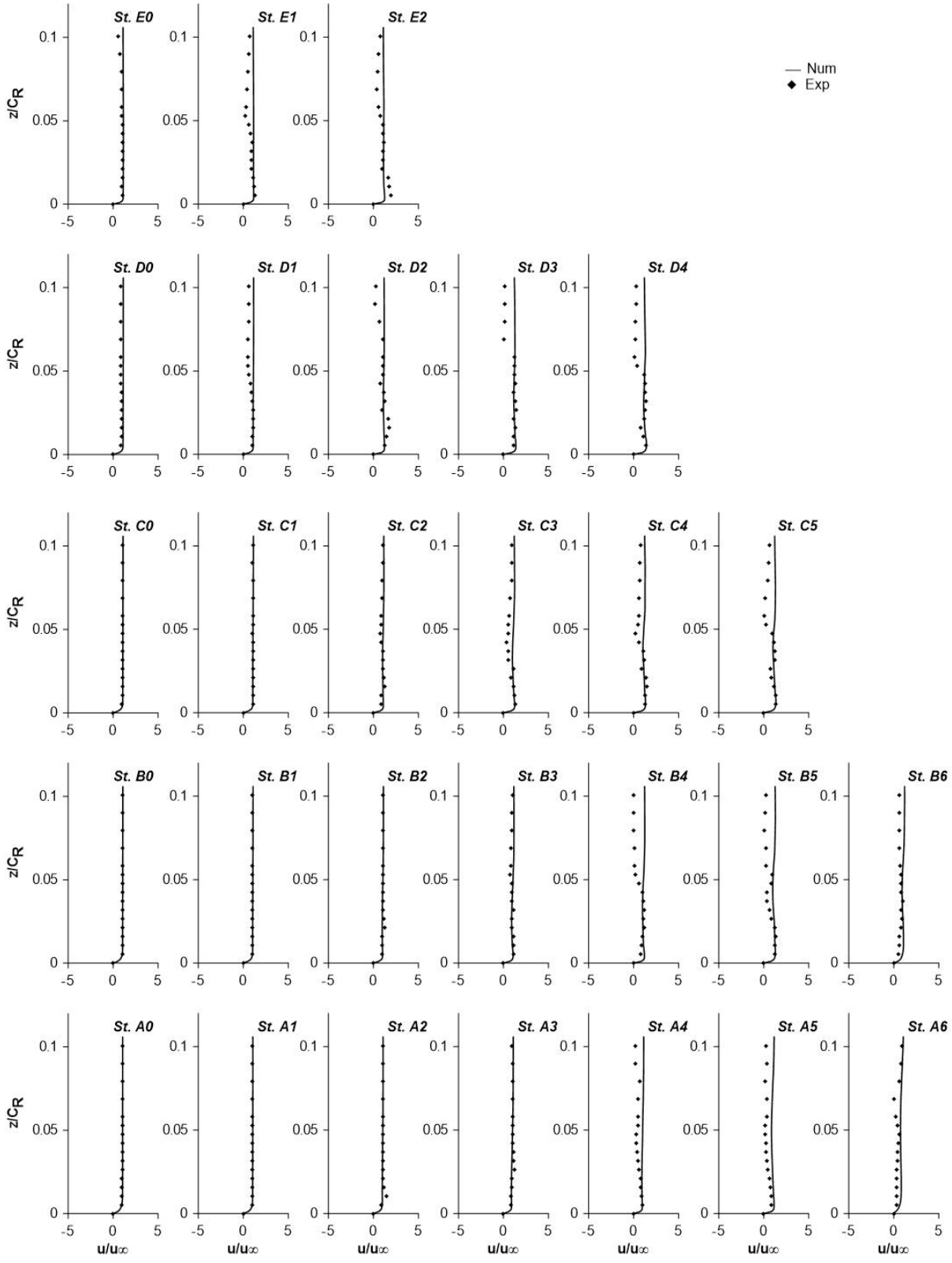

Figure 6.7 Variation of mean velocity at 10º angle of attack, [Num-Exp]

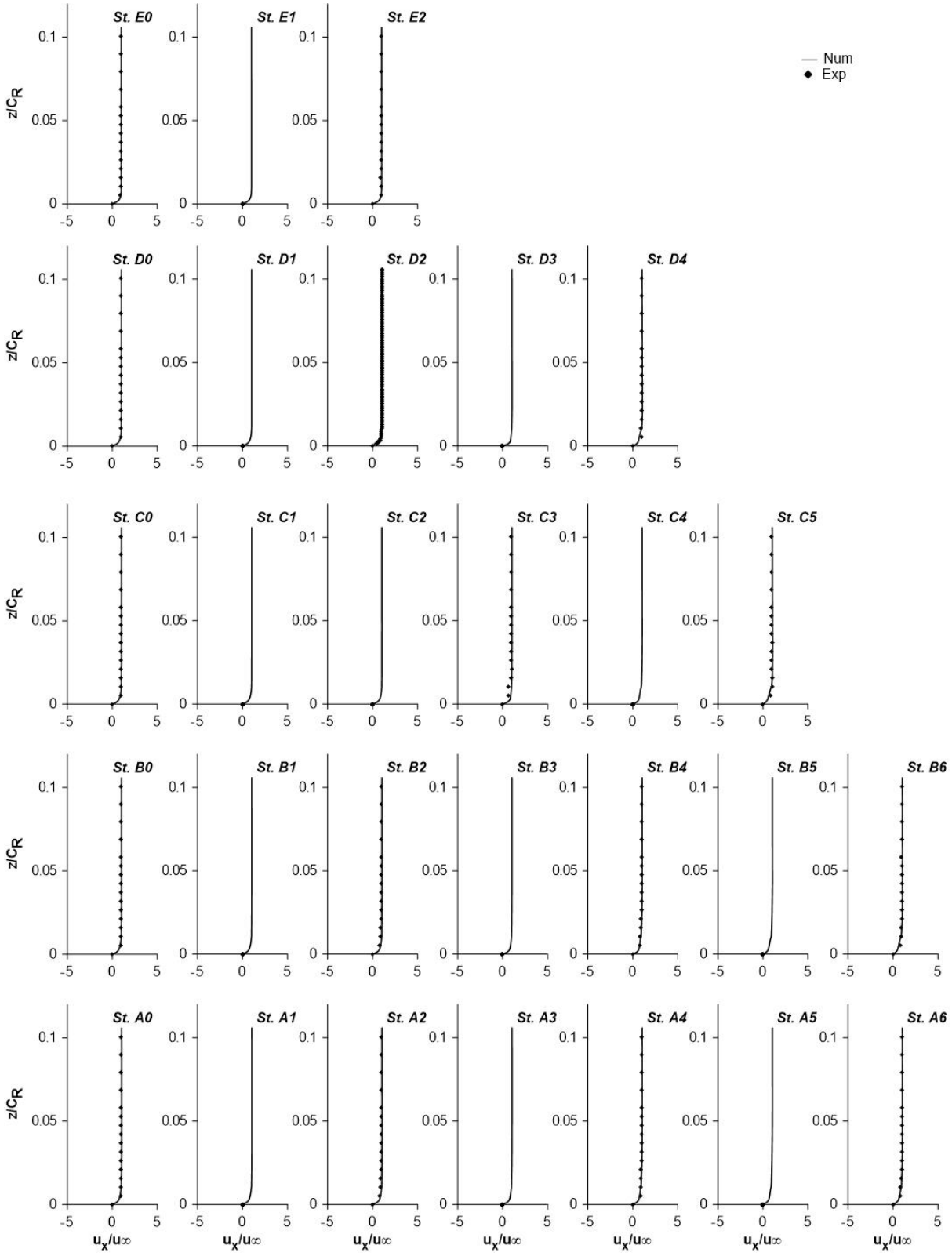

Figure 6.8 Variation of chord wise velocity at 0º angle of attack, [Num-Exp]

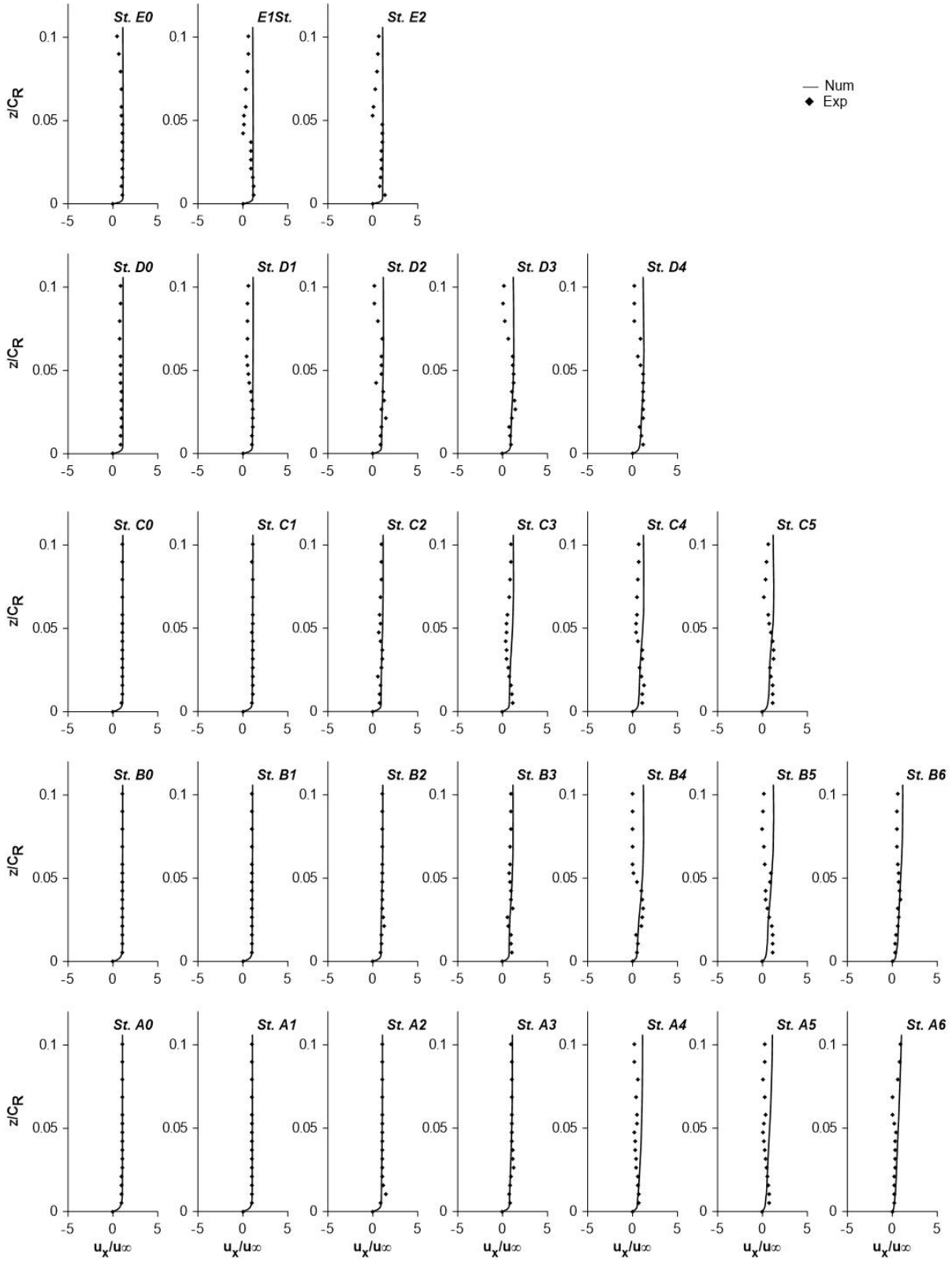

Figure 6.9 Variation of chord wise velocity at 10º angle of attack, [Num-Exp]

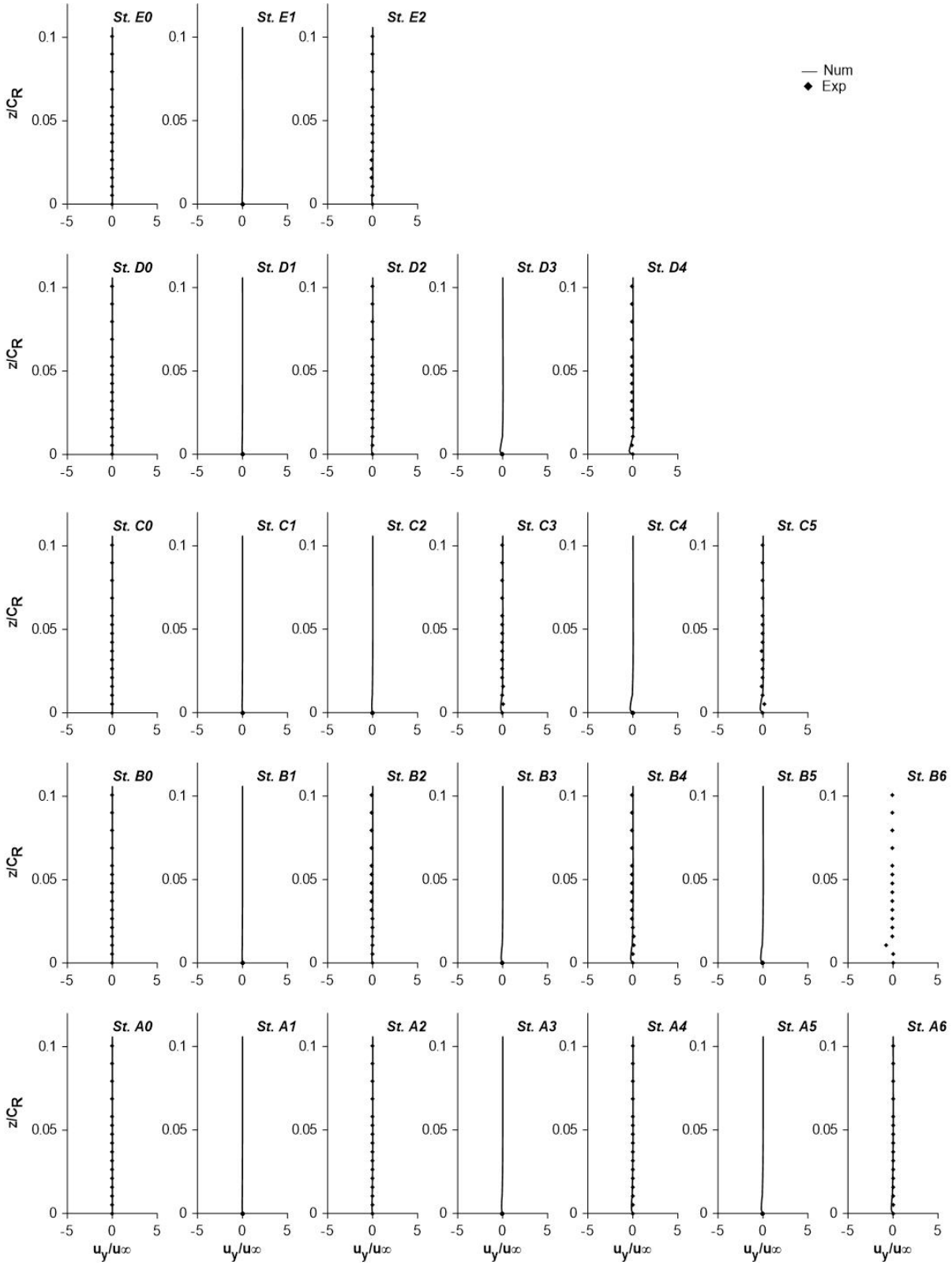

Figure 6.10 Variation of span wise velocity at 0º angle of attack, [Num-Exp]

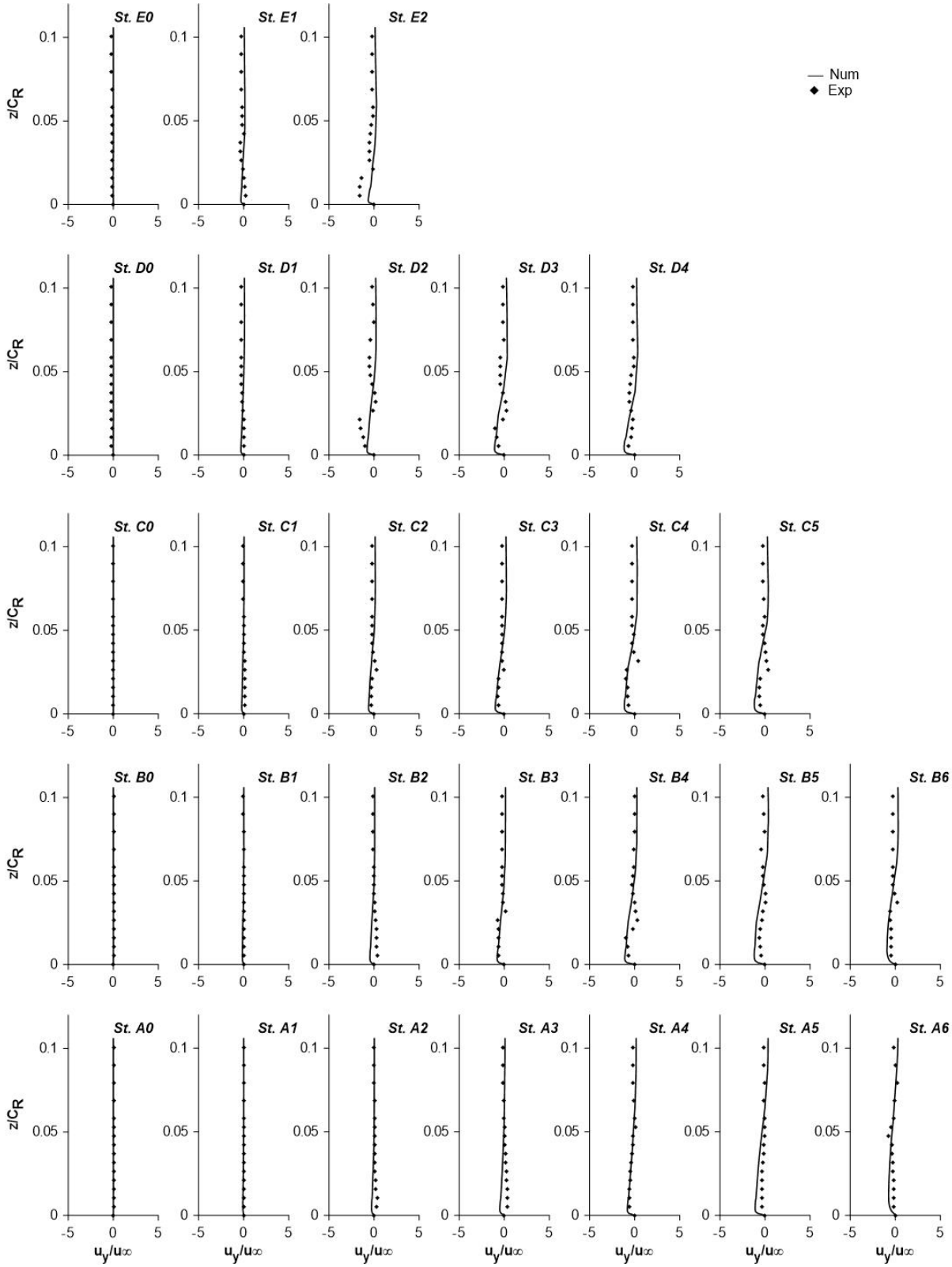

Figure 6.11 Variation of span wise velocity at 10º angle of attack, [Num-Exp]

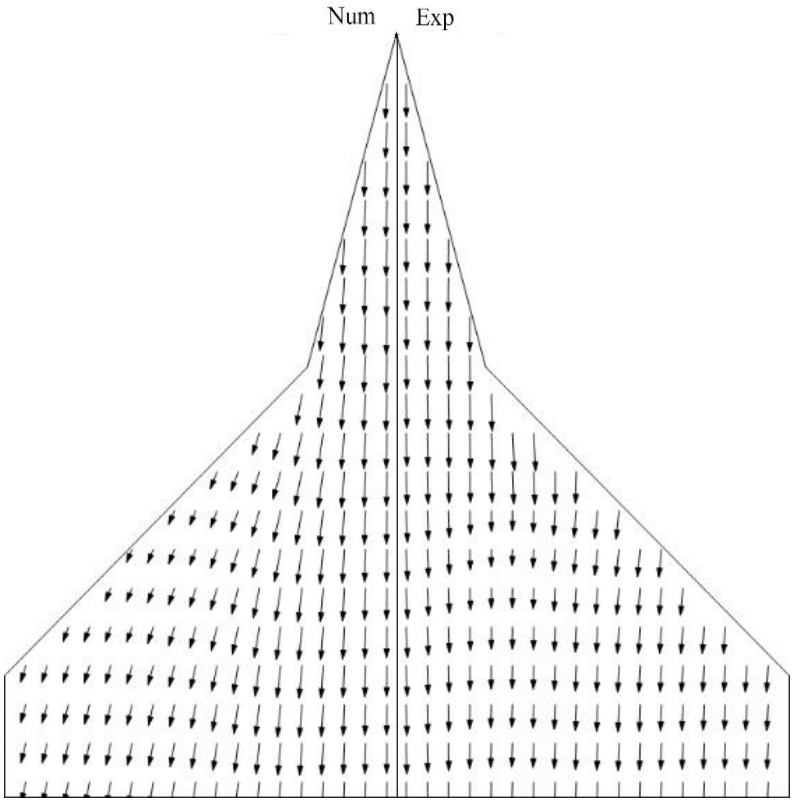

Figure 6.12 2-grid vector plot 1mm above leeward surface at 0 º AoA [Num-Exp]

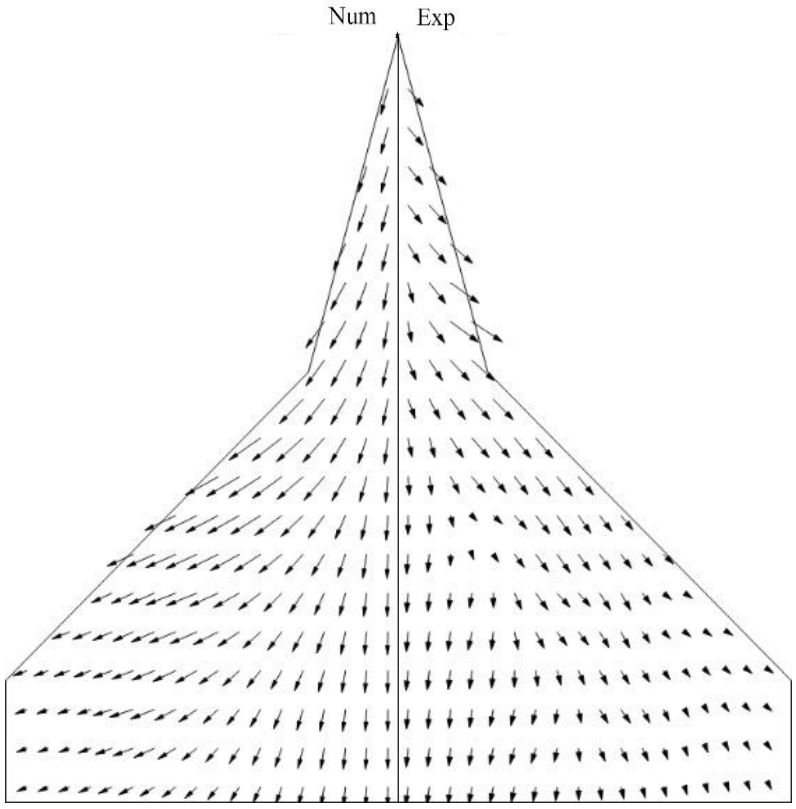

Figure 6.13 2-grid vector plot 1mm above leeward surface at 10 º AoA [Num-Exp]

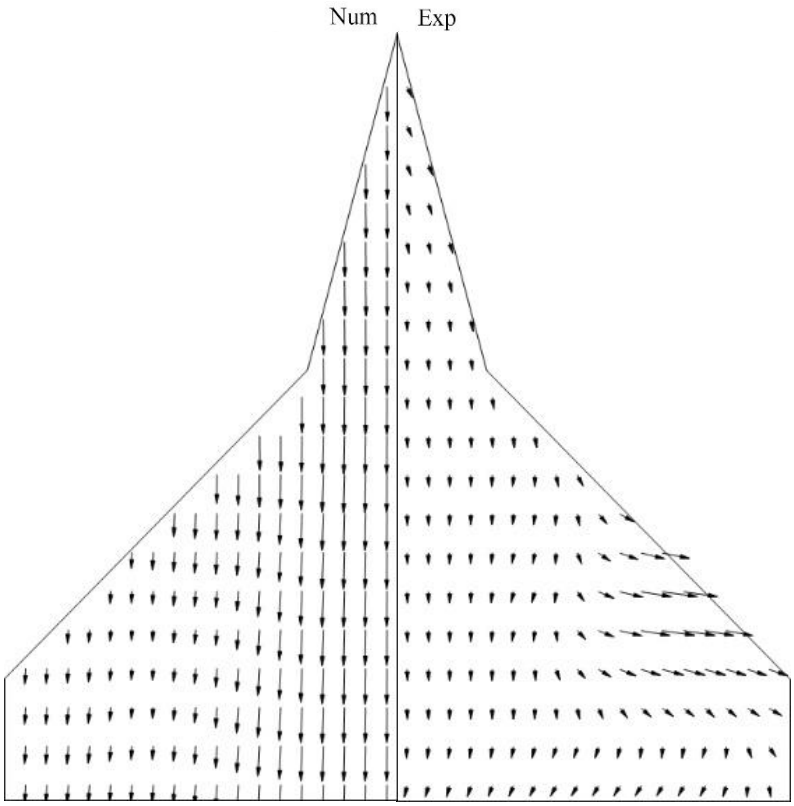

Figure 6.14 2-grid vector plot 2mm above leeward surface at 0º AoA [Num-Exp]

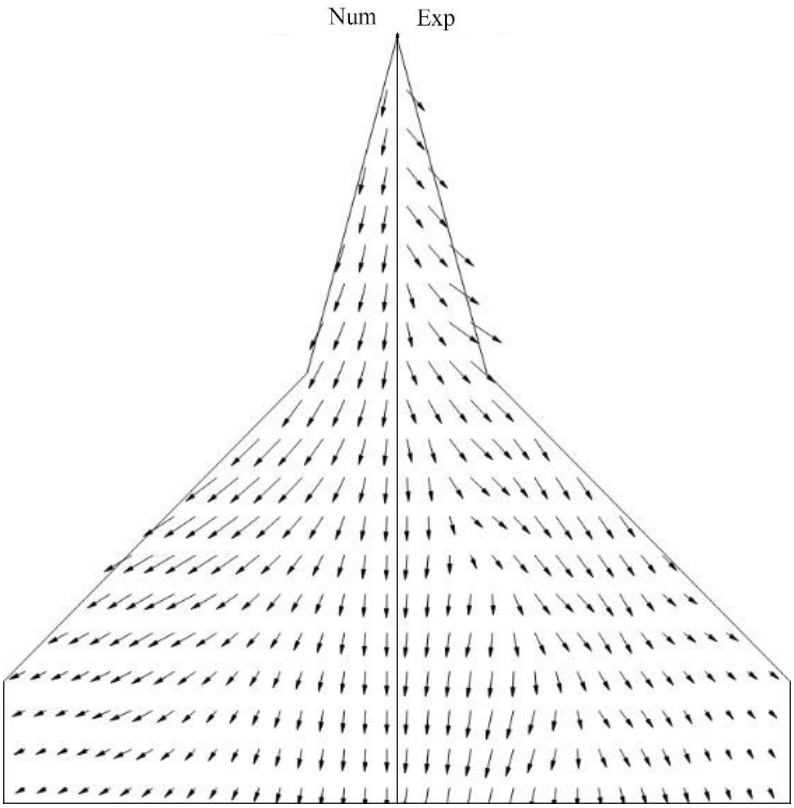

Figure 6.15 2-grid vector plot 2mm above leeward surface at 10º AoA [Num-Exp]

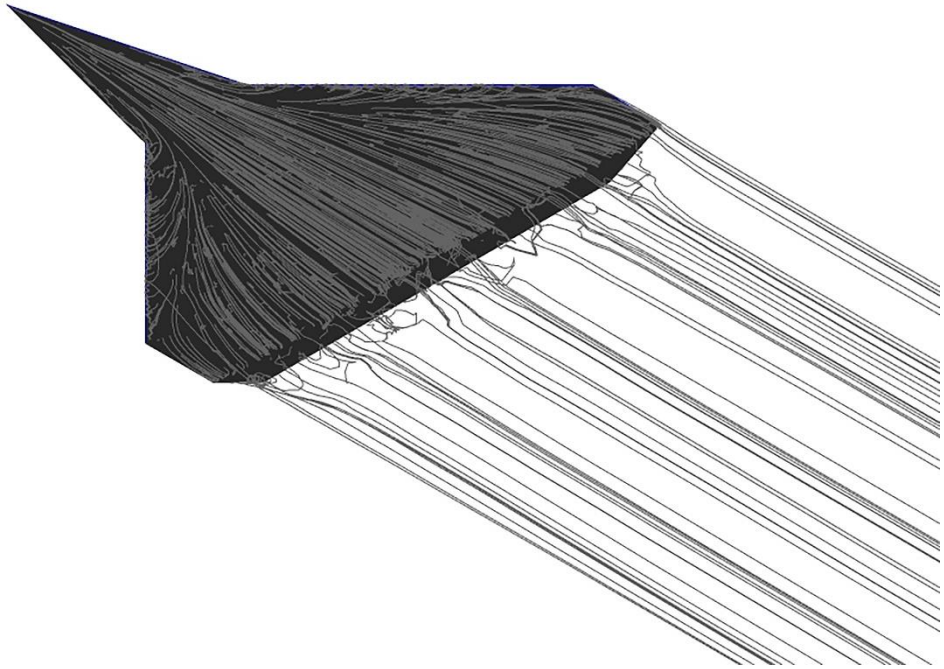

Figure 6.16(a) Pathlines at 0º angle of attack

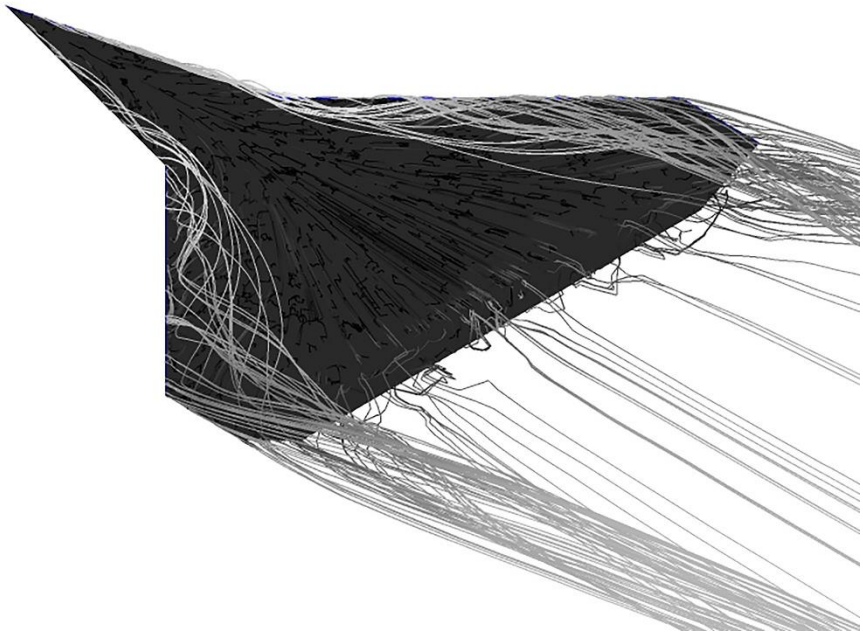

Figure 6.16(b) Pathlines at 5º angle of attack

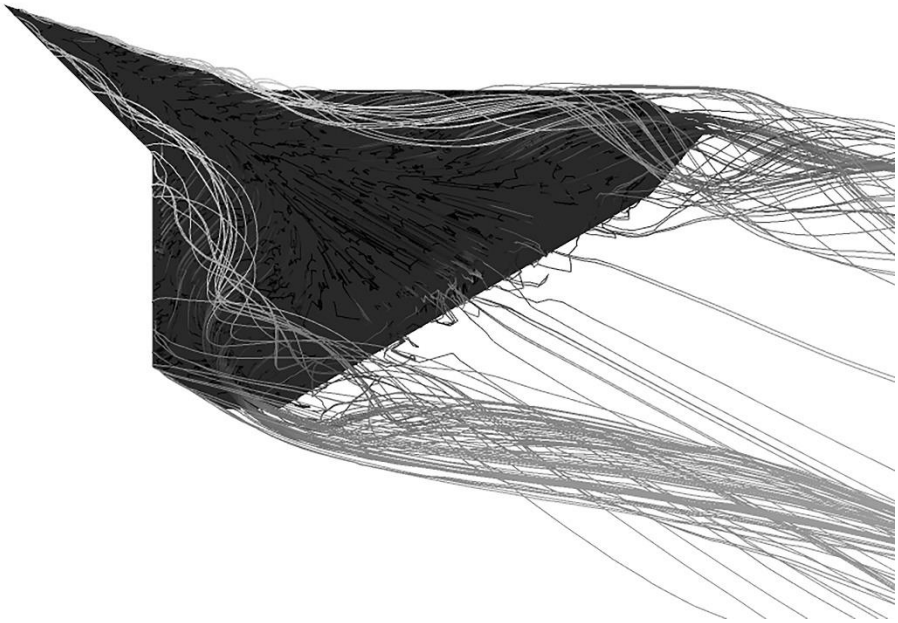

Figure 6.16(c) Pathlines at 10º angle of attack

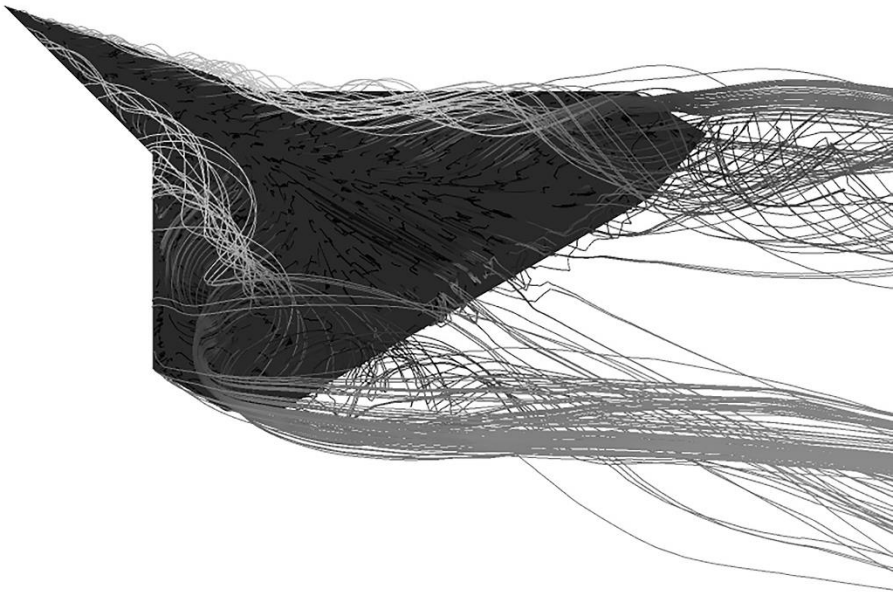

Figure 6.16(d) Pathlines at 15º angle of attack

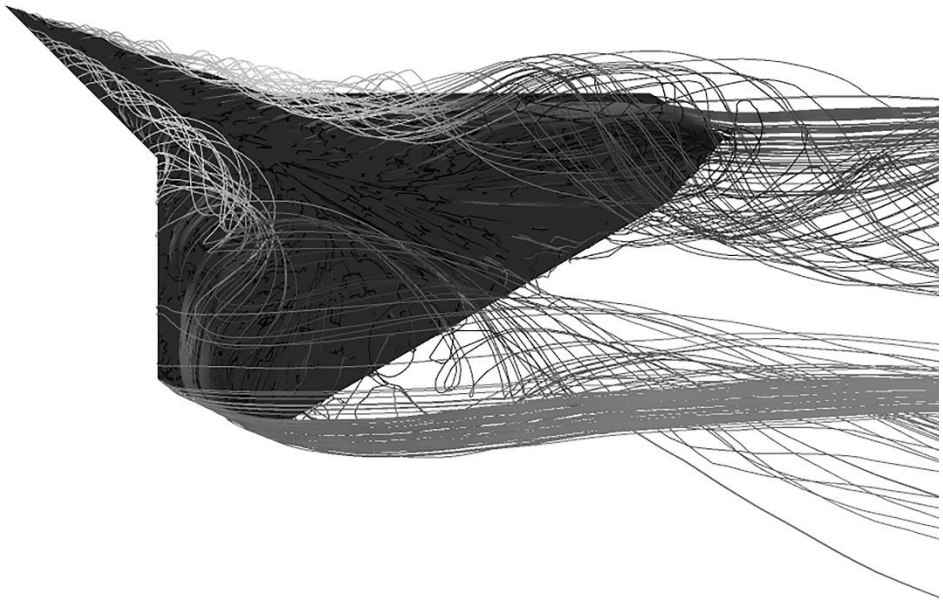

Figure 6.16(e) Pathlines at 20º angle of attack

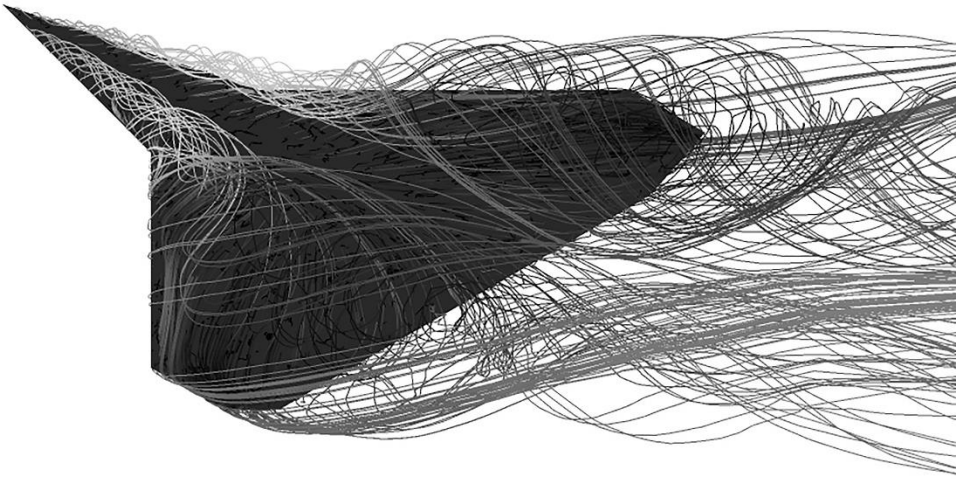

Figure 6.16(f) Pathlines at 25º angle of attack

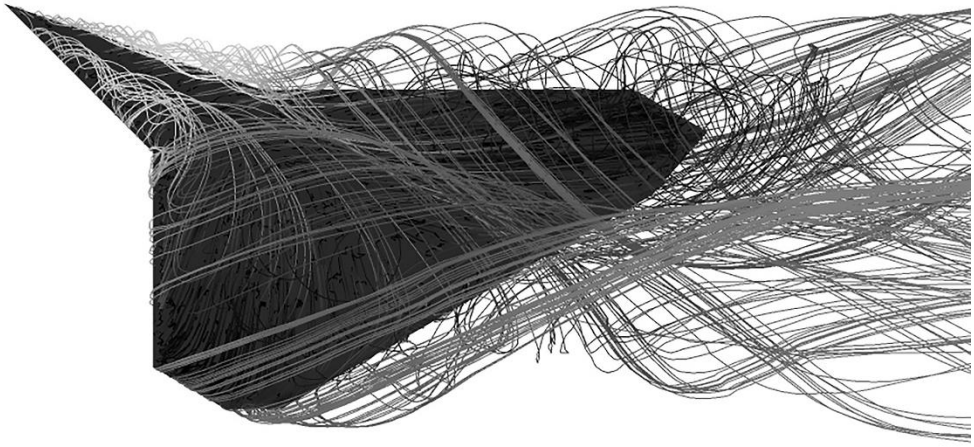

Figure 6.16(f) Pathlines at 25º angle of attack

Figure 6.16 Pathlines at a) 0° AoA, (b) 5° AoA, (c) 10° AoA,

(*d*) 15° AoA, (*e*) 20° AoA, (*f*) 25° AoA, (*g*) 30° AoA [Num-Exp]

CHAPTER 7

Conclusions and Future Work

7.1 Conclusion

In the present study, Flow field investigation of a 75º/45º double delta wing was done experimentally employing different experimental methods as discussed above. The experimental data were analysed and presented in a clear and understandable manner. Three-dimensional numerical simulations of a wing model were also performed under conditions similar to the experiments, utilizing the Spalart-Allmaras turbulence model in ANSYS Fluent (Version 19.1). The predicted results demonstrated reasonable agreement with the experimentally obtained data. Subsequently, the three-dimensional flow field was further visualized by employing the numerical data alongside the experimental counterpart. Characteristics of the flow patterns over the wing surface were also investigated using the experimental and numerically obtained results. Based on the present study, the following conclusions can be drawn.

a. To investigate flow structure closer to the wing leeward surface flow visualization studies were conducted. To obtain an idea about flow direction close to wing leeward surface, Oil flow visualization experiment was done. Oil flow visualization experimentally obtained data were analysed alongside with numerical counterpart obtained data using surface streamlines generated from computational data.

   Formation of different flow structures at different angle of attack over the wing leeward surface were analyzed from oil flow visualization. Among these flow features attached flow, separation and three-dimensional flow etc. were found. It was seen that attached flow occurs at 0° angle of attack. At 5º AoA also, the flow was nearly attached with a hint of formation of strake vortex. Beyond that distinct formation of vortex was observed. At 10° AoA, two distinct vortex namely strake vortex and wing vortex was seen to be formed. From 15° AoA afterwards the vortices starts combining each other and a larger vortex was created.

b. Measurements of surface pressure distribution at various angles of attack were conducted by dividing the entire half wing surface into multiple sections and measuring locations. The results indicate that, consistent with observations from surface flow visualization at 0° angle of attack, a favorable pressure gradient appears to be prevalent across the wing surface, suggesting the presence of attached flow. The results of pressure distribution showed that as AoA increased, C_p decresed in all sections. Also with increase of AoA, the low pressure regions seems to appear increasingly close to inboard section, which may be an indication of merging of two vortices and shifting of the hence created larger vortex inward. The results were arranged to represent in a contour surface plot with iso-pressure lines. This also indicate the creation of increased low pressure zone with higher AoA. Pressure contours derived from experimental data and numerical simulations were analysed and exhibited close similarities with constant pressure iso-lines aligning on the wing surface. The pattern of the contour lines was observed to be consistent with the findings from surface flow visualizations also. It was noted that the computational results qualitatively replicated the experimental observations.

c. To grasp and analyse the influence of the flow structure formations observed through surface flow visualization experiments and surface pressure distribution on the aerodynamic performance of the wing, the aerodynamic forces acting on the wing model are experimentally determined from a 3-component balance experiment. Furthermore, the resulting forces acting on the wing model are also extracted from the numerically simulated results. These numerical and experimental results demonstrate a close agreement with each other and predict qualitatively similar behavior, consistent with other reported findings.

   Experimental data analysis of the lift coefficient curve revealed that C_L increases steadily with a considerable slope up to 15º AoA, after which the slope decreases. But lift was available upto 25º, after which the slope became almost horizontal. So the stall point is located in this vicinity. The drag-polar is also in agreement with the said phenomenon. Numerically solved aerodynamic force coefficients exhibit similar trends and has close resemblance with experimental outcomes.

d. The velocity measurement experiment was conducted over a wing model using a three-hole pressure probe. This experiment was carried out in 0º and 10º AoA. Experimental data was collected at predetermined measurement stations distributed across the half of the wing's leeward surface. The mean absolute velocity, as well as the streamwise and transverse velocity components, were also estimated. Velocity data from numerical simulations were also extracted from the same measurement stations used in the three-hole probe experiment.

   The overall observations from velocity distribution shows that at 0º AoA, as the flow is somewhat an attached flow, the flow over the surface is uniform. At 10º AoA, the flow gets disturbed and a fluctuation is observed. This may be due to the onset of strake and wing vortex. Numerical results also predict fluctuations at some stations.

e. The data, whether from experiments or numerical simulations, shows that the angle of attack significantly impacts the flow characteristics. At different angles, the measured parameters across the wing's leeward surface exhibit varied distributions. Despite this varying diversity, a clear pattern emerges. In general, the parameter curves tend to increase from the stations near the leading edge to those closer to the trailing edge for each section of the wing.
f. The flow pattern over the surface of the wing model has been further explored through numerical analysis of computed pathlines. At a low angle of attack of 0°, the flow remains predominantly attached to the body and generates lift. As the angle of attack increases to 10°, a pair of rolled up flow is seen to be formed from leading edge. From 10º AoA, two vortices were visibly forming from the tip and the leading edge. These vortices get bigger as the angle increases. At 25º AoA, the two vortices seemed to be merged and a bigger vortex generated. This vortex further enlarged at 30º AoA.
g. The computational results demonstrated a generally good alignment with the experimental data, encompassing surface flow visualization, surface pressure coefficient distribution, aerodynamic parameters, and measured velocity distribution using a three-hole pressure probe. These findings were well supported numerically by the Spalart-Allmaras turbulence model. The

differences observed between the computed and experimental results followed a qualitatively similar pattern and were within reasonable limits.

7.2 Scope of Future Work

The reported work aimed to enhance the understanding of the flow field structure around a 75º/45º double delta wing configuration under subsonic flow conditions. A three-dimensional numerical simulation of the wing model was also conducted to scrutinize the inferences formed from the experimental results. Several future research directions were identified:

1. The implementation of Laser Doppler Anemometry (LDA) or Laser Doppler Velocimetry (LDV) could eliminate the intrusive effect of the three-hole pressure probe on the three-dimensional, sensitive flow field. Additionally, the use of 3-dimensional Particle Image Velocimetry (PIV), a non-intrusive method, could provide more accurate, detailed, and reliable information about the flow field, particularly the near-wall regions and the boundary layer generation. Such non-intrusive measurements would help to better understand and improve the estimations about the three-dimensional turbulent flow, which would ultimately enhance the numerical simulation of the wing model.
2. The use of pressure-sensitive paints (PSP) for surface flow visualization and pressure measurement could have helped to understand the pressure distribution over the wing's leeward surface without the need for pressure-tapping holes. This could have avoided unwanted human errors during the fabrication of the pressure tappings and eliminated errors from pressure loss in the PVC tubes and the inaccuracies of the pressure measurement devices. Implementing a more sophisticated pressure measurement technique would improve the experimental results.
3. The implementation of a six-component balance could have provided a better understanding of the roll, pitch, and yaw characteristics, in addition to the lift, drag, and moment measurements. A high-resolution Data Acquisition device will also increase the chance of precision measurement.
4. The three-dimensional numerical simulation of the wing model could have been performed using more computationally intensive techniques, such as Detached Eddy Simulation, Large Eddy Simulation, or Direct Numerical Simulation, along with a more refined mesh structure. This could have

yielded better numerical results with significantly less deviation from the experimental data, although it would have required much more computational power and time.

5. 3-dimensional transient simulation considering different physical constraints of aerodynamic characters could provide more reliable results.
6. Keeping in view the good agreement of results between experiments and numerical simulations, more parametric studies can be carried out to understand the behaviour of such wings in different input conditions.
7. Different geometric models may also be studied, experimentally and numerically, to get a comprehensive view of aerodynamic parameters and flow structure for a better understanding of the behaviour of such wings.

REFERENCES

[1] W. J. Jackman and H. Russel, Flying Machine: Construction and Operation.: CreateSpace Independent Publishing Platform, 2018., Project Gutenberg's online e book, 2008.

[2] O. Lilienthal, Birdflight as the Basis of Aviation: A Contribution Towards a System of Aviation, Compiled from the Results of Numerous Experiments Made by O. Lilienthal, Longmans, Green, 1911.

[3] C. H. Gibbs-Smith, The Invention of the Aeroplane 1799-1909, London: Taplinger Publishing, 1966.

[4] L. Prandtl, "NACA Technical Memorandum No. 452," 1928.

[5] L. Prandtl, "Abstracted as Theory of Lifting Surfaces, Part 1, NACA Technical Note 9, 1920, and Discussed in Applications of Modern Hydrodynamics to Aeronautics, NACA Report 116, 1921.".

[6] M. M. Munk, "NACA Report 121," 1923.

[7] R. E. Gordnier, M. R. Visbal and D. Garmann, "High-Fidelity Computations for Flexible Micro Air Vehicle Applications," in *DoD High Performance Computing Modernization Program Users Group Conference*, Schaumburg, 2010.

[8] S. Zafar and M. Gadalla, "Design and Evaluation of a Rooftop Wind Turbine Rotor With Untwisted Blades," in *Proceedings of the ASME 2013 Power Conference*, Boston, 2013.

[9] G. H. Elkaim, "Autonomous Surface Vehicle Free-Rotating Wingsail Section Design and Configuration Analysis," *Journal of Aircraft*, vol. 45, no. 6, pp. 1835-1852, 2008.

[10] R. Wootton, "Dragonfly flight: morphology, performance and behaviour," *International Journal of Odonatology*, vol. 23, no. 1, pp. 31-39, 2020.

[11] T. J. Mueller and J. D. DeLaurier, "Aerodynamics of Small Vehicles," *Annuak Review of Fluid Mechanics*, vol. 35, pp. 89-111, 2003.

[12] "Internet Sources, https://www.the-blueprints.com/blueprints/modernplanes/modern-aa-an/20021/view/aerospatiale-bac_concorde_1/".

[13] I. H. Abbot and A. E. Von Doenhoff, Theory of Wing Sections, including a summery of airfoil data, Courier Corporation, 1959.

[14] E. C. Polhamus, "A concept of the vortex lift of shape-edge delta wings based on a leading edge suction analogy," *NASA Technnical note*, December 1966.

[15] F.-H. LI, "Static and dynamic visualisation studies of two double delta wing models at high angles of attack," *Naval Post Graduate School, California*, March 1992.

[16] R. M. Wood, J. E. Byrd and G. F. Wesselmann, "Influence of airfoil geometry on delta wing leading edge vortices and vortex induced aerodynamics at supersonic speed," *NASA Technical Paper 3105,* March 1992.

[17] N. G. Verhaagen, L. N. Jenkins, S. B. Kern and A. E. Washburn, "A study of Vortex flow over 76/40 double delta wing," February 1995.

[18] S. K. Hebber, M. Platzer and A. Abdu, "Experimental investigation of vortex flow control using juncture fillets on a cropped double-delta wing".*33rd Aerospace Sciences Meeting and Exhibit.*

[19] C. Klein and R. H. Engler, "Visualization of Aerodynamic Effects on a Double-delta Wing Aircraft Model using Pressure Sensitive Paint (PSP) Technique," *Klein, C., and Engler, R. H. (1999). Visualization of aerodynamic effects on Journal of Visualization, Vol 2(1),* p. 9–16, March 1999.

[20] A. Pashilkar, "Surface pressure model for simple delta wings at high angles of attack," *Sadhana Vol. 26(6),* pp. 495-515, June 2001.

[21] H. A. Gonzalez, J. H. Bell, B. G. McLachlan and G. E. Ericson, Effects of Various Fillet Shapes on a 76/40 Double Delta Wing from Mach 0.18 to 0.7, Naval air warfare center aircraft Division patuxent river, 1994.

[22] M.-H. Sohn and Y.-I. Jang, "Visualization and Flowfield Measurements of the Vortical Flow over a Double-Delta Wing," *International Journal of Aeronautical and Space Sciences,* vol. 4, no. 1, pp. 63-74, 2003.

[23] S. L. Gai, M. Roberts, A. Barker, C. Kleczaj and A. J. Riley, "Vortex interaction and breakdown over double-delta wings," *The Aeronautical Journal,* vol. 108, pp. 27-34, 2004.

[24] Y.-K. Lee and H.-D. Kim, "Vortical flows over a LEX-delta wing at high angles of attack," *KSME International Journal,* vol. 18, pp. 2273-2283, 2004.

[25] G. E. Erickson and H. A. Gonzalez, "Pressure-Sensitive Paint Investigation of Double-Delta Wing Vortex Flow Manipulation," Nevada, 2005.

[26] M. H. Sohn and J. W. Chang, "Effect of a centerbody on the vortex flow of a double-delta wing with leading edge extension," *Aerospace Science and Technology,* vol. 14, no. 1, pp. 11-18, 2010.

[27] B. Nath, J. K. Prasad and S. Das, "Flow field study on a 65deg. Blunted delta wing," in *National Conference on Wind Tunnel Testing (NCWT-02)*, Bangalore, 2009.

[28] G. Atashbaz and M. Ommian, "Experimental Investigation of Vortex Flow over an 80º/60ºDouble Delta Wing at Sideslip," *Journal of Aircraft,* vol. 43, no. 3, pp. 840-843, 2006.

[29] M. Gopinath and K. M. Parammasivam, "Pressure Measurements on Delta wing with different leading edge radii," in *Fourth International Symposium on Computational Wind Engineering (CWE 2006)*, Yokohama, 2006.

[30] C. Nettelbeck, "Dynamic Analysis of a Double Delta Wing in Free Roll.," 2009.

[31] A. Z. Al Gharni, F. Saeed and A. M. Al Gharni, "Experimental and Numerical Investigation of 65º Degree Delta and 65º / 40º Degree Double-Delta Wings," *Journal of Aircraft,* vol. 45, no. 1, pp. 71-76, 2008.

[32] S. Saha and B. Majumdar, "Modeling and Simulation on Double Delta Wing," *International Journal of Advanced Computer Research,* vol. 3, no. 8, pp. 201-205, 2013.

[33] F. Saeed, "Experimental and Numerical Study of Side-Slipping 65º Delta and Double-Delta Wings," *International Journal of Engineering and Advanced Technology,* vol. 4, no. 2, pp. 214-221, 2014.

[34] M. Naimuddin, G. Sharma and G. Chopra, "Experimental and Computational Study on Compound Delta Wing," *Journal of Basic and Applied Engineering Research,* vol. 1, no. 3, pp. 47-52, 2014.

[35] J. A. Ekaterinaris and L. B. Schiff, "Navier-Stokes Solutions for an Oscillating Double-Delta Wing," *Journal of Aircraft,* vol. 32, no. 2, pp. 228-234, 1995.

[36] B. Aswin Kumar, P. Kumar, S. Das and J. K. Prasad, "Effect of leading edge shapes on 81°/45° double-delta wing at low speeds," *Journal of Aerospace Engineering,* pp. 1-8, 2017.

[37] S. L. Gai, M. Roberts, A. Barker, C. Kleczaj and A. J. Riley, "Vortex interaction and breakdown over double-delta wings," *The Aeronotical Journal,* vol. 108, no. 1079, pp. 27-34, 2004.

[38] F. Renac, D. Barberis and P. Molton, "Renac, F., Barberis, D., and Molton, P. (2005). Control of Vortical Flow over a Rounded Leading-Edge Delta Wing. AIAA Journal, 43(7), 1409–1418. doi:10.2514/1.7265," *AIAA Journal,* vol. 43, no. 7, pp. 1409-1418, 2005.

[39] N. M. Chaderjian and L. B. Schiff, "Large-Amplitude, High-Rate Roll Oscillations of A 65º Delta Wing at High Incidence," *Ames Research Center, NASA,* pp. 407-414, 2000.

[40] J. Wang and J. Tu, "Effect of wing planform on leading-edge vortex structures. , 55(2), 120–123. doi:10.1007/s11434-009-0643-z," *Chinese Science Bulletin,* vol. 55, no. 2, pp. 120-123, 2010.

[41] P. Kaurinkoski and T. Siikonen, "Calculation of Transonic Laminar and Turbulent Flow Past a Delta Wing," Helsinki University of Technology Laboratory of Aerodynamics, Finland, 1992.

[42] J. Sreenivasulu, S. Das, P. Kumar and J. K. Prasad, "Investigation of Flow Field over a Blunt Double Delta Wing," in *36thNational Conference on Fluid Mechanics and Fluid Power,* Pune, 2009.

[43] B. Muller and A. Rizzi, "Müller, B., and Rizzi, A. (1989). Navier-Stokes computation of transonic vortices over a round leading edge delta wing. International Journal for Numerical Methods in Fluids, 9(8), 943–962. doi:10.1002/fld.1650090805," *International Journal for Numerical Methods in Fluids,,* vol. 9, pp. 943-962, 1989.

[44] C. H. Hsu and C. H. Liu, "Navier-Stokes computation of flow around a round-edged double-delta wing," *AIAA Journal*, vol. 28, no. 6, p. 961–968, 1990.

[45] M. R. Allan, K. J. Badcock, G. N. Barakos and B. E. Richards, "A CFD Investigation of Wind Tunnel Interference Effects on Delta Wing Aerodynamics," University of Glasgow, 2002.

[46] J. M. Luckring, "Reynolds Number Compressibility and Leading Edge Bluntness Effect on Delta Wing Aerodynamics," in *24th International Congress of the Aeronautical Sciences*, 2004.

[47] M. K. Singh, V. Ramesh and S. M. Deshpande, "Mesh less Euler Computation for Cropped Delta Wing with Aileron Deflection," in *11th Annual CFD Symposium*, 2009.

[48] H. E. Hamidi and M. Rahimi, "Numerical Investigation of high attack angle flow on 76º/45º Double-Delta wing in Incompressible Flow," *International Journal of Aerospace and Mechanical Engineering*, vol. 5, no. 4, pp. 854-857, 2011.

[49] J. Liu, H. Sun, Z. Liu and Z. Xiao, "Numerical investigation of unsteady vortex breakdown past 80°/65° double-delta wing.27(3), 521–530. doi:10.1016/j.cja.2014.04.018," *Chinese Journal of Aeronautics*, vol. 27, no. 3, pp. 521-530, 2014.

[50] L. C. Squire, "Experimental work on the aerodynamics of integrated slender wings for supersonic flight," *Progress in Aerospace Sciences*, vol. 20, pp. 1-96, 1981.

[51] J. M. Luckring, "The discovery and prediction of vortex flow aerodynamics," *The Aeronautical Journal*, vol. 123, no. 1264, pp. 729-804, 2019.

[52] J. Miau, K. T. Kuo, W. H. Liu, S. J. Hsieh, J. H. Chou and C. K. Lin, "Flow developments above 50-deg sweep delta wings with different leading-edge profiles," *Journal of Aircraft,*, vol. 32, no. 4, pp. 787-794, 1995.

[53] C. Chowdhury, "Modeling and Calibration of Pressure Probes," Kolkata, 2007.

[54] D. W. Bryer and R. C. Pankhurst, Pressure-probe Methods for Determining Wind Speed and Flow Direction, Londan: Stationery Office Books, 1971.

[55] B. Majumdar, Fluid Mechanics with Laboratory Manual, 2nd ed., Delhi: PHI Learning Private Limited, 2016.

[56] I. Gursul, R. Gordnier and M. Visbal, "Unsteady aerodynamics of nonslender delta wings," *Progress in Aerospace Sciences*, vol. 41, no. 7, pp. 515-557, 2005.

[57] S. J. Kline and F. A. McClintock, "Describing Uncertainty in Single Sample Experiments," *Mechanical Engineering*, 1953.

[58] P. Ansell, M. Bragg and M. Kerho, "Ansell, P., Bragg, M., and Kerho, M. (2010). Envelope Protection System Using Flap Hinge Moment Measurements," in *28th AIAA Applied Aerodynamics Conference*, 2010.

[59] J. M. Diebold, M. C. Monastero and M. B. Bragg, "Aerodynamics of a Swept Wing with Ice accretion at at Low Reynolds," 2012.

[60] R. J. Moffat, "Using Uncertainty Analysis in the Planning of an Experiment," *Journal of Fluids Engineering*, vol. 107, no. 2, pp. 173-178, 1985.

[61] B. C. Nakra and K. K. Chaudhry, Instrumentation Measurements and Analysis, New Delhi: Tata McGraw Hill Education Private Limited.

[62] "V-19.1, Ansys Fluent Manual".

[63] J. Yuvaprakash, P. Kumar and j. k. Prasad, "Experimental and numerical studies on double delta wing with sharp leading edge at subsonic speed," *International Research Journal of Multidisciplinary Science and Technology*, vol. 1, no. 3, 2016.

[64] B. Nath, S. Das and J. K. Prasad, "Flowfield study on a 65 degree blunted delta wing," in *National Conference on Wind Tunnel Testing*, Bangalore, 2009.

[65] D. Liu, Y. Wang, D. Chen, X. Xu and X. Peng, "Numerical Investigation on the Reynolds Number Effects of Supercritical Airfoil," *International Conference on Advances in Computational Modeling and Simulation*, vol. 31, pp. 103-109, 2012.

[66] P. R. Spalart and S. R. Allmaras, "A One Equation Turbulence Model for Aerodynamic Flows," *La Recherche Aerpspatiale*, vol. 1, pp. 5-24, 1994.

[67] M. Lee and C. M. Ho, "Lift Force of Delta Wing," *Applied Mechanics Reviews*, pp. 209-221, 1990.

[68] U. Brennenstuhl and D. Hummel, "Vortex Formation Over Double-Delta Wing," *Institut für Strömungsmechanik, Federal Republic of Germany*, 1982.

APPENDIX – A

Effectiveness and Appropriateness of Turbulence Models: Spalart-Allmaras (SA), k-Epsilon, and k-Omega SST

Turbulence modeling is essential in Computational Fluid Dynamics (CFD) for precisely forecasting flow behavior across many engineering applications. The choice of a turbulence model is contingent upon the particular flow conditions, geometry, and required precision. The often-employed models are the Spalart-Allmaras (SA) model, the k-Epsilon model, and the k-Omega Shear Stress Transport (SST) model. Each model possesses unique attributes, benefits, and constraints, rendering them appropriate for particular applications.

1. Spalart-Allmaras Model

The Spalart-Allmaras model is a one-equation turbulence model tailored for aeronautical applications. It resolves a singular transport equation for an altered turbulent viscosity.

Attributes:

- **Simplicity:** It is computationally efficient as it employs a singular transport equation, rendering it appropriate for high-velocity aerodynamic flows.
- **Targeted Application:** The model is especially proficient for boundary layer flows exhibiting modest separation and compressible flows at elevated Reynolds numbers.
- **Linear Eddy Viscosity:** It posits a linear correlation between turbulent stress and strain rate, hence constraining its precision in flows characterized by significant separation or recirculation.

Benefits:

- Economically efficient, it is suitable for extensive simulations when computational expenses are a priority.
- Exhibits strong performance for connected flows and slender boundary layers in exterior aerodynamics.
- Dependable in high-velocity compressible flows, such as those occurring over airfoils or wings.

Constraints:

- Restricted precision for flows characterized by intense adverse pressure gradients, considerable separation, or vortex-dominated dynamics.
- Less effective in intricate three-dimensional flows or transitional states.

Applicability: The SA model is optimally utilized in aerospace contexts, particularly for exterior flows surrounding wings, fuselages, or airfoils, where the boundary layer remains predominantly attached, and flow separation is negligible.

2. k-Epsilon (k-ε) Model

The k-Epsilon model is a two-equation turbulence model that resolves transport equations for turbulent kinetic energy (k) and its dissipation rate (ε).

Attributes:

- **Robustness:** It is extensively utilized across several industries owing to its durability and ease of application.

- **Emphasis on Free-Shear Flows:** The model has strong performance in free-shear flows, including jets, wakes, and boundary layers, with minimal separation.
- **Incompressibility:** This method is especially efficient for incompressible flows at modest Reynolds values.

Benefits:

- Demonstrated dependability for totally turbulent flows with negligible separation.
- Appropriate for industrial applications, including HVAC systems, pipe flows, and exterior flows over blunt bodies.
- Provides adequate precision for steady-state, isotropic turbulence.

Constraints:

- Challenges with precision inflows are characterized by pronounced adverse pressure gradients, considerable separation, or recirculation.
- Less successful in forecasting near-wall flows due to its reliance on wall functions.
- Exhibits suboptimal performance in transitional flows or flows characterized by anisotropic turbulence.

The k-Epsilon model is most appropriate for free-shear flows and common industrial applications that demand simplicity, robustness, and precision. It is frequently employed as a reference model for comparison in CFD analyses.

3. k-Omega SST (Shear Stress Transport) Model

The k-Omega SST model integrates the benefits of the k-Omega model in proximity to walls with the k-Epsilon model in free-stream conditions. It is a two-equation model that resolves transport equations for turbulent kinetic energy (k) and specific dissipation rate (ω).

Attributes:

- **Model Integration:** It shifts from k-Omega in the near-wall region to k-Epsilon in the distant field, enhancing precision across various flow regimes.
- **Effective Management of unfavorable Pressure Gradients:** It exhibits superior performance in flows characterized by unfavorable pressure gradients and considerable separation.
- **Wall Resolving Capabilities:** The k-Omega SST model possesses wall-resolving capabilities, eliminating the need for wall functions and hence enhancing accuracy in proximity to walls compared to the k-Epsilon model.

Benefits:

- Precise for flows exhibiting separation, unfavorable pressure gradients, and intricate geometries.
- Enhanced forecasting of flow characteristics in external aerodynamics and transitional flows.
- Effectively resolves near-wall flows without dependence on empirical wall functions.

Constraints:

- More computationally intensive than the Spalart-Allmaras and k-Epsilon models.

- Responsive to free-stream turbulence levels, which may impact accuracy in some applications.
- May exhibit inferior performance in free-shear flows compared to the k-Epsilon model.

The k-Omega SST model is exceptionally adaptable and appropriate for complex flow applications, including those over airfoils, wings, or turbomachinery components. Its capacity to manage significant adverse pressure gradients renders it a favored option for aerodynamic and hydrodynamic research.

In conclusion, the choice of a turbulence model must be determined by the particular flow conditions and the objectives of the simulation. The **Spalart-Allmaras model** is suitable for high-speed aerodynamic flows with associated boundary layers, whereas the **k-Epsilon model** is effective for free-shear flows in industrial contexts. The **k-Omega SST** model provides a versatile and precise solution for complicated flows, including those with separation, due to its capability to resolve near-wall flows and manage adverse pressure gradients. Nonetheless, its elevated computational expense may not always be warranted in less complex applications. Optimal results necessitate meticulous consideration of flow physics and processing resources.

In this present study Spallart-Almaras turbulent model was adopted after carefully considering model independent study and references from lituratures as discussed in Section 4.3 of Chapter 4, Numerical Technique and Procedure.

1. Balasubramanian, R., Barrows, S. T., & Chen, J. (2008). Investigation of Shear-Stress Transport Turbulence Model for Turbomachinery Applications. In 45th AIAA Aerospace Sciences Meeting and Exhibit. https://doi.org/10.2514/6.2008-566
2. Nof, E., Bhardwaj, S., Koullapis, P., Bessler, R., Kassinos, S. C., & Sznitman, J. (2023). In vitro–in silico correlation of three-dimensional turbulent flows in an idealized mouth-throat model. In PLoS Computational Biology (Vol. 19, Issue 3). International Society for Computational Biology. https://doi.org/10.1371/journal.pcbi.1010537
3. Ansys Manual retrieved on 10.01.2025 from www.ansys.com, Release 2019R2

APPENDIX – B

Detailed Step by Step procedure of Recording of Experimental Results

This research investigates the flow phenomenon and pressure distribution over and above a double delta wing by employing various experimental techniques, including wind tunnel testing, oil flow visualization, balance measurement, surface pressure distribution measurements, and velocity profile assessments using a multi-hole pressure probe.

The following step by step procedures may be taken to acquire and record the experimental data so that the results can be achieved smoothly.

- A wind tunnel having low turbulence intensity and with sufficiently spacious test section be selected. The test section should be such that the blockage due to model should be less (<6%).
- The surface of the model wing should be smooth to allow the flowing air pass smoothly.
- Required equipment and instruments be selected as per experimental goal. For present study a wing traversing system, a three-component balance, a three-hole probe, chemicals, pressure transmitter were selected.

Oil flow visualization

- Titanium di-oxide (TiO_2), kerosene and oleic acid ($C_{18}H_{34}O_2$) were utilized as pigment, solvent and additive for the present study.
- By trial and error an appropriate mixture was prepared for present test condition.
- The oil solution was gently applied to the leeward surface of the wing after carefully removing all residue oil or dirt from previous observation.
- Place the wing within the wind tunnel with proper mounting and allow the free stream to pass for certain amount of time.
- The pigments in the mixture will trace the flow pattern over the surface.
- Capture the pattern and process in photo editing software.
- Details were discussed in section 3.7.1 page 30.

Balance Measurement

- A three-component balance was used.
- Balance was fixed with the model with the help of screws.
- Balance was electronically connected to the data acquisition device to record data.
- Wing-balance assembly was fitted with the model traversing apparatus and placed inside the wind tunnel.
- Free stream flow was allowed to pass different orientations of the wing, as required, and corresponding data were saved.
- Further calculations were made to find Lift, Drag, Moment and other allied parameters.
- Details were discussed in Section 3.4 page 24 and Section 3.7.3 page 32.

velocity profile

- According to the planform area of the leeward surface of the wing, number of locations were determined.
- A total of 28 locations were marked for observing velocity distribution over the wing surface.
- Calibrated multi-hole probe (a three-hole probe in this case) was employed to acquire the values readings of the three holes.
- The probe was connected to a traversing mechanism that travels normal to the wing surface. A pressure transmitter was employed to record data.
- Readings was taken upto a distance of 20mm above the surface of the wing with regular stops at all 28 locations.
- Mean velocity, chordwise velocity and spanwise velocity was calculated with the help of calibration equations.
- Details were discussed in Section 3.7.4 page 33.

surface pressure distribution

- According to the planform area of the leeward surface of the wing, number of pressure points were determined.

- The pressure points were taken chordwise and five spanwise locations were selected.
- A total of 28 small holes (1.3mm dia.) were drilled at desired points to accommodate PVC tubes which will capture the surface pressure on the wing.
- Other end of the PVC tube was connected to the pressure transmitter to measure the pressure during experiment. It should be kept in mind that all other loose ends of the PVC tube, except the one in use, is temporarily sealed.
- Data was recorded at different orientations in the datasheet prepared for the same.
- Details were discussed in Section 3.7.2 page 31.